Advanced Virtual Synchronous Generator Implementation on a Modular Multilevel Converter

By

Chen Jiang

A Thesis submitted to the Faculty of Graduate Studies of

The University of Manitoba

in partial fulfillment of the requirements for the degree of

Doctor of Philosophy

Department of Electrical and Computer Engineering

The University of Manitoba

Winnipeg, Manitoba, Canada

Abstract

Voltage Source Converters (VSC) are finding increasing usage due to the growing demand for renewable energy resources (RES) and distributed energy resources (DES). However, DES and RES connected using traditional VSCs experience adverse behavior in weak ac networks where the phase angle at the point of common coupling (PCC) can change rapidly. One solution to this problem is to make the converter mimic the characteristics of a synchronous machine which makes the connection to a weak grid with other generation sources much easier. The resulting VSC is referred to as a "Virtual Synchronous Generator" (VSG) and behaves in a similar manner to traditional synchronous generators with which there is a century of experience. Hence, synchronizing the VSG with a grid consisting of other synchronous generators and even multiple VSGs is straightforward. However, unlike real synchronous generators which are robust and can handle large short circuit currents, the power electronic switches of a VSG require protection due to their reduced overcurrent capability.

The conventional VSG faces several challenges, for example, it is difficult to include inherent current limits, and even with an added embedded current limiter, often the converter can become unstable when connected to the grid, particularly when it has a high short circuit ratio. To overcome the drawbacks, this thesis proposes a novel current source interfaced VSG, which emulates the mechanical and electrical dynamics of an actual SG and can be operated as a current source interface at the same time.

Before designing the current source interfaced VSG, a control method to make the converter act as a high-bandwidth and high-precision current source is required and is proposed in this thesis. The novel hysteresis current controller using acceleration slope designed for the modular multilevel converter (MMC) makes use of the multiple voltage steps available with the MMC and accelerates or decelerates the rate of change of current depending on whether it deviates significantly from the target current. Both the Electromagnetic Transients (EMT) simulation and hardware-in-loop (HIL) experiment validate the successful operation of the proposed current controller. Also, the power loss analysis shows that the MMC with the proposed current controller i) has significantly less

power loss than a two-level VSC with hysteresis control and ii) is essentially the same as that of an MMC controlled as a voltage source, which is the commonly used configuration for MMCs in HVdc transmission applications.

Using the proposed hysteresis current controller, a current source interfaced VSG named SM emulation VSG is introduced then. In this case, the inherent current limiting function can be implemented easily and straightforwardly by simply limiting the magnitude of the current reference. Additionally, this proposed approach allows one to represent the VSG with the differential equations of an actual SG with as much detail as desired, such as the number of d- and q-axis windings, etc. Both small signal analysis and EMT simulation results show that the VSG remains stable not only in weak systems but also in ultra-stiff systems, which was identified as a challenge for earlier conventional VSG implementations. In order to demonstrate the viability of the proposed approach, it is also compared with other existing or emerging VSG approaches such as Swing Equation (SE) based VSG. Additionally, the small signal analysis is also conducted to investigate the effect of inclusion/exclusion of the damper windings.

Moreover, since the parameters of the proposed VSG are not restricted to the range of a physical machine, one is free to arbitrarily assign any parameter value that one may wish. A genetic algorithm (GA) is used to optimize the parameters to obtain better performance.

Index Terms: Electromagnetic Transients Simulation; Virtual Synchronous Generator; Grid-forming Converter; Modular Multilevel Converter; Hysteresis Current Control; Small Signal Analysis.

Acknowledgments

I feel blessed to have Prof. Aniruddha Gole as my academic supervisor and my life mentor during my Ph.D. journey. During this 6-years, he has taught me a lot and has guided me to a professional research attitude and direction. Most importantly, he kept me fed. Thanks boss. Jokes aside in the past few years, I had to go through some tough times due to the Covid pandemic. Without Prof. Gole's endless patience and inspiring encouragement, I would have never been able to carry out this work. I am proud to be his student, and I want him to be proud of me as well.

I also want to thank Dr. Yi Zhang. I am honored to cooperate with him in research works. He has provided valuable advice during the study and has spent countless hours to help me with the research.

In addition, I would like to thank Prof. Vajira Pathirana, Prof. Qiuyan Yuan and Prof. Gregory Kish to become my committee members. Thank you for taking your time reviewing my work and providing thoughtful feedback.

I would like to acknowledge all the members and groupmates in the power systems simulation lab. You know who you are. (Hahahaha~~). We had fun together, worked together and brainstormed new ideas together. Meanwhile, I would also like to thank all supporting staffs, especially Erwin Dirks, Amy Dario, Traci Gledhill, Shrimal Koruwage, Eddy Cheung and Samuel Kidd. They are always helpful and supportive during my study.

Nobody has been more important to me in the pursuit of this project than the members of my family. I would like to thank my younger brother Jiaxu Jiang, my parents and my parents-in-law, whose love and guidance are with me in whatever I pursue. Most importantly, I wish to thank my loving and supportive husband, Dr. Dong Li, who provided me with unending inspirations, and kept me away from housework.

In last part of this non-academic section, I would like to share some fun knowledge with the readers. Please allow me to introduce the world's smallest bird – Hummingbird, which is the favorite bird of Prof. Gole and me.

1. Bee hummingbirds are the smallest birds in the world; so small in fact, that they are often mistaken for insects.
2. Their eggs are same size of coffee beans.
3. In flight, the Bee Hummingbird’s tiny wings beat 80 times per second and can fly upside down and backwards.
4. One of the fastest in the animal kingdom, bee hummingbirds heart rates can reach 1260 beats per minute.

It is hard to image that how much power is stored in this little beautiful creature. So, just like A. A. Milne said, you are stronger than you think.

Chen JIANG

List of Tables

List of Figures

List of Abbreviations

Ac	Alternating current
APF	Active Power Filter
CCSC	Circulating Current Suppression Control
Dc	Direct Current
DES	Distributed Energy Source
DOL	Direct-on-Line
EMT	Electromagnetic Transient
FACTS	Flexible Ac Transmission System
GFL	Grid Following
GFM	Grid Forming
GTO	Gate Turn-off Thyristors
GTIO	Giga-Transceiver Input/Output
GA	Genetic Algorithm
HVdc	High Voltage Direct Current
HIL	Hardware-In-Loop
IGBT	Insulated Gate Bipolar Transistors
LCC	Line Commutated Converter
MMC	Modular Multilevel Converter
M/S	Master-Slave
MIMO	Multi-Input Multi-Output
NLC	Nearest Level Control
NLVCS	Non-Liner Vector Current Source
PWM	Pulse Width Modulation
PLL	Phase-Locked Loop
PMA	Power Management Allocator
PI	Proportional-Integral
POC	Point Of Connection
PCC	Point of Common Coupling

RTDS	Real-Time Digital Simulator
RMS	Root Mean Square
RoCoF	Rate of Change of Frequency
SG	Synchronous Generator
SMs	Sub-modules
SE	Swing Equation
SM	Synchronous Machine
SCR	Short Circuit Ratio
SS	Small Signal
VSC	Voltage Source Converter
VSG	Virtual Synchronous Generator

Contents

1 Introduction

This chapter introduces the background of voltage source converters (VSCs) used for High Voltage Direct Current (HVdc) power transmission and discusses why virtual synchronous generators (VSGs) are a useful VSC topology option. It starts with a discussion of HVdc technology and particularly the VSC, which is seeing increasing use in modern HVdc systems. Then the most widely used control strategies, i.e., decoupled current control [1] and droop control [2]-[3] are presented. Finally, this chapter demonstrates limitations with the traditional methods and discusses how the newly emerging VSG control approach shows promise in overcoming these limitations.

1.1 High Voltage Direct Voltage Transmission Background

1.1.1 Ac Versus Dc Transmission

High voltage ac transmission is the most widely used power transmission technology in the world. It has the advantage of easily changing voltage levels through transformers and simple generator structures. However, when used in transmission, it has higher losses due to poor power factor, skin effect, etc. Also, when used for underwater or underground cable transmission, the high charging current required for ac transmission can be problematic. On the other hand, dc transmission has unique advantages in certain applications, i.e., long-distance transmission systems and dc cables [4]-[7].

In highly populated urban areas, underground cables are more suitable for power system planning. It is well known that the underground ac cables have higher capacitance than the overhead transmission lines due to its physical structure. Therefore, the capacitive current in cables causes long-distance transmission to be near impossible without compensation. As shown in Figure 1-1, due to the voltage drop and terminal limit, the acceptable longest length of the transmission line is around $480\ km$ [6]. Although some reactive power compensation equipment can be installed to reduce the total reactance, the cost of the equipment can be very high and may not be practical. However, the dc transmission system does not have the disadvantages mentioned above. As a capacitor is an open circuit to dc, the cable capacitance does not affect the steady-state HVdc operation. Also, due to the dc electric and magnetic fields being constant, there is no ionic motion in the cables and no induced current in the sheath. The capacitive current losses for a long distance can be eliminated due to the constant dc voltage. Therefore, long-distance transmission can be achieved by using a dc transmission line. Additionally, the dc lines do not require reactive compensation thus the cost decreases.

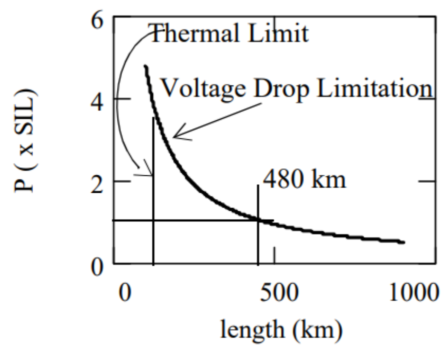

Figure 1-1 Active Power Versus Transmission Line Length [6]

Another advantage of a dc transmission line is the ability to connect two asynchronized ac systems. In ac networks, power can only be transferred between two ac systems with the same nominal frequency and synchronized operation, but dc systems can be used to connect such asynchronous systems. Therefore, some back-to-back HVdc links are built for connecting different frequency systems, such as Itaipu (Brazil) where $50\,Hz$ and $60\,Hz$ systems are connected [8].

Moreover, dc transmission can improve power system stability. Their controllers can change the power rapidly which permits the HVdc links to damp oscillations in the ac interconnecting networks. For example, an auxiliary damping controller can be installed in the HVdc system to dampen low-frequency oscillation in the ac system [9].

1.1.2 Line Commutated Converter (LCC)

In the past, the common dc transmission technology has been the line commutated converter (LCC). The LCC consists of either mercury valves or thyristor valves. The simplest structure of LCC is the 6-pulse Graetz bridge as shown in Figure 1-2. The conversion process ac to/from dc is achieved by sequencing the turn-on of the thyristor switches, T1, T2…T6 in sequence, which results in a current transfer from one ac phase to the other.

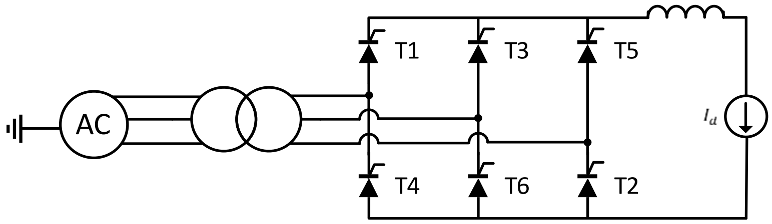

Figure 1-2 Typical Three-phase Six-pulse Graetz Bridge

The LCC can be operated in two different modes, which are rectifier mode and inverter mode. This is achieved by different firing angles on the valves. When the firing angle is less than $90°$, the converter is under rectifier mode. In this mode, the dc current flows from the positive terminal of dc circuits to transfer the power from ac system to the dc link. When the firing angle is higher than $90°$, the converter is operated as an inverter. Under this mode, the dc voltage changes polarity and transfers dc power to ac system. The HVdc transmission system consists of two Graetz bridges, which are interconnected on the dc sides. One is operated as a rectifier and the other is under inverter mode.

The application of LCC-HVdc technology is highly accepted in the modern power system. However, some weaknesses of LCC-HVdc need to be noticed. The first drawback of LCC is reactive power consumption. Both operation modes consume reactive power and are approximately $50-60\ \%$ of the active power [7]. The six-pulse LCC also generates harmonics of frequencies $6n \pm 1$ on the ac side and $6n$ on the dc side, which requires additional filters. Using the widely used 12-pulse connection where two 6-pulse bridges are connected in series on the dc side and shunt on the ac side, the harmonics can be significantly reduced, but considerable filtering is still required. Some compensation equipment such as capacitor banks, synchronous compensators, and higher-rating ac filters are needed to provide reactive power support. The compensation equipment not only increases the costs but also requires more space in the converter station.

Another drawback of LCC-HVdc is the "commutation failure" on the inverter side, which can be defined as the unsuccessful transfer of current from the conducting valve to the next one in the conducting sequence. This is often caused by disturbances in the ac system. When the commutation failure happens, there is a short circuit on the dc side and the power transmission is stopped due to this short circuit. If there are many repeated commutation failures, the HVdc links may trip. Another limitation of the LCC is that the thyristor valves can only be triggered to turn on. Their turnoff is completely at the mercy of the ac voltage, and they turn off when the applied voltage reduces the valve current to zero. This imposes a significant constraint on the range of operation. This limitation can be overcome by using gate-turnoff-able switches such as insulated gate bipolar transistors (IGBTs) as is the case in the voltage source converter (VSC) discussed below.

1.1.3 Voltage Source Converter (VSC)

The voltage source converter (VSC) consists of switches capable of being turned on as well as off with external commands, such as gate turn-off thyristors (GTOs) or insulated gate bipolar transistors (IGBTs). Therefore, the VSC can generate its voltage waveforms independent of the ac system. The widely used VSC structures are two-level VSC, three-level VSC, and modular multilevel converter (MMC) [1][10][11].

1.1.3.1 Two-level Voltage Source Converter (VSC)

The two-level VSC is the most frequently used VSC for all applications with low dc-side voltages [12]. The schematic diagram of a three-phase two-level VSC is shown in Figure 1-3.

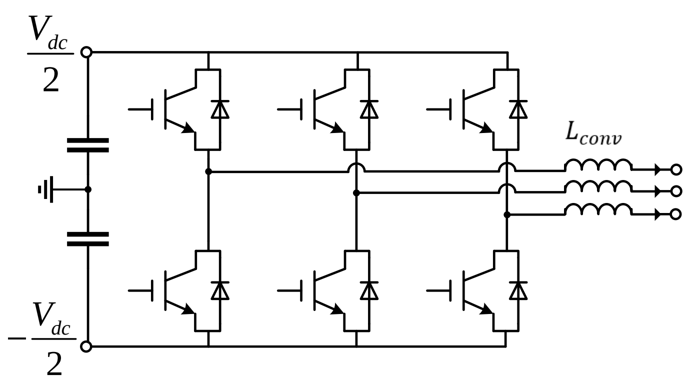

Figure 1-3 Typical Structure of a Two-level VSC

The dc capacitors provide short-term energy storage to maintain the dc voltage approximately constant. Each leg of VSC consists of two unidirectional controllable switches and an anti-parallel diode so that the valve can conduct current in both directions and block voltage in one direction by switch signals. Generally, an inductance L_{conv} is in series with the ac terminal to improve the current waveforms. This could be a separate inductor or be included in the leakage inductance of a downstream transformer.

The basic operation of one phase leg is in Figure 1-4 [10]. With the neutral point selected as the middle node between the dc capacitors as shown, the output voltage only has two values $(+\frac{V_d}{2}, -\frac{V_d}{2})$, hence the moniker "two-level". Notably, the switching signal (firing pulses) of the upper IGBT is always the complement of the lower IGBT to avoid short circuiting the dc bus.

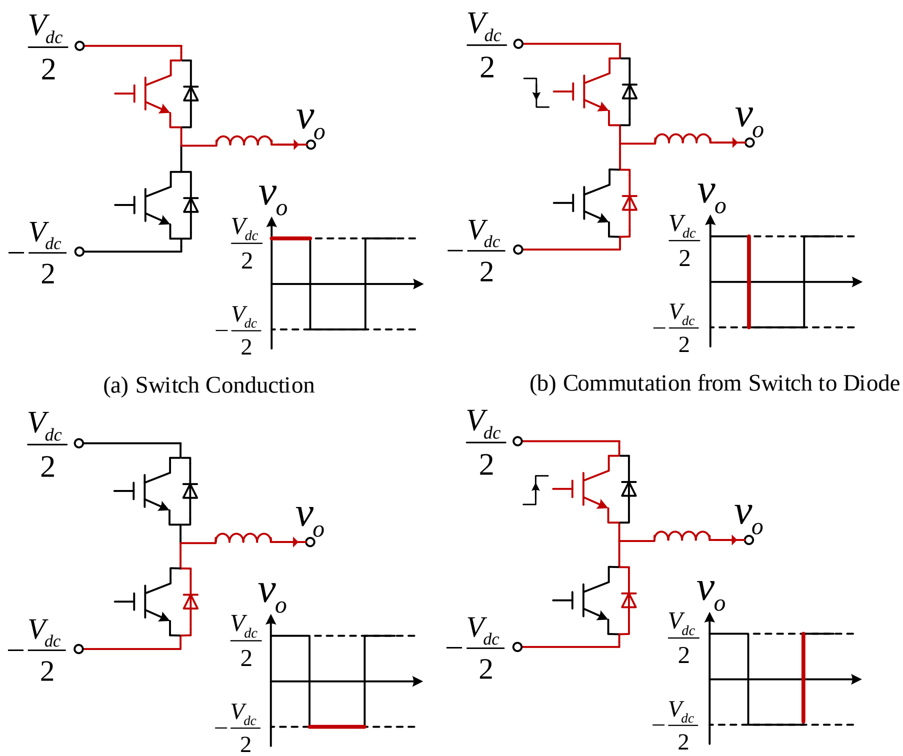

(a) Switch Conduction

(b) Commutation from Switch to Diode

(c) Diode Conduction

(d) Commutation from Diode to Switch

Figure 1-4 Operation of a Two-level Converter Phase Leg

When the upper switch is on as shown in Figure 1-4 (a), the ac terminal voltage is equal to $+\frac{V_d}{2}$. In Figure 1-4 (b), the upper switch is off and the available path for current is the lower diode. After the current is fully commutated to the lower diode, the ac terminal is equal to $-\frac{V_d}{2}$ as shown in Figure 1-4 (c). Normally the lower switch is also turned on after a certain delay time (naming blanking time) as a reversal of the current direction is possible in Figure 1-4 (c). The ac terminal voltage can be returned to a positive value by turning off the lower switch and then turning on the upper switch after a blanking time. This process is in Figure 1-4 (d). After the current path is replaced by the upper switch same as in Figure 1-4 (a), the ac terminal voltage becomes positive again. This sequence can be repeated. If the current is in the opposite direction of Figure 1-4 and the commutation sequence is similar, the difference is the current will be commutating between the upper diode and the lower switch.

Through the switching sequence above, the ac voltage can be switched between $+\frac{V_d}{2}$ and $-\frac{V_d}{2}$ at any desired time, therefore, the converter is controlled as a voltage source. The desired ac voltage can be achieved through the pulse-width modulation (PWM) method.

Although the two-level VSC is economical and a simple solution for low-voltage operation, some shortcomings should be noticed. Firstly, the ac side voltage has a large harmonic component around the switching frequency. As the switching frequency is large (typically in the $1-2\ kHz$ range in HVdc applications), these harmonics do not penetrate as much as the lower frequency harmonics inherent in the LCC. Nevertheless, they do require the installation of an ac filter. Also, as the ac terminal voltage is only changed between $\pm\frac{V_d}{2}$, the high voltage slope causes significant stress on the insulation of connected ac-side equipment. Each switching event also results in a considerable energy loss as any parasitic capacitance on the ac busbar has to traverse a voltage change of $|V_d|$. In order to have better performance, the multilevel converter topology discussed next is now becoming dominant in new VSC-HVdc installations.

1.1.3.2 Modular Multilevel Converter (MMC)

Modular multilevel converters (MMCs) today become the most popular VSC topology which is now widely used in applications such as HVdc transmission [13], variable-speed drives [14], renewable energy generators [15], flexible ac transmission systems (FACTS) [16] and so on.

The schematic diagram of a one-phase MMC is shown in Figure 1-5 (a). The arm consists of several identical modules which can be either the half-bridge or full-bridge type.

With appropriate switching signals, any desired ac terminal voltage can be obtained. The MMC has lower losses and can generate nearly harmonic-free ac voltage waveform compared to the two-level VSC. The dc capacitors are distributed within each module, while the MMC is built up by cascade-connected modules. Therefore, the ac terminal voltage can have several voltage levels depending on the number of modules.

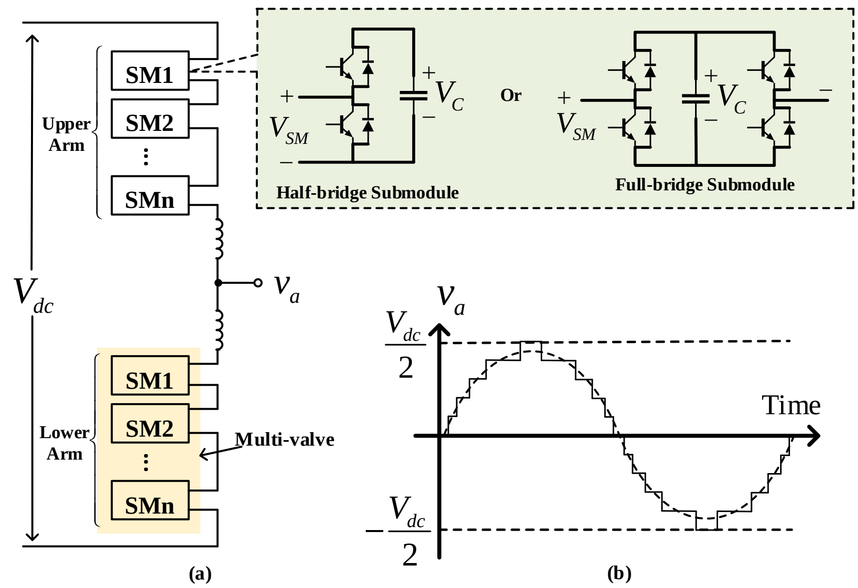

Figure 1-5 (a) Half-bridge or Full-bridge Schematic Diagram of a One-phase MMC. (b)Schematic Diagram of MMC Output Voltage Waveforms.

The modular structure of the MMC is suitable for high-voltage applications because the design can be changed by including either more or fewer submodules to accommodate the rated voltage of choice, without requiring the redesign of the submodule. During operation, the ac voltage waveform is generated by adding or bypassing specific modules in the arm as shown in Figure 1-5 (b). With a large number of levels, the stepped output waveform can be made to closely follow a sinewave, thereby eliminating any filter requirement.

With a properly designed MMC, each module is switched on or off infrequently in one cycle, and the change in voltage at its terminals is simply the module voltage and not the entire dc voltage (as was the case for the 2-level topology). This significantly decreases the switching losses of the converter. An additional advantage of MMC is that the control system has extra freedom to deal with dc side faults. The dc capacitors are not completely discharged during the fault so that the fault recovery can be faster [11].

On the other hand, compared to the two-level VSC, the MMC has a more complex structure. and the design of the control system is more complicated. Some additional control features are needed to balance the voltages on each of the sub-module capacitances (via the capacitance voltage balancing controller) and to suppress circulating current (via the circulating current suppression controller, also known as CCSC).

1.2 Park's Transformation

Neglecting the zero sequence, the three-phase ac variables can be transformed to a two-axis rotating frame (the dq reference frame). Most VSC controllers work in the dq reference frame, as it becomes easier to directly control the real or reactive powers independently. This is discussed below.

The Park transformation matrix is used to transform the variable parameters from the phase abc reference frame to a rotated dq reference frame [17]. If the ac variables in the phase abc reference frame are balanced, the variables become dc constant after transforming into the dq reference frame. In the study of synchronous generators, this transformation can also be regarded as referring the stator quantities onto the rotor side.

The transformation matrix and its inverse matrix are in (1-1) and (1-2) below, where θ is defined as the angle by which the d-axis leads the centerline of phase a winding in the direction of rotation. When the transform is applied to electrical machines, θ represents the mechanical angle of the rotor. This angle is carefully chosen to effectively convert stator variables to the rotor side, creating a more simplified and intuitive physical representation of the machine's model.

$$T(\theta) = \frac{2}{3}\begin{pmatrix} \cos(\theta) & \cos(\theta - \frac{2\pi}{3}) & \cos(\theta + \frac{2\pi}{3}) \\ \sin(\theta) & \sin(\theta - \frac{2\pi}{3}) & \sin(\theta + \frac{2\pi}{3}) \\ \frac{1}{2} & \frac{1}{2} & \frac{1}{2} \end{pmatrix} \tag{1-1}$$

$$T^{-1}(\theta) = \begin{pmatrix} \cos(\theta) & \sin(\theta) & \frac{1}{2} \\ \cos(\theta - \frac{2\pi}{3}) & \sin(\theta - \frac{2\pi}{3}) & \frac{1}{2} \\ \cos(\theta + \frac{2\pi}{3}) & \sin(\theta + \frac{2\pi}{3}) & \frac{1}{2} \end{pmatrix} \tag{1-2}$$

According to (1-3), the voltage and current transformation can be expressed as follow,

$$\begin{pmatrix} v_d \\ v_q \\ v_0 \end{pmatrix} = T(\theta) \times \begin{pmatrix} v_a \\ v_b \\ v_c \end{pmatrix}, \begin{pmatrix} i_d \\ i_q \\ i_0 \end{pmatrix} = T(\theta) \times \begin{pmatrix} i_a \\ i_b \\ i_c \end{pmatrix} \tag{1-3}$$

1.3 VSC Converter-level Control

This section describes how the higher-level controls are designed for any VSC (MMC or 2-level VSC). Typically, the VSC control mode can be either the grid following (GFL) or grid forming (GFM) type.

1.3.1 Grid Following Strategy

The grid-following control method is the commonly used technique for converter control. This approach enables converters to synchronize their generated voltage waveform with the grid voltage waveform by using a phase-locked loop (PLL). The PLL tracks the phase (and frequency) of the grid voltage and generates the timing reference for firing the converter's valves. However, it may pose challenges in scenarios where the grid has a high impedance (i.e., it is "weak"), so that a change in the power order causes a sudden shift in the phase of grid ac voltage, which may result in poor tracking. Also, slight variations or disturbances in the weak grid can lead to fluctuations in converter operation, potentially affecting system performance and introducing instability.

The typical strategy in grid-following control (GFL) is the 'dq decoupled control,' which has been used over many years. An overview of this method is provided below.

Figure 1-6 shows a VSC converter connected to an infinite bus through a transformer. With all voltages referred to one side, the transformer equivalent circuit is a series $L - R$ circuit as shown. Voltage triplets (v_a, v_b, v_c) and (e_a, e_b, e_c) represent phase voltages at grid side and converter side respectively and currents (i_a, i_b, i_c) represent line currents.

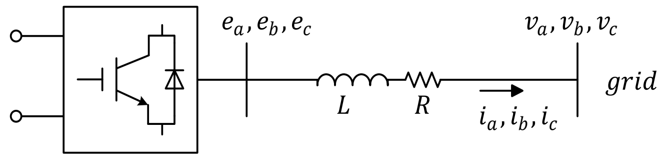

Figure 1-6 One VSC Connected to an Infinite Bus

With the dq decoupled control strategy, the output currents of the VSC are generated according to the dq-axes current order. The outer loop calculates the dq-axes current reference based on the power order and this current reference is inputted into the inner loop. The outputs of the inner loop are the d- and q-axis components of the desired voltage from the VSC. Converting from rectangular to polar coordinates, the magnitude (in pu, this is the modulation index) and phase of the VSC's output voltage are realized. This voltage can be generated either by using the pulse width modulation (PWM) technique for a 2-level converter or by using a more sophisticated method for a multi-level modular converter (MMC) [10]. Therefore, output active and reactive power from VSC to the grid are controllable separately. Since the current of the VSC is the direct control variable of the controller, it is easy to limit the current during operation in case of the VSC or other devices have damage risks because of over-current phenomena.

The control block diagram of the dq-decoupled controller is shown in Figure 1-7 below [1]. P_{ref} and Q_{ref} are the active and reactive power references, P and Q are the measured powers flow out from the converter. i_d, i_q and u_d, u_q are the measured system current and terminal voltages in dq reference frame. i_d^*, i_q^* and e_d^*, e_q^* are the current and voltage references in dq reference frame.

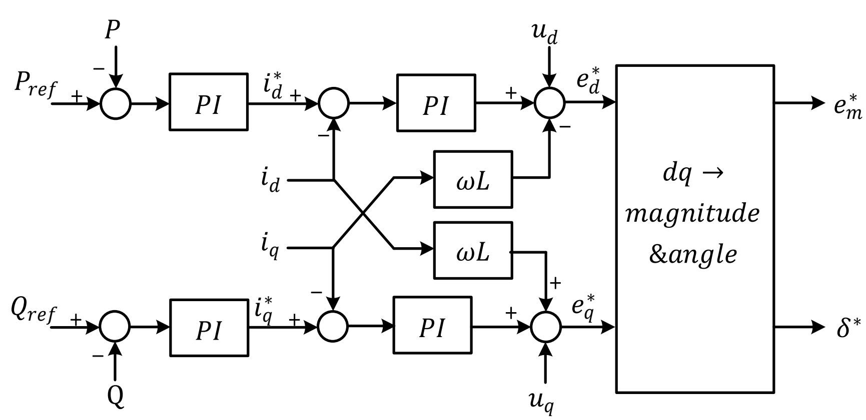

Figure 1-7 Control Block Diagram of Dq Decoupled Control

The '*dq-frame* → *magnitude and angle*' block converts the dq quantities back to the magnitude and phase of the ac voltage using (1-4) and (1-5) below. Here e_m^* and δ^* are the magnitude and phase angle of the reference voltage. These are then converted straightforwardly to reference voltage waveforms for each of the three phases, which transferred to the firing block for generating the on/off signals for the IGBT switches.

$$e_m^* = \sqrt{{e_d^*}^2 + {e_q^*}^2} \tag{1-4}$$

$$\delta^* = \arctan\left(\frac{e_q^*}{e_d^*}\right) \tag{1-5}$$

The downside of the dq-frame decoupled control is that it needs a phase-locked loop (PLL) to lock on to the phase of the grid voltage, and then the controller will follow this value to control the frequency of the VSC side. This will cause some problems when the VSC is in the islanding mode of operation, such as terminal voltage dropping, frequency unstable, and so on. To overcome this problem, some additional control loops become necessary, which further increases the complexity of the controller.

It should be noted that the proportional integral (PI) controllers result in a delayed response and any current order change cannot be instantaneously followed. This is different from the proposed hysteresis current controller used later in this thesis (Chapter 4).

Other methods are also possible and sometimes used in power transmission applications. For example, Alpha-Beta control, or $\alpha\beta$ control [18] which transforms three-phase AC signals into a two-dimensional $\alpha\beta$ reference frame. This transformation simplifies the control of VSCs by decoupling the active power control (in α-axis) from the reactive power control (in β-axis). Such decoupling enables precise and independent control of real and reactive power output, which is essential for grid stability and power quality enhancement. However, this method requires proportional resonant (PR) controllers specific to the rated frequency rather than PI controllers, which can increase computational demand (when digitally implemented) and behave sub-optimally if the ac frequency changes.

1.3.2 Grid Forming Strategy

The grid-forming (GFM) control method [19] is a recent advancement in converter control. Unlike the traditional GFL control strategy, where converters synchronize with the grid's voltage and frequency, the GFM itself generates its output voltage and frequency and can be used for connecting to purely passive loads or very weak systems. The magnitude and phase of the generated voltage is continuously adjusted to deliver the desired real and reactive powers. This innovative approach allows converters to establish a new grid reference and actively shape the network's voltage and frequency, making them capable of initiating and sustaining a stable grid in scenarios where the main grid might be unavailable or unstable. GFM holds promise for enhancing grid resilience, enabling microgrid operation, and ensuring reliable power supply from renewable sources.

1.3.2.1 Droop-based Control Strategy for GFM

Droop-based control is one of the basic GFM strategies to control the terminal voltage and the frequency of the VSC side (e_a, e_b, e_c in Figure 1-6) instead of the current flow of the system (i_a, i_b, i_c in Figure 1-6) [2][3]. This control strategy needs voltage and current feedback from the ac network.

The power flow equations are defined below. In (1-6) and (1-7), E is the voltage magnitude of the sending point and V is the voltage magnitude of the receiving point, δ is the angle difference of these two voltages, X is the line reactance between these two points. P and Q are the active power and reactive power flow from the sending point to the receiving point.

$$P = \frac{VE}{X} sin\delta \tag{1-6}$$

$$Q = \frac{V^2}{X} - \frac{VE}{X} cos\delta \tag{1-7}$$

When the resistance of the transmission line is ignored, active power 'P' changes with power angle $\delta = \int(\omega - \omega_0)\, dt$, where the ω_0 is the nominal frequency. On the other hand, reactive power 'Q' is more sensitive to the voltage magnitude. Therefore, active power 'P' is a function of system frequency (ω), and reactive power 'Q' is a function of voltage magnitude. Assuming that the relationship is linear, then the following characteristic equations can be established. Equations (1-8) and (1-9) defined as the $P-\omega^*$droop characteristic and $Q-E^*$droop characteristics respectively. E^* and ω^* are the reference frequency and voltage, ω_0, E_0, P_0 and Q_0 are the steady state values of the frequency, terminal voltage, active power, and reactive power. Variables m and n are the droop constants.

$$\omega^* = \omega_0 - m(P_0 - P) = g(P) \tag{1-8}$$

$$E^* = E_0 - n(Q_0 - Q) = f(Q) \tag{1-9}$$

The control block is in Figure 1-8 below. The V_{ref} is equal to E^*, and δ_{ref} can be calculated by integrating the reference frequency ω^*.

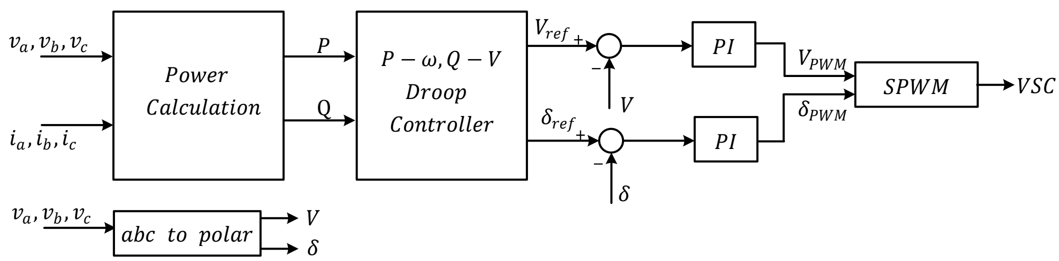

Figure 1-8 Droop Control Structure

Additionally, this control strategy is suitable for both operation modes (grid-connecting mode and islanding mode), the droop controller can also achieve load sharing without a communication link between different inverters in proportion to their power rating by choosing droop parameters appropriately.

However, since the controller is in voltage-source control mode, there is no inherent current limiting. Also, there are steady-state errors in frequency and voltage.

1.3.2.2 Virtual Synchronous Generator (VSG) Control

As the number of inverter-based distributed energy source (DES) connections into the modern grid replaces existing synchronous generators, the inertia of the power system decreases. This can cause frequency oscillation problems and creates new unstable conditions [17]. Both VSC control strategies (decoupled current control and droop control) mentioned above will encounter problems when the connected system is 'weak' because these control strategies do not provide inertia to the system.

To support low inertia systems, a new control method is required. The features required in this new control approach include:

1) The inertia should be provided to the power system to improve the frequency oscillation problem.
2) The VSC should be operated not only in grid-connecting mode but also in islanding mode without any control structure changing.
3) The damping function should exist to decrease the transient process faster.
4) The control strategy should have a current limit ability to protect the VSC from over-currents.
5) The load can be shared between several VSCs automatically according to the predetermined droop parameters without communication links.
6) The voltage and frequency steady state error should be eliminated.

Some existing control strategies only partially address the above requirements. For example, an extra lag control block or lead control block can be added to the droop controller (shown in section 1.3.2.1) to provide inertia and damping respectively. However, the over currents cannot be effectively limited [20]. One can also provide inertia via the addition of a low pass filter block to the control system, but the steady-state error still exists in the power and voltage [21]. Among the different control strategies for VSC, a control strategy named virtual synchronous generator (VSG) can achieve all the requirements above [22]-[24].

The VSG is classified as a GFM control strategy, in which the converter is controlled to mimic the behaviour of a synchronous generator (SG). It is known that the synchronous generator (SG) has high inertia because of the rotor mass which improves the frequency oscillation damping [17]. Besides, the synchronous generator does not need communication when several machines are connected to a power network. The machines can achieve load sharing automatically. Also, the synchronous generator can be controlled to provide damping to the power system when a transient process happens.

Since the synchronous machine has these advantages, it is a good idea to let the VSC mimic the behavior of the SG with the design of a suitable control structure. Note that actual synchronous generators have a real inertia in the due to the kinetic energy storage in the rotating mass of its rotor. In a virtual synchronous machine such a store of energy has to be provided, such as through a battery energy storage or a remote connection to a rectifier in a point-to-point transmission system.

In most cases, a simplified model of the SG is used, such as the swing equation-based VSG discussed in Chapter 2 later, where the electro-mechanical swing equation and a simplified representation of damping are included. Additional blocks, such as extra damping loop [25] can be added to such a model to improve dynamic performance. Similarly, a virtual impedance controller can be combined with the VSG representation to emulate the slow time-varying (quasi-stationary) impedance characteristics of a real SG [26][27]. This type of controllers typically provide d- and q-axis current orders which can be passed to a decoupled dq controller to generate the modulation index for the converter's firing pulse generation block. However, [28] shows that such VSG controller may cause the converter to become unstable when it connected to a strong system.

This thesis will develop and investigate a novel current source interface VSG (detailed synchronous machine emulation VSG in Chapter 5), which emulates the mechanical and electrical dynamics of an actual SG. This strategy will optimize the behaviors of converter and achieve all the requirements mentioned above.

It should be noted that the VSG control methods described in this thesis can be implemented with two-level VSC or MMC technology. For high power and voltage levels, the MMC is the converter of choice due to its lower losses and modular construction. However, for voltages be lower power lower voltage applications, e.g., below $350\ kV$, $600\ MW$), such as in the Caprivi HVDC Interconnector in Namibia [29], the 2-level VSC topology is still commonly used due to its simplicity of control.

1.4 Additional Standard MMC Controllers

In this section, some additional standard MMC controllers will be introduced, which are circulating current suppression control (CCSC), nearest level control (NLC), and capacitor voltage balancing control. These controllers are commonly used and are always equipped with the MMC.

1.4.1 Circulating Current Suppression Controller

In an MMC, there can be even harmonics currents that circulate between the legs and do not enter the network [10] and the main components of the circulating currents are second-order harmonics. The circulating currents $i_s^{abc} = [i_s^a, i_s^b, i_s^c]$ can be obtained from the sum of arm currents in each phase. From Figure 1-5, each arm of the MMC has the arm inductance L_{arm}, and the purpose of the arm inductance is merely to limit high-frequency components in this circulating current and to enable a smooth circulating current control.

In order to cancel the circulating harmonics, the circulating current suppression controller (CCSC) is required. The widely used CCSC method is the decoupled CCSC as shown in Figure 1-9.

The circulating-current control is intimately linked to the voltage control. From the controller structure, the circulating currents i_s^{abc} is first transferred to the dq reference frame by the Parker transformation to get the d- and q-axis second-order harmonics components. And a decoupled controller is designed to control i_s^d and i_s^q separately to zero by generating the order of the compensating voltage v_{cc}^{dq} using the proportional-integral (PI) controller. Then v_{cc}^{dq} is converted back to abc coordinate. v_{cc}^{abc} is combined with the voltage references v_{ref}^{abc} from the main controller to provide the final voltage order to MMC.

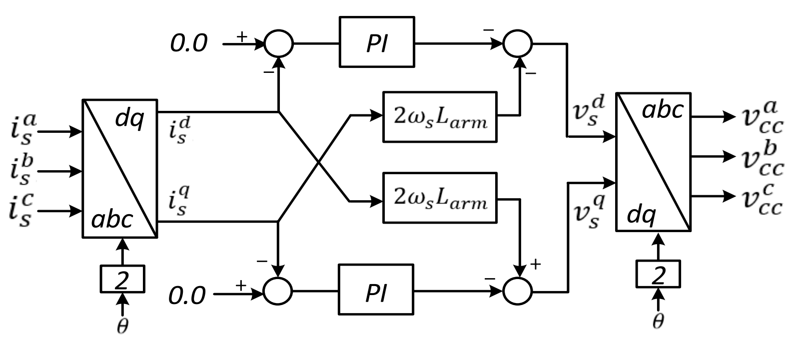

Figure 1-9 Decoupled Circulating Current Suppression Control

1.4.2 Nearest Level Controller

This section focusses on the modulation of the output voltages of the MMC. After generating the final voltage orders, the next step is to decide the number ‘N’ of the active submodules at each time instance to provide the MMC's required voltages. Since the MMCs can only generate discrete voltage levels, the main idea of the modulation is to convert the continuously varying voltage references to discrete numbers.

Many different methods including multilevel carrier-based modulation methods and nearest level controller (NLC) can be used [10]. In the thesis, the NLC algorithm is chosen and is introduced later.

The NLC algorithm is originally created for large multilevel drive applications and one of the advantages of this method is the simple implement. The main idea of the NLC is to sample the voltage references at high frequency f_s and to approximate it with the nearest available level.

The easiest approximation can be formulated mathematically by applying the '*round(x)*' function, which will output the closest integer. Also, there are some modified versions of the approximation algorithm. In this thesis, the updated 'discretization sinusoidal reference' is used. The function of this block is that it generates the proper discrete number of the submodules according to the per-unit voltage reference $v_{ref,pu}$. The algorithm is shown below in (1-10), where N is the number of the submodules in each arm of the MMC, and the *'floor(x)'* function indicates the greatest integer less than or equal to x.

$$N_{out} = floor\left[0.5 + \left(v_{ref,pu} + 1.0\right) \times 0.5 \times N\right] \tag{1-10}$$

The sampling frequency f_s should be high enough to avoid voltage steps change in one instant exceeding one capacitor voltage level. The minimum required sampling frequency can be calculated from (1-11), where f_1 is the system fundamental frequency, and N is the number of the submodules in each arm.

$$f_{s,min} = \pi N f_1 \tag{1-11}$$

1.4.3 Capacitor Voltage Balancing Controller

After deciding on the correct number N_{out} of the active submodules (SMs), the next step of the MMC is to choose which N_{out} out of N SMs are inserted. This is done by capacitor voltage balancing controller.

The capacitor voltage of each SM (V_c) are changed during the MMC operation depending on the status of the SM and the arm's current direction. It is well known that the capacitors of the inserted SMs are charged when the concerned arm current is positive, then its V_c increases. On the other hand, when the arm current is negative, the capacitors of the active SMs are discharged and its V_c decreases. And the capacitor voltages remain unchanged when the SMs are bypassed. For energy balance purposes, it is necessary to choose the proper SMs to insert or bypass when the voltage order is changed.

Different capacitor voltage-balancing methods can be found in [10], such as submodule sorting, predictive sorting, tolerance ban method, and so on. In this thesis, the basic submodule sorting method is used, and the main idea is introduced below.

The submodule sorting method is one of the simplest methods, which is based on identifying the submodules with the highest and lowest instantaneous capacitor voltage [31]. The main idea is to regulate all the capacitor voltages around the average voltage level ($\frac{V_{dc}}{N}$) by charging the lower voltage magnitude capacitors and discharging the higher voltage magnitude capacitors. Where V_{dc} is the dc side voltage and N is the number of SMs in each arm.

Assuming that only one SM is required to insert or bypass when the voltage reference changes, then a total of four situations is possible. The algorithm logic is as follows:

1) An SM should be inserted, and the arm current is positive. In this case, the bypassed SM with the lowest capacitor voltage is chosen since this process will cause the capacitor to be charged, whereby its voltage increases to reach the average value.
2) An SM should be inserted, and the arm current is negative. In this situation, the bypassed SM with the highest capacitor voltage is chosen since this process will cause the capacitor to be discharged, whereby its voltage decreases to reach the average value.
3) An SM should be bypassed, and the arm current is positive. In this case, the active SMs with the highest capacitor voltage is chosen. This is because the process will stop the charging of the capacitor and thus the voltage will not depart from the average value further.

4) An SM should be bypassed, and the arm current is negative. In this case, the active SMs with the lowest capacitor voltage is chosen. This is because the process will stop the discharging of the capacitor and thus the voltage will not depart further from the average value.

When the number of the SMs which are required to insert or bypass is more than one, for example, two SMs should be inserted and the arm current is negative, then the SMs with highest and second highest capacitor voltage are chosen.

1.5 Thesis Structure

Based on the framework of the research, this thesis is organized as:

Chapter 1 gives the background information, literature review, and introduction.

Chapter 2 introduces Swing-Equation (SE) based VSG control with switchable current limiting control. The mathematical explanation of the control design process is included. Additionally, the proposed controller has applied an MMC system for verification in the Electromagnetic Transient (EMT) program.

Chapter 3 shows the comparative study of the widely used Master-Slave controller and SE-based VSG controller for parallel VSC-HVDC links feeding passive loads on offshore platforms under different operation situations.

Chapter 4 introduces a non-linear method to control the MMC like a high-bandwidth and accurate current source. Besides the traditional hysteresis current control for the two-level VSC, a novel hysteresis current control method using acceleration current slope designed for the MMC is also proposed. The power loss analysis is then discussed. Finally, a popular application which is the active power filter (APF) is presented in the offline EMT program and the physical real-time digital simulator (RTDS).

Chapter 5 gives the details of detailed synchronous machine (SM) emulation VSG with current limiting blocks. Unlike the SE-based VSG controller, this VSG method regulates the output currents from the converter, therefore, it is easy to limit the currents. The mathematical explanation of the controller's design process is included. Several simulation results are provided for verification.

Chapter 6 gives the mathematical derivation of the small signal models of the VSG mentioned in chapter 5. Eigenvalue analysis is performed to study the influence of the damper windings and other parameters. Also, the stable operation of the VSG is investigated with different SCR ac systems. Moreover, since there is no physical restriction of the parameters of the VSG, the genetic algorithm (GA) is used to optimize the parameters to obtain a better damping performance.

Chapter 7 concludes the comparison between SE-based VSG and detailed SM emulation VSG from different aspects, which are damping support, similarity to the synchronous generator, and over-current protection.

Chapter 8 concludes the thesis and lists the future works in progress.

2 Swing Equation Based Virtual Synchronous Generator Control

The synchronous generator (SG) is the most widely used power source in modern networks. It can provide voltage output with a stable frequency and magnitude in the presence of arbitrarily varying loads. If there is more than one SG connected to the grid, when the frequency changes due to power demand fluctuation, each SG will respond to this fluctuation according to its own damping factor and inertia constant. Therefore, no communication system is needed between SGs to distribute power and eventually all generators will settle into the new steady state.

If the voltage source converter (VSC) can be controlled to mimic the behavior of an SG, the VSC can maintain the frequency and voltage properly. Moreover, the VSCs in parallel operation can also share power demands automatically and independently without using any other high-level control signal to distribute power for each VSC.

The control system of a VSC (2-level or MMC) can be designed so that the VSC behaves like a 'virtual synchronous generator' (VSG). The controller mimics the dynamics of an SG. The level of adherence to a true SG can be approximate or very accurate, the former being the usual case. One advantage of this type of model is that the phase-locked loop required for a conventional VSC controller to obtain the timing reference can be avoided. One issue is that an actual SG can tolerate very large short-circuit currents. On the other hand, if the VSG had the same currents, it would damage the IGBT valves. Hence, any VSG implementation must also include some form of current limitation, which is not present in a real SG.

2.1 Swing Equation-based VSG

One VSG implementation is the Swing Equation (SE) based VSG. It essentially models the mechanical dynamics of an SG accurately but simplifies the electrical part. It is discussed in this chapter, which also includes a discussion of how the current can be limited so as not to damage the IGBT valves.

The core swing equations (which primarily consider the dynamics of the mechanical movement of the rotor) of an SG model are built inside the VSG controller. The electrical representation is very simple and is essentially a controlled ac voltage source. Additional factors such as the damper windings are ignored in this approach. Therefore, this type of VSG controller is named 'Swing Equation (SE) based VSG'. Such converters (along with their associated control systems) are also called 'Synchronverters' [22].

2.1.1 Implementing the SG Model in the VSC-Inverter Controller

The general structure of a grid-connected VSC inverter (2-level) is shown in Figure 2-1. The VSC inverter is connected to the grid through an LC filter. With the VSG control strategy, the VSC will behave like an SG with the approximate model shown in the figure.

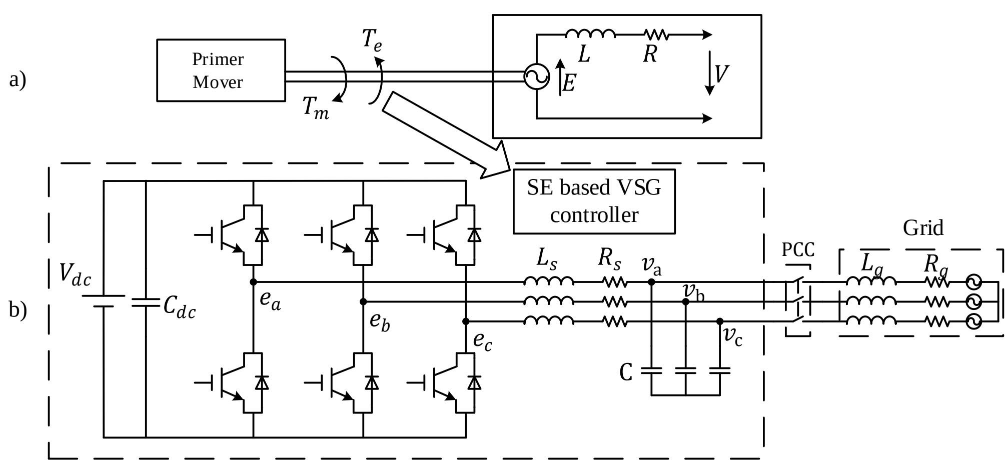

Figure 2-1 (a) The Simplified SG. (b) The SE-based VSG Implementation.

From Figure 2-1, the inductor L_s of the LC filter can be selected as the synchronous inductance (L) of the SG. The resistance (R_s) of the filter can be selected as equal to the synchronous resistance (R) of the SG. The internal back electromotive force voltage (E) is computed by the controller and becomes the reference voltages (e_a^*, e_b^*, e_c^*) for the PWM controller which generates the internal PWM voltages (e_a, e_b, e_c). Note that the low frequency component of the PWM waveform e_a will be equal to e_a^*, etc. The capacitor voltage (v_a, v_b, v_c) is equivalent to terminal voltage (V) of SG. The mechanical power exchanged with the prime mover is replaced with the power exchanged with the dc bus.

2.1.2 Electrical Part of Synchronous Generator in the SE-based Model

Models of the SG with various levels of detail are introduced in the literature [17]. For system analysis and control design, a simplified model of the SG is used to build the VSG. Assume that the rotor of SG is a round rotor without any damper windings, as shown in Figure 2-2. The self-inductance and resistance of the field winding are L_f and R_f, respectively. There is one pair of poles per phase with identical and rotationally symmetric concentrated coils. When implementing the VSG, the magnetic-saturation effects in the iron core and eddy current are not considered and hence not included. The self-inductance coefficient is L, the mutual-inductance coefficient is M, and the coil resistance is R_s. The rotor angle is θ.

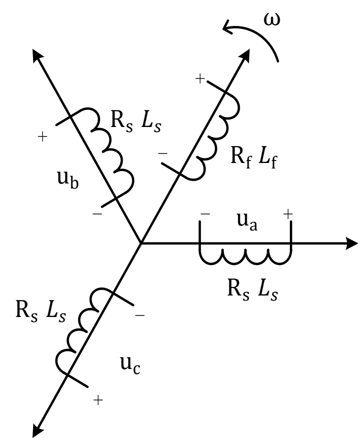

Figure 2-2 Structure of An Idealized Three-phase Round-rotor SG

In (2-1) below, $\underline{v}$ is the phase terminal voltage, $\underline{i}$ is the stator phase current and $\underline{e}$ is the back electromotive force (emf), which is also can be considered as the internal voltage as in Figure 2-1.

$$\underline{v} = \begin{bmatrix} v_a \\ v_b \\ v_c \end{bmatrix}, \ \underline{i} = \begin{bmatrix} i_a \\ i_b \\ i_c \end{bmatrix}, \ \underline{e} = \begin{bmatrix} e_a \\ e_b \\ e_c \end{bmatrix}; \tag{2-1}$$

Also, we define:

$$\underline{\cos}\theta = \begin{bmatrix} \cos\theta \\ \cos(\theta - \frac{2\pi}{3}) \\ \cos(\theta + \frac{2\pi}{3}) \end{bmatrix}, \ \underline{\sin}\theta = \begin{bmatrix} \sin\theta \\ \sin(\theta - \frac{2\pi}{3}) \\ \sin(\theta + \frac{2\pi}{3}) \end{bmatrix}; \tag{2-2}$$

The terminal voltage of SG can be written in (2-3) and (2-4) as follow,

$$\underline{v} = -R_s\underline{i} - L_s\frac{d\underline{i}}{dt} + \underline{e} \tag{2-3}$$

$$\underline{e} = M_f i_f \omega \underline{sin}\theta - M_f\frac{di_f}{dt}\underline{cos}\theta \tag{2-4}$$

where, M_f is the mutual inductance between stator winding and rotor winding; i_f is the field current and ω is the rotor speed.

Assuming that the field current of SG is constant, then the emf is rewritten as

$$\underline{e} = M_f i_f \omega \underline{sin}\theta \tag{2-5}$$

2.1.3 Mechanical Part of Synchronous Generator

The mechanical dynamics of an SG can be described by the “swing equation” [17]:

$$J\frac{d\omega}{dt} = T_m - T_e - D_p(\omega - \omega_0) - D_w\omega \tag{2-6}$$

$$\frac{d\theta}{dt} = \omega \tag{2-7}$$

where J is the moment of inertia of all parts rotating with the rotor. T_m is mechanical torque, T_e is electromagnetic torque. ω is the rotor speed, ω_0 is the reference rotor speed and θ is the rotor angle. Since the amortisseur windings are not included in the SE-based representation, a damping coefficient D_p is included to provide a damping torque proportional to the slip frequency $(\omega - \omega_0)$ which crudely represents the damping effects of the amortisseur windings in a real machine. The other damping coefficient D_w represents damping due to the windage loss.

The electromagnetic torque can be rewritten in (2-8) [22],

$$T_e = M_f i_f\left[i_a\sin(\theta) + i_b\sin\left(\theta - \frac{2\pi}{3}\right) + i_c\sin\,(\theta + \frac{2\pi}{3})\right] \tag{2-8}$$

The formula shows that the electromagnetic torque is related to phase currents, rotor angle, and virtual mutual flux $M_f i_f$.

For an actual SG, the mechanical torque is provided by the prime mover, and for the VSG controller, this power will be supplied by the dc side source. Thus, the dc source is equivalent to a virtual prime mover.

With the electrical and mechanical parts above, the whole SG model is now described. Based on the introduction above, the VSG controller can be built accordingly and is shown in the next section.

2.1.4 Structure of Swing Equation-Based VSG

The generated active and reactive powers can be calculated based on (2-9) and (2-10) as follows,

$$P = \omega M_f i_f \left[i_a \sin(\theta) + i_b \sin\left(\theta - \frac{2\pi}{3}\right) + i_c \sin\left(\theta + \frac{2\pi}{3}\right) \right] \tag{2-9}$$

$$Q = -\omega M_f i_f \left[i_a \cos(\theta) + i_b \cos\left(\theta - \frac{2\pi}{3}\right) + i_c \cos\left(\theta + \frac{2\pi}{3}\right) \right] \tag{2-10}$$

The above (2-6) to (2-8) can be summarized by the "frequency loop" block diagram in Figure 2-3. In the frequency loop, the inputs are the active power reference (P_{ref}) and the phase current feedback signal ($\underline{i}$) measured from the external system. The output of the system is the virtual rotor angle θ. The electromagnetic torque T_e can be calculated based on (2-8). The virtual mutual flux $M_f i_f$ is generated from the voltage magnitude loop.

In a real SG, the terminal voltage is controlled by an "exciter" via the applied field flux $M_f i_f$. A voltage magnitude control loop (shown in Figure 2-3) can be included which generates the desired $M_f i_f$ magnitude. In the diagram below with switches S_Q opened and S_V closed, a simple controller is used which acts on the scaled voltage magnitude error, i.e., $D_q(V_{ref} - V_m)$, where V_{ref} and V_m are the voltage reference and measured terminal voltage magnitude, respectively. Alternatively with switches S_Q closed and S_V opened, the desired $M_f i_f$ magnitude is generated based on the reactive power error, i.e., $(Q_{ref} - Q)$, where Q_{ref} and Q are reactive power reference and calculated system reactive power using equation (2.8), respectively.

Once the magnitude of the field flux is calculated by the voltage magnitude loop, three-phase voltage reference waveforms (e_a^*, e_b^*, e_c^*) for each of the corresponding phase voltages can be generated and sent on the firing pulse generator to generate the appropriate firing pulses to the IGBTs so that the generated internal voltage, say e_a has a fundamental component equal to e_a^*, etc.

Additionally, there is a magnitude detection block in Figure 2-3 to get the voltage magnitude from the voltage signal. Several methods can be used for magnitude detection. One of the designs is shown below.

Assuming a balanced three-phase voltage,

$$v_a = \sin\varphi \;, v_b = \sin\left(\varphi - \frac{2\pi}{3}\right), v_c = \sin\left(\varphi + \frac{2\pi}{3}\right) \tag{2-11}$$

We have

$$v_a v_b + v_b v_c + v_a v_c = -\frac{3}{4} v_m^2 \tag{2-12}$$

Where, v_m is the voltage magnitude.

Noted that a low-pass filter is needed in the VSG implementation to attenuate the ripple.

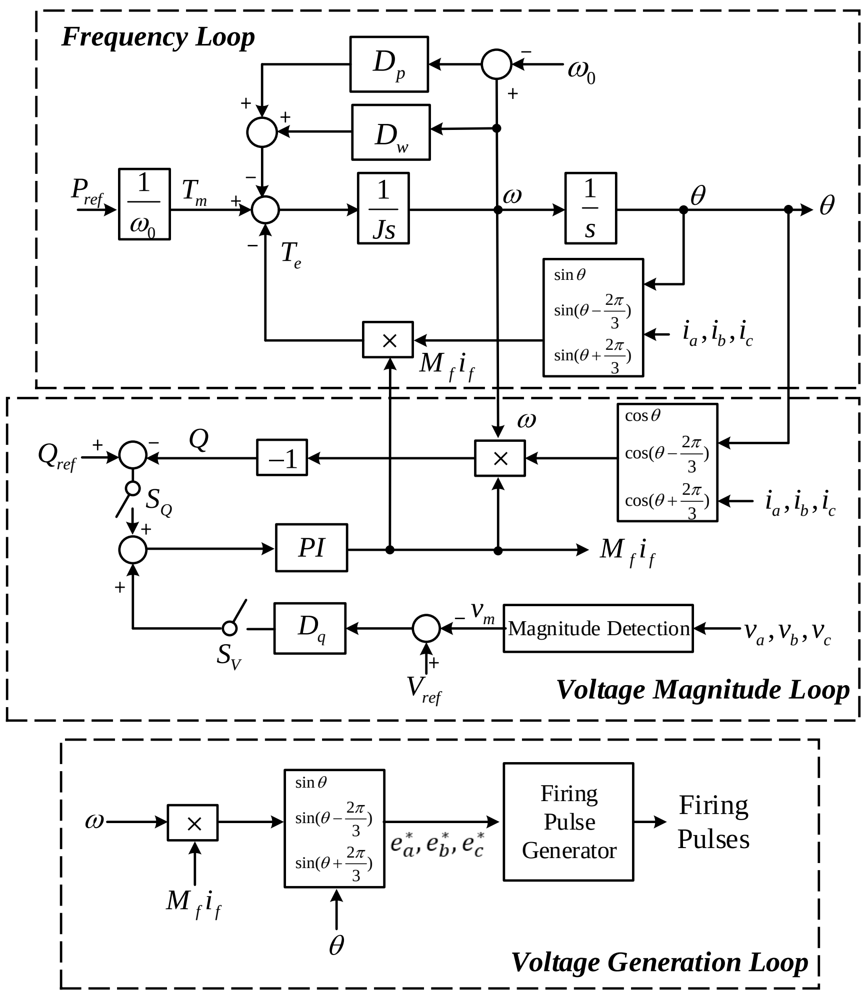

Figure 2-3 SE-based VSG (Sans Current Limiter)

2.2 Current Limiting Methods in Swing Equation Based VSG

Since the output currents are not the direct control variables of SE-based VSG, there is no inherent current limiting feature. Therefore, the SE-based VSG lacks the ability to limit over-current phenomena when a system fault or other unexpected situation happens. Some modifications can be added to the SE-based VSG to solve this problem.

The most popular current limiting methods nowadays are:

1) Multi-loop controller with an embedded current limiter
2) Virtual impedance controller
3) Switchable current limiting controller

This section first briefly introduces method 1 and method 2 and then discusses the switchable current limiting method in detail as it is the one used in the remainder of this thesis.

2.2.1 Current Limiting using Embedded Current Limiter

Multi-loop controller with an embedded current limiter is one type of grid-forming control. It has a cascaded control structure [32]-[36]. The typical structure is in Figure 2-4.

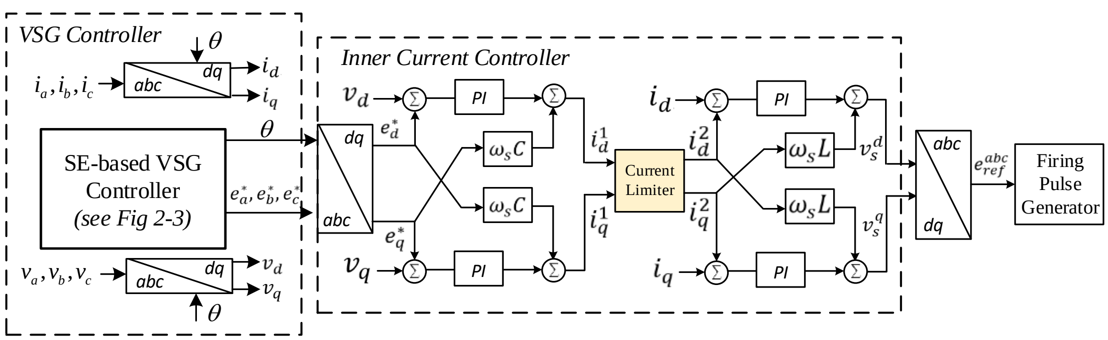

Figure 2-4 Typical Structure of Multi-loop Control with an Embedded Current Limiter

A downstream current control loop is inserted after the main VSC controller (which will be a SE-based VSG in this case). The voltage references e_a^*, e_b^*, e_c^* in Figure 2-3 could be directly used by the VSC to produce the voltage. However, doing so directly leaves no mechanism to control the current. Hence, the voltage orders are first converted to equivalent current orders which can be limited, as shown in the inner current controller in

Figure 2-4. This is a straightforward method to limit the current because the current reference is the control input, and its magnitude can be limited at this stage. Then the right-hand side decoupled controller generates the voltage orders v_s^d and v_s^q to achieve the limited current orders. These are converted back to polar quantities to produce the modulation voltages for the three phases.

Note that since the limiters are added to the current reference for the VSG type controller, once the current hits the limits, the converter becomes a constant current source which will lack the VSG's dynamic characteristics. Also inserting the current controller in series with the original VSG can deteriorate the dynamic behavior (e.g., increase the time constant) of the controller response [30]. Moreover, [28] shows that such VSG with embedded current controller may cause the converter to become unstable when it connected to a strong system due to the delays inherent to the PI controllers.

2.2.2 Current Limiting using Virtual Impedance Controller

Virtual impedance control is an over-current protection method used widely in grid-forming converters [37]-[39]. This method operates by reducing the amplitude of the converter reference voltage in case of any over-current. In this approach, the controller is given a characteristic that mimics the insertion of a series impedance on the ac side, by changing its ac voltage. Usually, a virtual resistor is chosen as the only component of the virtual impedance. A mixed impedance could have been an alternative, but it has been shown to give rise to poor stability [37].

The equivalent circuit of the converter with a virtual resistor connected to the grid is shown in Figure 2-5.

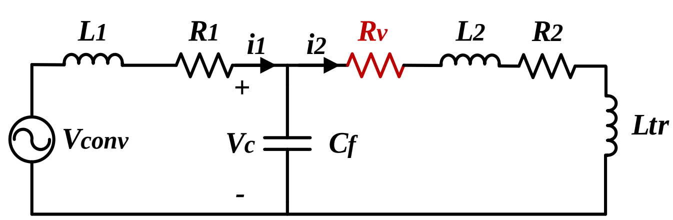

Figure 2-5 Single Phase Diagram of Converter Equivalent Circuit with Virtual Resistor

2.2.3 Switchable Current Limiting Controller

The two current limiting methods mentioned above both add an extra control loop inside the VSG, which introduces additional dynamics which detract from the principal role of the original VSG. The switchable current limiting controller is chosen in this thesis since it would not significantly deteriorate the original SE-based VSG.

In this current limiting method, the control strategy of the converter can be divided into two separated control blocks. One is the Swing-Equation (SE) based VSG discussed in Section 2.1 and another is the switchable current limiting controller as shown in Figure 2-6 [40]. The operation principle is concluded as follows:

1) Under the normal operation mode, the SE-based VSG is active.
2) When the over-current situation occurs, the converter will switch to the current limiting controller.
3) When the over-current situation clears, the VSG will be activated again.

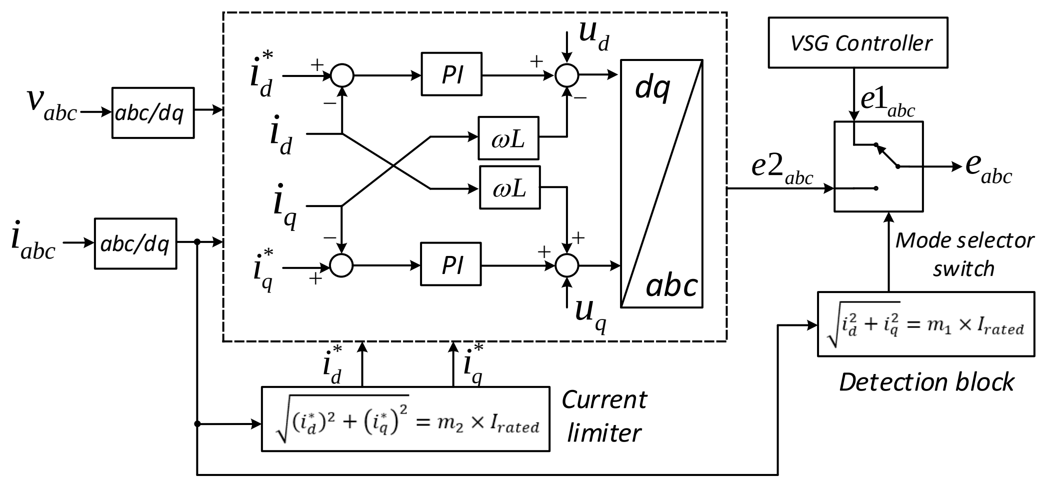

Figure 2-6 Switchable Current Limiting Loop

In the figure, the detection block with multiplier m_1 is used to monitor the system current. Assume I_{rated} is the current rating. Typically, m_1 is chosen from 1.2 to 1.5. With smaller m_1, the detection block has more sensitivity. When the measured output current magnitude $\sqrt{i_d^2 + i_q^2}$ is less than $m_1 \times I_{rated}$, the VSC is under the initial VSG controller, therefore, the VSC is controlled as a voltage source and is suitable in both grid-connected and islanded operations. However, if the current magnitude $\sqrt{i_d^2 + i_q^2}$ is larger than the pre-set value ($m_1 \times I_{rated}$), the controller will determine this as an unexpected over-current situation, and the mode selector switch is triggered to switch the control mode from VSG to the current limiting controller. It is desired to limit the current to $m_2 \times I_{rated}$ by generating d- and q-axis current orders i_d^* and i_q^* under this overcurrent situation. Normally, m_2 is chosen from 0.8 to 1.0. The PI controllers are used in this current limiting method to make the system current follow the current reference. After the fault is cleared and the output current recovers to the normal value, the controller is switched back to the VSG mode after a certain clearance time.

Besides the above-mentioned advantages, some problems also appear. For example, as a PI controller is used, the current may overshoot the reference transiently or have a slow response depending on the controller's gains.

2.3 Demonstration of Swing Equation Based VSG

With the aid of Electromagnetic Transients (EMT) simulation, this section demonstrates the dynamic operating behaviors of an MMC with the SE-based VSG. The widely used PSCAD/EMTDC© software was used as the vehicle for simulation in all system-level studies in this thesis.

The reason for selecting PSCAD/EMTDC© is its significant capabilities in modelling power systems that include HVdc and other power electronic equipment, and due to the wealth of expertise available to the author while at the University of Manitoba. This simulation software was originally developed at Manitoba Hydro by Professor D. A. Woodford and Prof. Ani Gole (University of Manitoba). It has also been used for the design and system studies of the majority of the world's HVdc systems, with a user base of approximately 50,000 internationally.

In this section, the SE-based VSG is demonstrated using an 11-level MMC system with switches S_Q closed and S_V opened. This ensures a PQ control mode in which the output active and reactive power are being regulation.

2.3.1 Demonstration System Layout

A simple transmission scenario with an 11-level MMC is shown in Figure 2-7. The strong ac system is represented by a voltage source and the Thevenin impedance $R_s + jX_s$. It is assumed that the remote converter controls the dc side voltage to its desired value of $\pm 5\ kV$. The main system parameters are in Table 2-1.

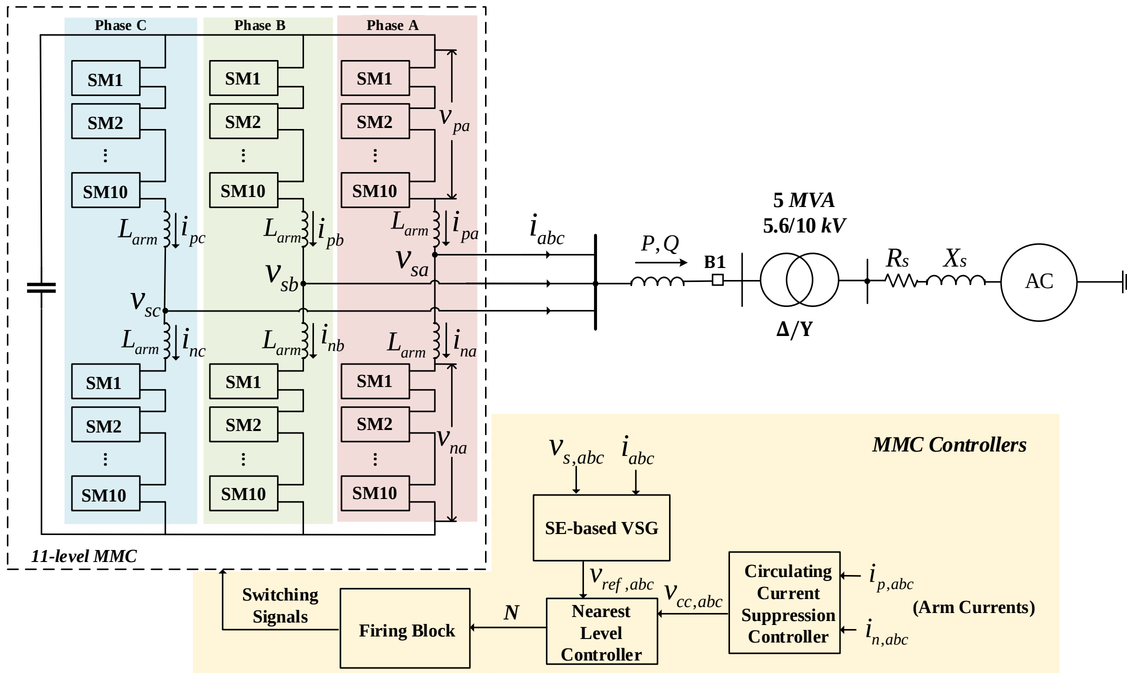

Figure 2-7 System Layout with 11-level MMC

Table 2-1 Main Parameters of MMC System

Parameter	Value	Parameter	Value
Dc side voltage V_{dc}	$\pm 5\ kV$	Transformer MVA	$5\ MVA$
Number of submodules /Arm	10	Transformer voltage	$5.6/10\ kV$
MMC arm inductance	$2\ mH$	Ac system rated voltage	$10\ kV$ (L-L, RMS)
Converter rated power	$5\ MVA$	System frequency	$60\ Hz$
Converter rated voltage	$5.6\ kV$ (L-L, RMS)	Ac system SCR	7.5

The parameters of the SE-based VSG (see Figure 2-3) and the switchable current limiting block (see Figure 2-6) are in Table 2-2 and Table 2-3, separately.

Table 2-2 Parameters of SE-based VSG

Parameter	Value	Parameter	Value
Reference active power P_{ref}	5.0 MW	Inertia J	0.5 s
Reference reactive power Q_{ref}	0.0 $Mvar$	Damping constant D_p	30
Voltage magnitude loop proportional gain factor K_p	0.0	Voltage magnitude loop integral time constant K_i	0.2
Damping constant D_w	0.0		

Table 2-3 Parameters of Switchable Current Limiting Controller

Parameter	Value	Parameter	Value
Rated current I_{rated}	1.0 pu	Multiplied constant m_2	0.9
Multiplied constant m_1	1.3	Control mode switch time	0.2 s

According to Table 2-3, the converter changes from the SE-based VSG to the current limiting block with $m_2 = 0.9$, when the system current magnitude is larger than $m_1 \times I_{rated} = 1.3\ pu$. And the converter changes back to SE-based VSG if the system current is lower than $1.3\ pu$ for $0.2\ s$.

In order to demonstrate the effect of the switchable current limiting block, the demonstrations are divided into two parts as followed in section 2.3.2 and section 2.3.3, which are the SE-based VSG *without* and *with* the current limiting block, separately.

2.3.2 Fault Recovery Demonstration Without Current Limiting Block

To validate the SE-based VSG, the system is simulated and allowed to reach a steady state. A three-phase to ground fault is applied at the secondary side (Y connection) of the transformer at 0.5 s, and the duration of the fault is $0.15s$ (9 cycles).

Figure 2-8 indicates the output active power P and reactive power Q.

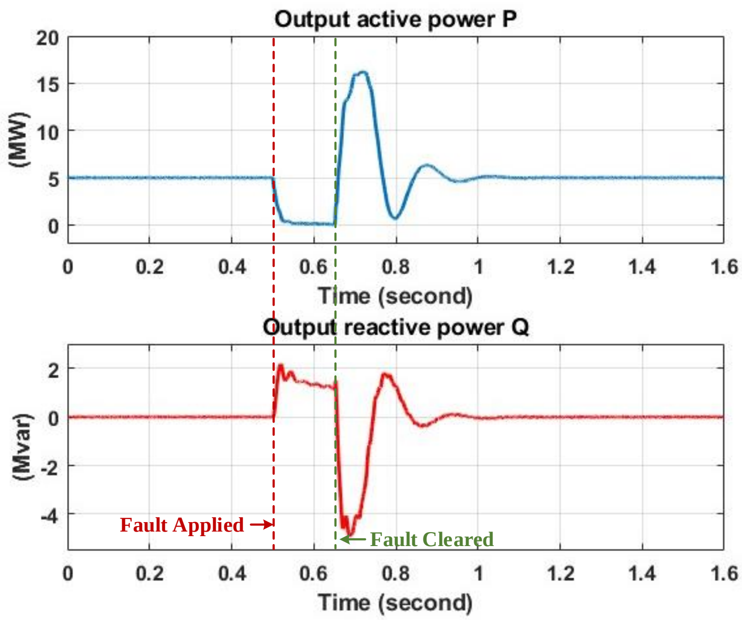

Figure 2-8 Waveform of Output Powers P and Q

Before the fault is applied, the system is under steady-state operation. The output active power P is approximately equal to $5.0\,MW$, and the output reactive power Q is regulated to be $0.0\,Mvar$. The results match the power references, which means the SE-based VSG can be operated under PQ mode successfully in the steady state. After the fault is cleared, the powers can recover to the same steady state, albeit with considerable oscillation which can be damped by introducing appropriate damping (not shown).

Figure 2-9 (a) (b) show the RMS value of the converter terminal voltages V_{RMS} and the instantaneous three-phase voltage waveforms v_{abc}, and Figure 2-9 (c) (d) show the RMS value of the output currents I_{RMS} and the instantaneous three-phase currents waveforms i_{abc}. Figure 2-10 is the MMC's upper arm current of phase a. During steady state, the three-phase voltages and currents are balanced. After the fault is cleared, the terminal voltages and output currents are able to recover to the same steady state quickly within about $400\,ms$.

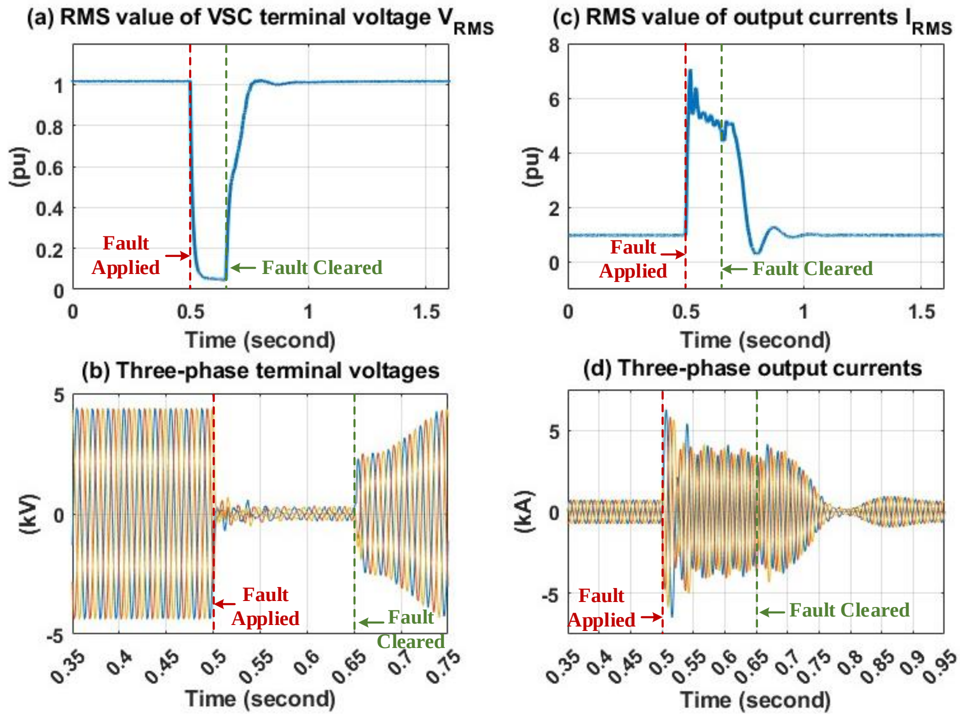

Figure 2-9 Waveforms of Terminal Voltage v_{abc} and Output Current i_{abc}

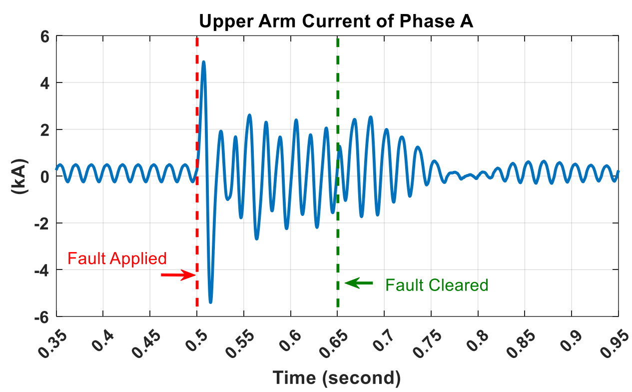

Figure 2-10 Waveforms of the Upper Arm Current of Phase a

A real SG's short circuit current is dependent on its internal voltage and transient impedance (X_d'', X_q'') and can be very large. In the above case, the SE-based VSG tried to mimic a real SG and consequently a similar high current ensues. The maximum output current reached almost $5.2\ kA$ (peak) and the maximum arm current reached around $5\ kA$ (peak) during the fault, which would cause over-current damage to the converter's delicate electronic component (IGBTs, etc.). This type of operation is not acceptable in a real converter system. Hence adding a current limiting feature is imperative as discussed in section 2.3.3.

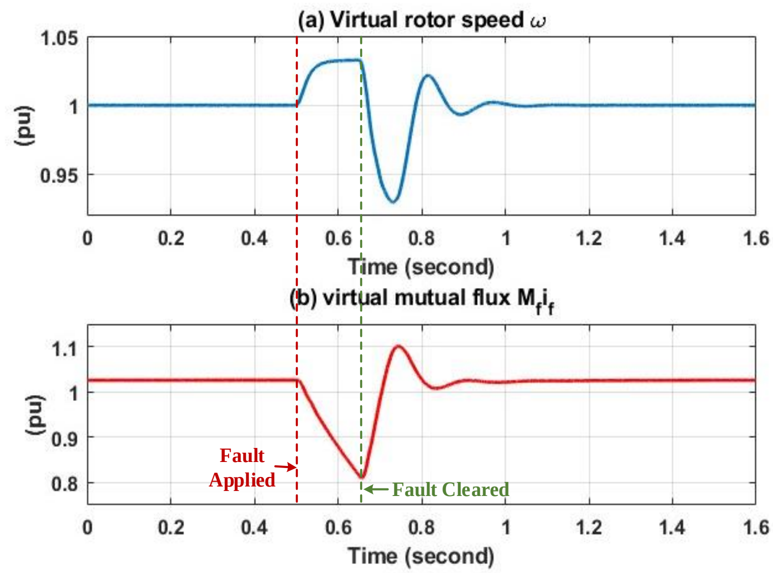

Figure 2-11 Output Variables from Frequency Loop and Voltage Magnitude Loop

Figure 2-11 shows the virtual rotor speed ω of MMC from the frequency loop and the virtual mutual flux $M_f i_f$ from the voltage magnitude loop. From Figure 2-11 (a), the converter can keep synchronism with the external system during the steady state. During the fault, the virtual rotor speed keeps increasing due to the near-zero output power during the short circuit, and the input power remains constant. Some oscillation happens after the fault is cleared. The virtual rotor speed of the MMC recovers to its nominal value and post-fault synchronization is achieved in this case. Therefore, the converter has fault ride-through capability. However, if the fault durations were longer, the virtual rotor speed and consequently the virtual rotor angle could increase causing a loss of synchronization with the external system.

Also, from Figure 2-11 (b), the virtual mutual flux $M_f i_f$ decreases during the fault and can recovery back to its nominal value when the fault is cleared. This indicates that the terminal voltage magnitude of the converter is under control.

2.3.3 Fault Recovery Demonstration with Current Limiting Block

To protect the converter from over-current damage, a switchable current limiting block is added. A three-phase-to-ground fault is applied at the secondary side (Y connection) of the transformer at 0.5 s, and the duration of the fault is $0.15s$ (9 cycles).

Figure 2-12 shows the output active power P and reactive power Q. Also, Figure 2-13 shows the RMS value of the converter terminal voltages V_{RMS} and the instantaneous three-phase voltage waveforms v_{abc}.

Before the fault is applied, the system reaches a steady state operation with $P = 5.0\ MW$ and $Q = 0.0\ Mvar$. The results match the power references, which means the SE-based VSG can be operated under PQ mode successfully in the steady state. Also, the three-phase voltages are balanced. After the fault is cleared, the system can recover to the same steady state at around $1.3\ s$ after an oscillation.

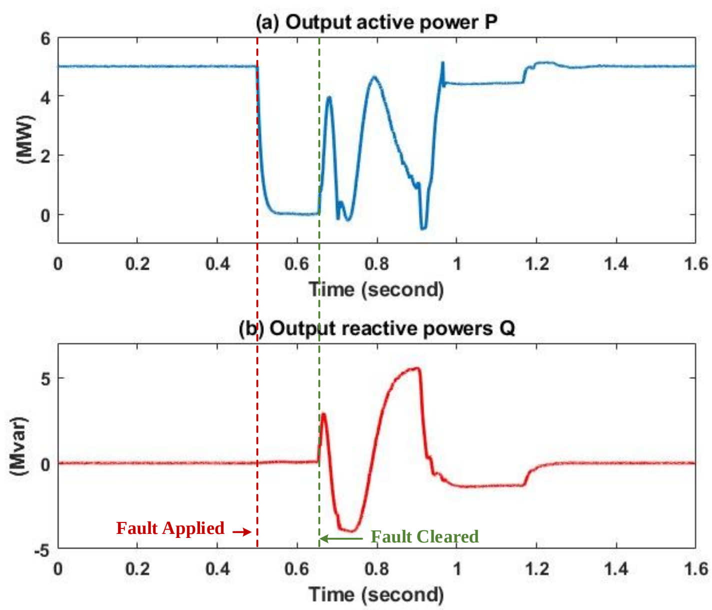

Figure 2-12 Waveforms of Output Active Power P and Reactive Power Q

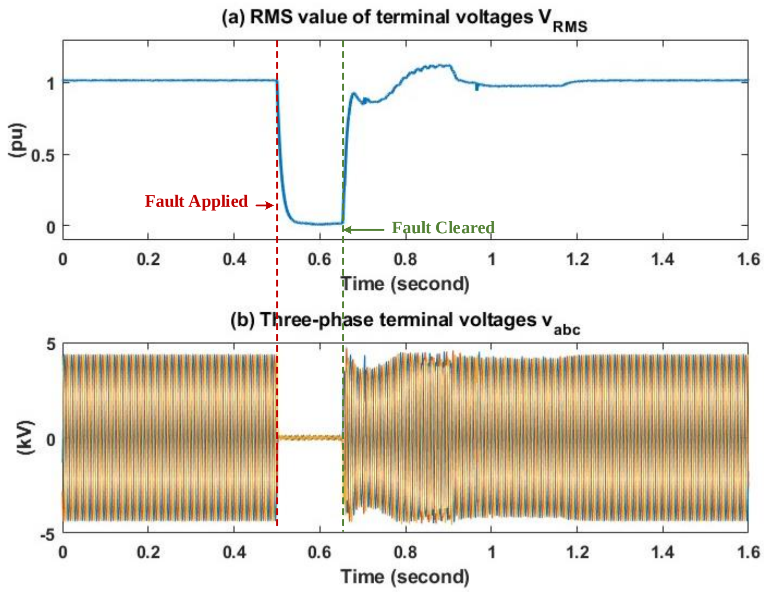

Figure 2-13 Waveforms of Terminal Voltage v_{abc} and its RMS Value

Figure 2-14 (a) is the signal which indicates the controller mode. Value ‘0’ means the MMC is operated as a SE-based VSG and ‘1’ shows the converter is in the current limiting mode. The irregular oscillation of the powers (see Figure 2-12) is caused by the multiple switches between the SE-based VSG and the current limiting mode.

It is notable that in a real SG, the rotor angular speed ω would keep increasing during the fault due to the excess of input power over output power. This brings risks of losing synchronism with the external system. Since the converter is not a real SG, the virtual rotor speed ω can be kept exactly at $1.0\,pu$ during the interval to prevent lost synchronism when the current limiting block is active. And when the converter is under the SE-based VSG, ω is released. This mechanism is referred to as ‘ω reset mechanism’.

Figure 2-14 (b) is the virtual rotor speed ω of the MMC with this reset mechanism. The converter can keep synchronism with the external system during the steady state. Also, the post-fault synchronization is achieved in this case since ω of the MMC recovers to its nominal value. Therefore, the VSC has fault ride-through capability.

Figure 2-14 (c) shows the magnitude of the output currents I_{mag}, which is equal to $\sqrt{i_d^2 + i_q^2}$ Also, the maximum allowable current of $1.3\,pu$ is shown with dotted line.

Figure 2-14 (d) shows the instantaneous three-phase current waveforms i_{abc}. Figure 2-15 is the MMC's upper arm current of phase a.

When the fault is applied at $0.5\ s$, the current magnitude increases and reaches $1.3\ pu$ at around $0.501\ s$. At the same time, the converter is switched to the current limiting block to regulate the current magnitude to $m_2 \times I_{rated} = 0.9\ pu$. A large fault current (about $1.5\ pu$) can be seen at the beginning of the fault. It is because the PI controller needs time to force the current equal to the references. Therefore, in the beginning, the converter faces risks of over-current.

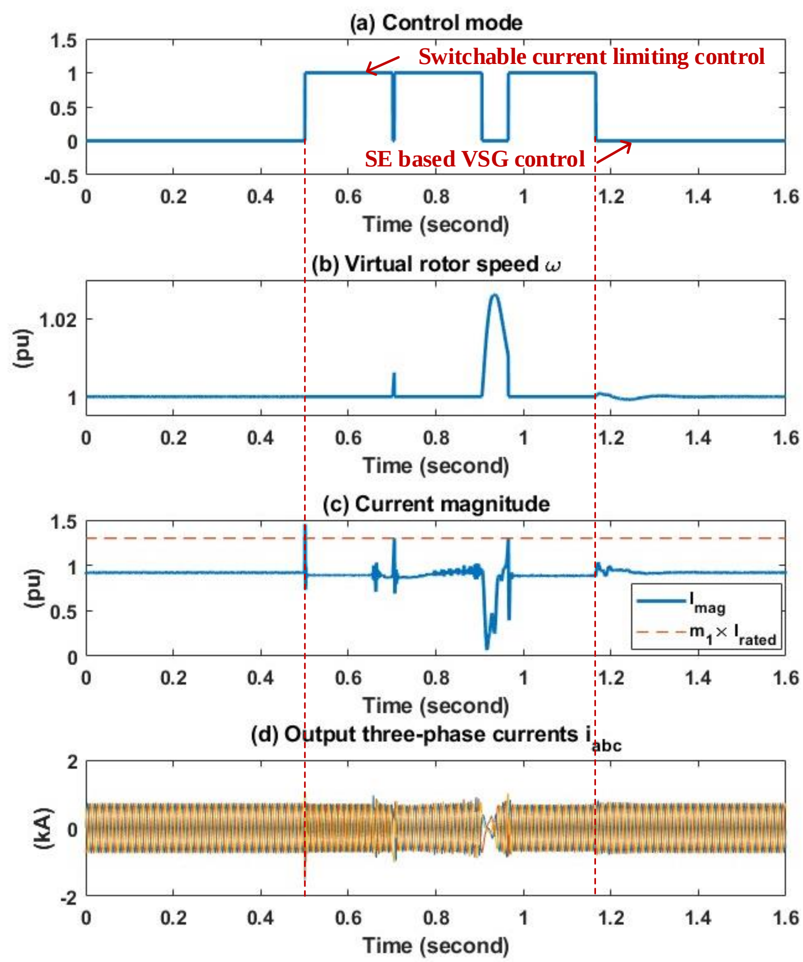

Figure 2-14 Virtual Rotor Speed ω and Current Magnitude I_{mag}

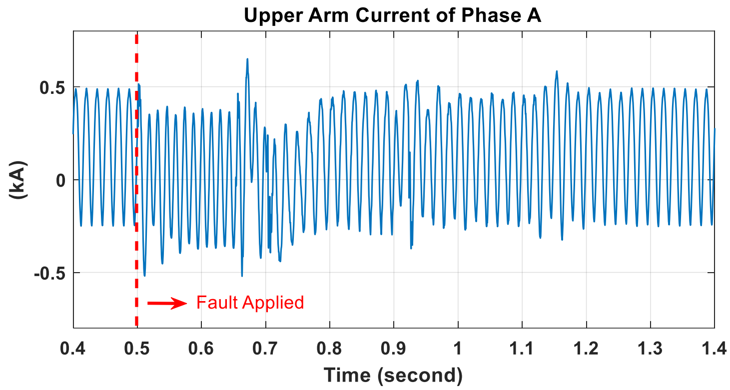

Figure 2-15 Waveforms of the Upper Arm Current of Phase a

After the fault is cleared, the SE-based VSG is active again at $0.704\ s$. Please note, when the VSG is re-selected, it raises the current too quickly, necessitating the second and third over current limitations. It is clear that the converter can be operated in a safe range during the whole operation.

2.4 Chapter Conclusion

The main content of this Chapter can be concluded as follows:

1. The Swing Equation (SE) based virtual synchronous generator (VSG) was introduced with details.
   a) This controller essentially models the mechanical dynamics of an actual synchronous generator (SG) but simplifies the electrical part. Therefore, the voltage source converter (VSC) with this kind of controller can mimic the behavior of the real SG. Therefore, all the experience obtained from the traditional SG can also be used.
   b) One advantage of the VSG method is that no communication system is needed between different converters to equitably distribute the power. This is because when the frequency changes due to power demand fluctuation, each VSG responds to this fluctuation according to its own damping factor and inertia constant.
   c) Moreover, the VSG can generate its own frequency and voltage order without the help of the phase-locked loop (required for the conventional

VSC controller) to obtain the timing reference. Therefore, this kind of controller can be used for connecting to passive loads or very weak systems. This advantage makes the VSG desirable in renewable energy interconnecting systems which are usually operated in low short circuit ratio (SCR) conditions.

2. Any VSG implementation must include current limiting to protect the valves from damage due to overcurrent. The switchable current limiting method was introduced in this Chapter and added to the SE-based VSG.
    a) Since the output currents are not the direct control variables of SE-based VSG, there is no inherent current limiting feature. Thus, some extra feature should be added, such as the switchable current limiting method.
    b) The switchable current limiting controller regulates the current within a safe range, only when the over-current situation occurs, therefore, it would not significantly deteriorate the original SE-based VSG function.
    c) Please note that as the PI controller is used in the current limiting block, the current may overshoot the reference transiently or have a slow response depending on the controller gains.
3. The SE-based VSG method and its switchable current limiting block were tested in Electromagnetic Transients simulation (PSCAD/EMTDC software) to validate the effectiveness.
    a) A simple MMC system was used to validate the control strategy.
    b) The simulation results show that the converter with the SE-based VSG can reach the desired steady state successfully. And the current limiting block regulates the valve currents to a safe range to prevent the over-current situation. Also, the converter can recover to the same operating point after a three-phase-to-ground fault, which proves the fault ride-through capability of the system.
    c) Moreover, the virtual rotor speed reset mechanism can prevent the converter from losing synchronism with the external system.

d) The oscillation currents may raise quickly to touch the ceiling limitation when operating mode is switched to SE-based VSG. Thus, the switchable current limiting block may be activated multiple times.

3 Parallel VSC-HVdc Links Feeding Passive Loads

The material in this chapter is published by the author as reference [23] C. Jiang, A. D. Sinkar, M. K. Das, A. M. Gole, and V. Pathirana, "A comparative study of master-slave control and virtual synchronous machine control for parallel VSC-HVDC links feeding passive loads on offshore platforms," in 15th IET International Conference on AC and DC Power Transmission (ACDC 2019), Coventry, UK, 2019, pp. 1-6. Adhering to IET copyright policy, it is being reproduced here for her own thesis with the above acknowledgment (https://acdc.theiet.org › media › iet-conference-paper-template).

This chapter describes the parallel operation of two 2-level VSC links for supplying power to an offshore oil platform intended for application in the North Sea. The SE-based VSG method (without the current limiting block) mentioned above is implemented and studied in this application system. For compassion between different control strategies, a widely used Master-Slave (M/S) strategy is also introduced briefly in this section. Different operating scenarios are discussed and tested in the EMT simulation program, such as load balancing, start-up of offshore induction motors, transferring and tripping of loads in case of failure of one of the links, and fault recovery and ride-through.

It demonstrates the automatic sharing of loads in a realistic application between VSCs without the need for communication when the SE-based VSG is implemented. On the other hand, the M/S controller requires communication and an additional Power Management Allocator (PMA) but is inherently better at current limiting.

This project involves collaboration with an industry partner. At the time of the research, two-level converters were typical for ratings under $350\ kV$ and $300\ MW$, and so were selected for these purposes. More recently, MMCs are also being used for lower ratings and could have also been used. In this preliminary study, current limiting was ignored in the simulations.

3.1 Project Introduction

Offshore oil and gas platforms are highly energy-intensive applications with power demands exceeding hundreds of MWs. Traditionally, gas-turbine generators on-site have been used to meet their power demands [41]. Nowadays, however, to reduce their carbon footprint, many projects have started utilizing VSC-based HVdc links to supply power from the onshore grid [42], [43]. This is also an economically attractive solution depending on the distance to the platform. Alternatively, multiple VSC-HVdc links can also be used to cater to their power demand to ensure higher reliability and to reduce production losses due to an outage of a single link [12], [44]. However, operating multiple VSC-HVDC links onto a passive, islanded system (like an offshore platform) gives rise to many technical challenges. These include bump-less synchronization of the VSC converters, coordination of their operation, sharing of the power demand without overloading any converter, and maintaining the voltage and frequency stability of the offshore grid in case of switching of different components/loads.

Two control strategies that are most effective for such applications are Master-Slave (M/S) control and Virtual Synchronous Generator (VSG) control of VSCs. The former strategy relies on the fact that there is a Master converter that sets the frequency and voltage of the offshore grid while the other converter (the Slave) follows it [45]. The latter strategy relies on controlling the VSCs such that they emulate the behavior of synchronous generators so that the control techniques used in traditional synchronous grids can be extended to these applications.

In this section, a comparative study of these two strategies is presented with different types of switching events simulated in an EMT simulation program (PSCAD/EMTDC).

3.2 Layout of Parallel VSC-Links System and Operation Mode

The layout of the system utilized for the simulation studies is shown in Figure 3-1 and the parameters of the different equipment are listed in Table 3-1 to Table 3-3.

Based on the system layout, it can be inferred that there are three modes in which the system can operate:

- Mode 1 (Non-parallel mode): In this mode, individual converters supply their local load with the interconnecting transformer branch open (due to a scheduled or forced outage).
- Mode 2 (Parallel mode): In this mode, both the converters are synchronized and share the load according to their individual ratings.

- <u>Mode 3 (Single converter mode):</u> In this mode, only a single converter supplies only the critical loads in the system in case the other converter is out of service (due to a scheduled or forced outage) with interconnecting transformer branch closed.

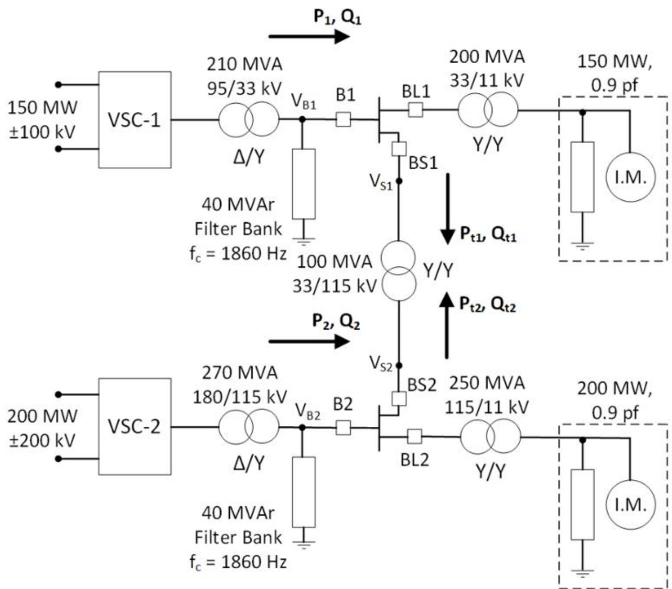

Figure 3-1 Parallel VSC-Links System

Table 3-1 Transformer Data

Transformer	VSC-1 Transformer	VSC-2 Transformer	Interconnecting Transformer	Load-1 Transformer	Load-2 Transformer
Rating	210 MVA	270 MVA	100 MVA	200 MVA	200 MVA
Voltage Ratio	95/33 kV	180/115 kV	33/115 kV	33/11 kV	115/11 kV
Connection	Δ/Y	Δ/Y	Y/Y	Y/Y	Y/Y
L_{sl}	0.15 pu	0.15 pu	0.07 pu	0.07 pu	0.07 pu
R_s	0.02 pu	0.02 pu	0.02 pu	0.02 pu	0.02 pu

Table 3-2 Induction Motor Data

Parameter	Value	Parameter	Value
Rated Power	12.5 MW	Rated Voltage	11 kV
R_s	0.021444 pu	X_{sl}	0.108546 pu
R_r	0.0333333 pu	X_{rl}	0.108546 pu
X_m	4.0 pu	Rated Efficiency	97.1 %
Rated Power Factor	0.9	Inertia (H)	2.0 s

Table 3-3 Filter Data

Filter	VSC-1 Filter	VSC-2 Filter
C_f	97.432 μF	8.0229 μF
L_f	75.147 μH	0.9126 μH
R_f	0.0878 Ω	1.0665 Ω

3.3 Master-Slave Control Method of Parallel VSC links

The Master-Slave (M/S) controller is introduced briefly, and this control method is also implemented in the parallel VSC system to compare with the proposed SE-based VSG strategy. Note that the M/S control method requires communication between the VSCs.

In M/S control strategy, one of the converters is designated as Master and the other is designated as Slave [12]. The Master converter's controller sets the frequency of the offshore grid. It also maintains its terminal voltage at its rated value. The Slave converter's controller tracks its terminal voltage using a phase locked loop (PLL) and provides the amount of active and reactive power according to the command it receives. To coordinate the operation of the two converters and to share the load changes based on their individual ratings, a hierarchical control structure can be used. This structure consists of a higher-level controller, called the Power Management Allocator (PMA), and lower-level control systems that control individual VSCs according to the commands received from the PMA.

3.3.1 Higher-level Controller

The Power Management Allocator (PMA) is shown in Figure 3-2.

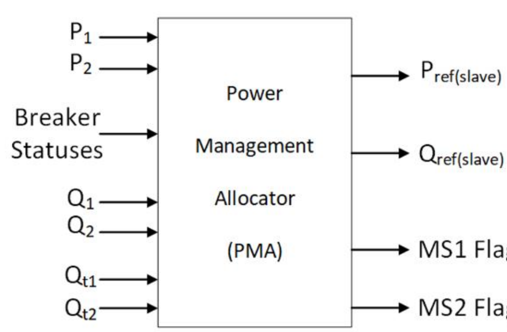

Figure 3-2 Power Management Allocator for M/S Control Strategy

This PMA block essentially performs two important tasks:

1. Decide which converter is the Master converter and which is the Slave converter.
2. Provide active and reactive power commands to the Slave converter to share the load according to individual ratings.

The PMA generates the active and reactive power order for the Slave converter using (3-1) and (3-2) respectively.

$$P_{ref(slave)} = \frac{P_{rated(slave)}}{P_{rated(total)}} \times (P_1 + P_2) \tag{3-1}$$

$$Q_{ref(slave)} = \begin{cases} (Q_1 - Q_{t1}) & \text{if } VSC1 \text{ is slave} \\ (Q_2 - Q_{t2}) & \text{if } VSC2 \text{ is slave} \end{cases} \tag{3-2}$$

Here, $P_{rated(slave)}$ is the available rating of the Slave converter while $P_{rated(total)}$ is the total available rating of the Master and the Slave converters. All the other quantities are as given in Figure 1. The reactive power order is generated in such a way that the reactive power flow on the interconnecting transformer branch is kept as low as possible (when operating in Mode 2). If the Slave converter provides the demanded power, the master converter provides the remaining power (i.e., the slack).

3.3.2 Lower-level Controller

The block diagram of the lower-level control system is given in Figure 3-3. The well-known dq-based control system has been used for individual VSCs. Since there is an inner current control loop present in this type of control, it is possible to have faster control of VSC currents so that the converters do not get overloaded even during transient operating conditions.

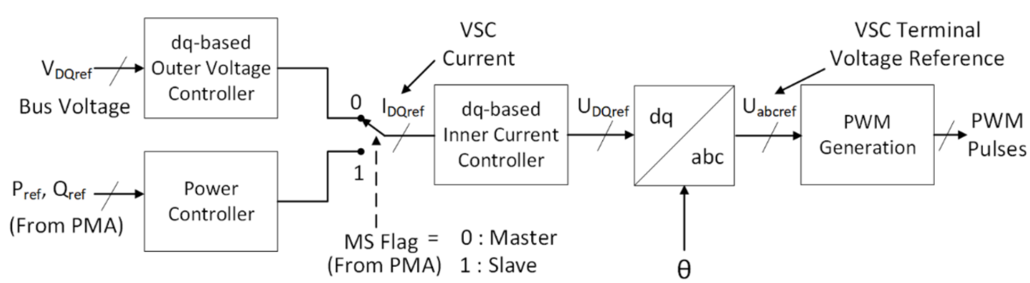

Figure 3-3 Lower-level Control System for individual VSCs

For the Master converter, MS Flag is equal to '0'. While for the Slave converter, MS Flag is '1'. The angle θ shown in Figure 3-3 comes from a PLL. Since any one of the two converters could be Master/Slave, these controls are duplicated for each of the VSCs.

3.3.3 Synchronization Mechanism used in M/S Control

Assume the system is operating in Mode 1. So, the MS Flag in Figure 3-3 is equal to 0 for both converters. Say it is decided to switch to Mode 2 with VSC-2 as Master and VSC-1 as Slave. Breaker BS2 in Figure 3-1 is closed and the PMA gives the command to VSC-1 to become the Slave. Following this, the PLL of VSC-1 starts tracking the voltage V_{S1} (see Figure 3-1). When the phase difference between V_{B1} and V_{S1} becomes 0, the breaker BS1 is closed. On successful synchronization, VSC-1 is the Slave converter and supplies the active and reactive power as commanded by the PMA.

3.4 Swing Equation Based VSG Method

The operating mechanism of the SE-based VSG was introduced before, which will not be repeated here. Only the special aspects related to the VSC parallel operation are explained in this section.

3.4.1 Load Sharing in VSG Controller

In a synchronous grid, the variations in active and reactive power are shared amongst the connected generators using frequency and voltage droop mechanisms. This is a very elegant and, most importantly, decentralized way of sharing the load (i.e., it doesn't rely on any communication between machines). When the active power demand changes, there is a change in the speeds (ω) of the machines due to changes in their individual T_e. The prime mover system of each machine then changes its power inputs in such a way that the new power balance is achieved.

This concept can be extended to work in the case of VSCs controlled using SE-based VSG method as well. The parameter D_P in the swing equation (2-6) usually represents the mechanical friction in an actual machine. But it's a well-known fact that the effect of droop control is equivalent to an increase in the constant D_P. So, for VSG, the constant D_P in frequency loop (see Figure 2-3) represents the mechanical friction plus the frequency droop coefficient. Similarly, the quantity D_q in voltage magnitude loop (see Figure 2-3) represents the voltage droop coefficient for sharing the reactive power demand.

3.4.2 Selection of D_p and J for SE-based VSG

To ensure proper load sharing when using VSG controller, it's important to properly select the different parameters of the control system shown in Figure 2-3. The different parameters to be selected are D_P, J, D_q and K.

Connecting both converters into the same ac system requires a common frequency. Thus, $\Delta\omega_1 = \Delta\omega_2 = \Delta\omega$ (say), where $\Delta\omega = (\omega - \omega_0)$. If we want that the ratio of powers supplied by each VSC to be the same at all operating points, i.e., $P_1/P_2 = n$, then from the steady state analysis of (2-6), it can be shown that the ratio of the droops (D_{P1}/D_{P2}) is also equal to n. This gives a droop characteristic as shown in Figure 3-4.

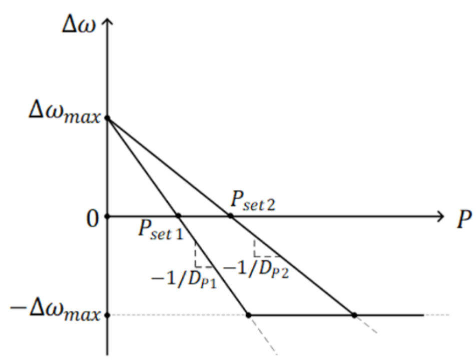

Figure 3-4 Frequency-Active Power Droop Characteristic

Here, $\Delta\omega_{max}$ is the maximum change in the frequency when the load changes from $(P_{set1} + P_{set2})$ to 0. Typically, this is taken to be about $3\,\%$ to $5\,\%$ of the nominal frequency. From Figure 3-4, it can be easily shown that:

$$|D_{P1}| = \frac{P_{set1}}{\Delta\omega_{max}}\ ,\ |D_{P2}| = \frac{P_{set2}}{\Delta\omega_{max}} \tag{3-3}$$

Now, looking at the frequency loop in Figure 2-3, we can say that its time constant τ_P is given by (3-4). The time constant τ_P is a design parameter that must be selected based on the bandwidth that is desired.

$$\tau_P = \frac{J}{D_P} \tag{3-4}$$

So once τ_P, n and $\Delta\omega_{max}$ have been selected, D_{P1}, D_{P2}, J_1 and J_2 can be easily calculated using (3-3) - (3-4) and $D_{P1}/D_{P2} = n$. Similarly, D_{q1}, D_{q2}, K_1 and K_2 that are used in the voltage magnitude loop Figure 2-3 can also be calculated.

3.4.3 Synchronization Mechanism used in SE-based VSG

Assume the system is operating in Mode 1. To synchronize the two VSCs, firstly breaker BS2 is closed (see Figure 3-1). Once this breaker is closed, an automatic control system starts tracking the phase difference between the voltages V_{B1} and V_{S1} (see Figure 3-1) and changes the P_{set1} based on this. This in turn changes ω_1 in such a way that the phase difference between the voltages V_{B1} and V_{S1} starts decreasing. When the phase difference becomes zero and stays within a tolerance band for a predetermined amount of time, the breaker BS1 is closed. On successful synchronization, this auxiliary control system used for synchronization can be deactivated.

3.5 Simulation Demonstration

This section presents the results of the simulations performed in PSCAD/EMTDC© to compare the two schemes under different dynamic scenarios. For M/S controller, in all the cases presented here, VSC-2 is the Master, and VSC-1 is the Slave.

3.5.1 Load Sharing After a Step-change in Load

Figure 3-5 shows the response of both VSG as well as M/S controller for an increase in the load by 50 MW at $t = 1\ s$. Both strategies are effective in ensuring the sharing of the change in the load according to the individual ratings of the VSCs. The only difference is that in M/S controller, the frequency of the system always comes back to nominal frequency after a load change while in SE-based VSG controller, the frequency drops when the load increases.

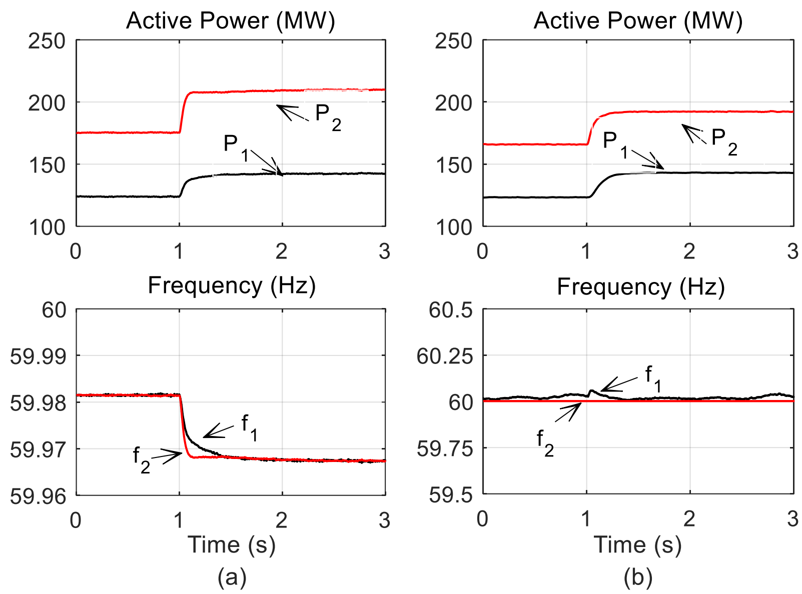

Figure 3-5 Effect of Step Change in the Load; (a) SE-based VSG, (b) M/S Controller

A slower outer control loop named 'secondary frequency regulation' can be utilized for changing P_{set1} and P_{set2} in a coordinated fashion to bring the frequency back to its nominal value, which is given in Figure 3-6 below.

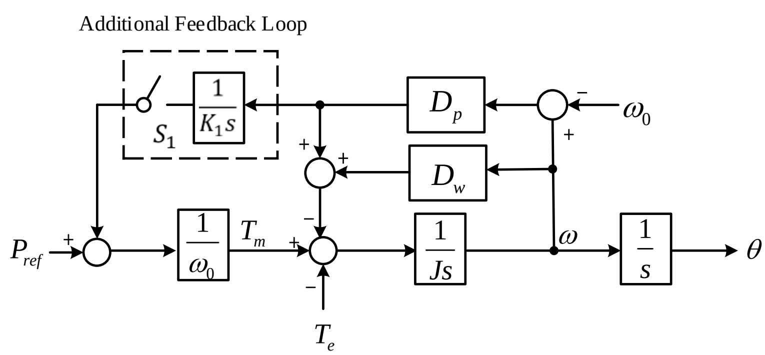

Figure 3-6 Secondary Frequency Regulation Loop

3.5.2 Direct-On-Line (DOL) Starting of Induction Motor

Typically, the majority loads on an offshore platform are high-power induction motors. To check the viability of M/S controller as well as VSG controller, their response is recorded for a Direct-on-Line (DOL) start of a $14\,MVA$ induction motor. Figure 3-7 shows the responses for both cases. The induction motor has been started at $t = 1\,s$ at the bus near to VSC-2. The mechanical load on the motor is assumed to be a pump-type of load (i.e., $T_L \propto \omega^2$).

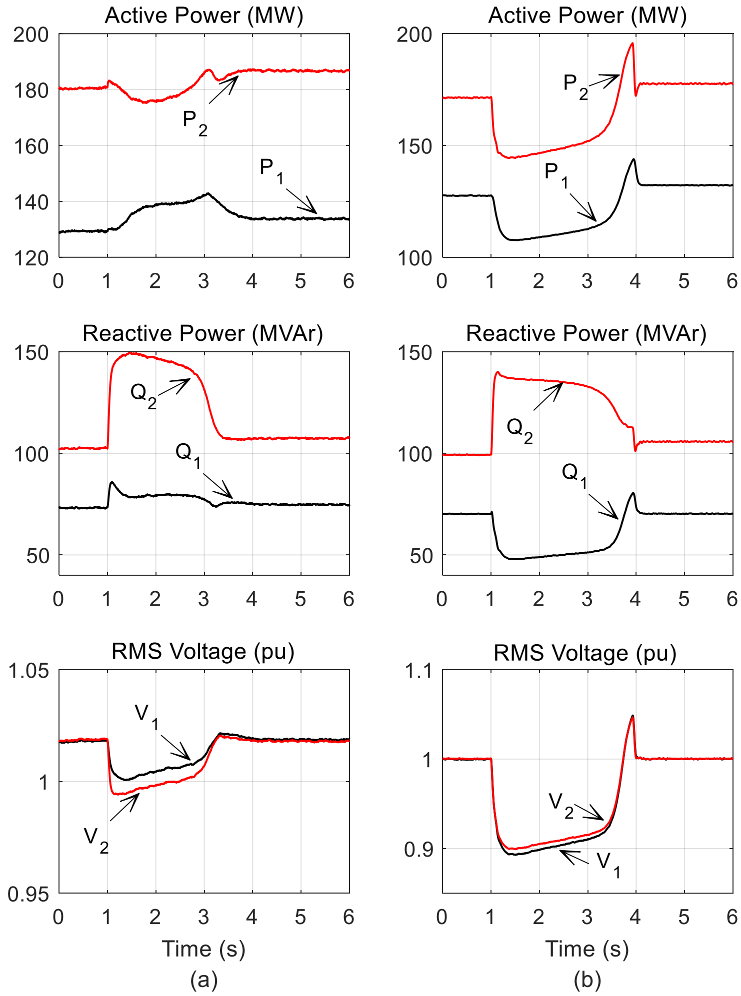

Figure 3-7 Induction Motor DOL Starting; (a) SE-based VSG, (b) M/S Controller

The DOL start is successful in both cases. It takes about $3\ s$ for the machine to reach its rated speed. The only difference is in the fact that the voltage sag in the case of M/S controller is higher (about $10\ \%$) than with SE-based VSG (about $3\ \%$).

This can be attributed to the fact that M/S controller has an inherent current limiting capability (due to the decoupled i_d-i_q control loops), unlike the VSG presented here. So, when the induction motor is starting and if the Q demand is higher than the ratings of the converters, then M/S controller will just limit the converter's output current to avoid overloading the converters. No such mechanism is available for the VSG presented here.

3.5.3 Tripping of a Link

One of the critical contingencies for a system with parallel VSC-HVDC links is the tripping of one link and subsequent changeover from the synchronized operation of both converters (Mode 2) to one converter supplying the entire load (Mode 3). This is particularly critical in the M/S control case when the Master converter trips (since it is maintaining the voltage and the frequency of the offshore grid).

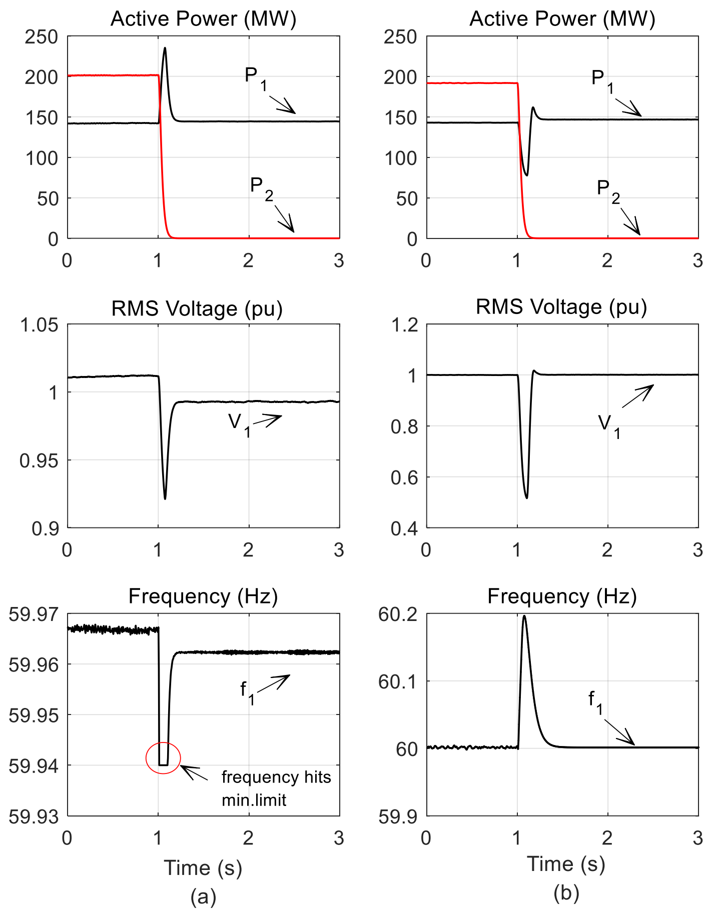

Figure 3-8 Effect of Tripping of VSC-2; (a) SE-based VSG, (b) M/S Controller

Figure 3-8 presents the responses of both cases when VSC-2 is tripped at $t = 1\,s$ (VSC-2 is the Master for M/S controller).

For M/S controller, when the Master converter trips, two extremely critical things need to be accomplished:

1. Detecting that the Master converter has tripped and changeover of the Slave to Master.

2. Issuing transfer trips to non-critical loads to ensure that the total load stays within the rating of the surviving converter.

There are delays associated with each of these steps and if these delays are too large, then the voltage may sag to a very low value (as in Figure 3-8 (b)) and lead to a total outage. Hence, care needs to be taken to deal with this case in the field.

On the contrary, there are no such special requirements for SE-based VSG. Since the VSCs share the load in a completely decentralized manner, the changeover from Mode 2 to Mode 3 becomes relatively easier. The only critical point is that the transfer trips need to be given quickly to avoid overloading a converter (notice the sharp increase in the active power for SE-based VSG in Figure 3-8 (a)). In addition, the current limiting mechanism should be added to protect the converters. But, as seen in Figure 3-8 (a), for SE-based VSG, the frequency falls on overload. So, tripping of non-critical loads can be accomplished using under-frequency relays that utilize local measurements at load busses.

3.5.4 Fault Ride-through and Recovery

It is very important to study how fast these two schemes ride through and recover following a fault in the offshore grid. In the simulation, a three-phase fault occurs at $t = 0.1\ s$ on a $50\ MW$ feeder near VSC-1's bus. The fault is cleared after $0.1\ s$ by tripping the corresponding feeder. Figure 3-9 presents the post-fault recovery for both cases.

It can be inferred from Figure 3-9 that the recovery of the SE-based VSG is faster (about $0.12\ s$) than the M/S controller (about $0.27\ s$). This can be attributed to the fact that in SE-based VSG, the VSC's output voltage is controlled while in M/S controller, the VSC's output current is controlled. Since all the loads are passive in an offshore platform, the recovery with a voltage-controlled device is expected to be faster compared to the case with a current-controlled device. Also, there are inherent delays in the decoupled current controller since the PI controllers are used.

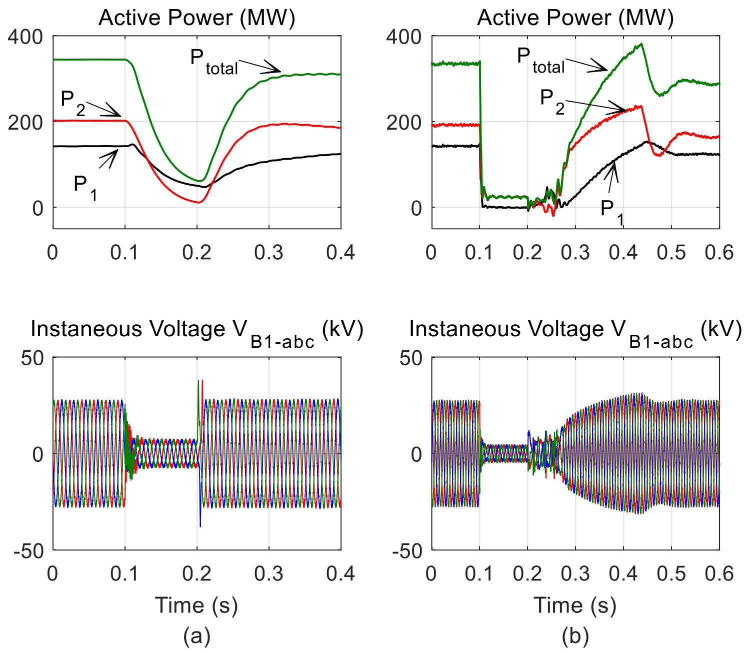

Figure 3-9 Post-fault Recovery; (a) SE-based VSG, (b) M/S Controller

3.6 Chapter Conclusions

Based on the discussions and the simulation results in this chapter, the following inferences about the two control strategies can be drawn:

- The SE-based VSG method is shown to be a good solution for offshore platforms when it comes to multi-vendor implementations since the load can be shared automatically in a decentralized manner without the need for PMA.
- The frequency always comes back to the nominal value following a disturbance in M/S controller. To accomplish this in the SE-based VSG, an additional slower outer control loop may have to be used which changes P_{set1} and P_{set2} in a coordinated fashion.
- Handling the case of tripping a link is relatively easier for the SE-based VSG than the M/S controller. In the M/S control method, there is a need for a mechanism to detect that the Master converter has tripped. No such special requirement is there for SE-based VSG.

- In the case of SE-based VSG, unassisted post-fault recovery is faster than with the M/S controller. This is because, in VSG, the VSCs are voltage-controlled devices while in M/S controller, they are current-controlled devices.
- There is no <u>inherent</u> mechanism to avoid overload of a VSC in the case of SE-based VSG. Thus, the SE-based VSG requires an additional current limiter, e.g., a switchable current limiting block. In the case of M/S controller, this can be easily accomplished using the inner current control loop present in the lower-level controls.
- In the case of M/S controller, providing redundancy for the central coordinating controller is very critical to counter total failures. No such redundancy is required for SE-based VSG.

4 Novel Hysteresis Current Control for MMC Using Acceleration Current Slope

This work has been filed as US Provisional Patent Application No. 63/502,189, May 2023.

The voltage source interfaced Swing Equation based VSG introduced in Chapter 2, has no inherent current limiting capability. An additional feature such as the switchable current limiting block must be added to regulate the overcurrent.

What if the voltage source converter (VSC) can be given the characteristic of the real synchronous generator and implemented as a stiff current source at the same time? Then the inherent current limiting function can be implemented easily and straightforwardly by simply limiting the magnitude of the current reference. The VSG with embedded current controller mentioned above in section 2.2.1 could be one option. However, as shown later in Chapter 6, with this option, the system becomes more susceptible to instability when the short circuit ratio (SCR) is large due to the delays inherent within the PI controller [28]. To overcome this potential instability, this chapter introduces a new approach. Using the proposed method, the VSC is controlled as a current source with very fast dynamic response.

4.1 Introduction

Traditionally, the hysteresis current control (also referred to as current-reference PWM) has been long used with two-level VSCs [46] to follow a given reference current. This method is summarized in section 4.3.

However, the application of this method with the modular multilevel converter (MMC) has not been widely investigated due to the complexity of its structure. Thus, the control strategy which can make the MMC behave as a high-bandwidth and high-precision current source is the subject of this Chapter. The example used in this chapter to demonstrate the working of the proposed hysteresis control method designed for MMCs is the active power filter (APF), which is often used for controlling arc furnace flicker as in Figure 4-1 [47].

Then Chapter 5 will use this control method to build a current source interfaced VSG strategy.

The operating principle of an APF is that it identifies the undesirable component of the load current and injects a canceling component into the grid to offset this [48]. Additionally, a converter-based APF can simultaneously provide reactive power compensation, regulation of terminal voltage, and voltage balancing in three-phase systems.

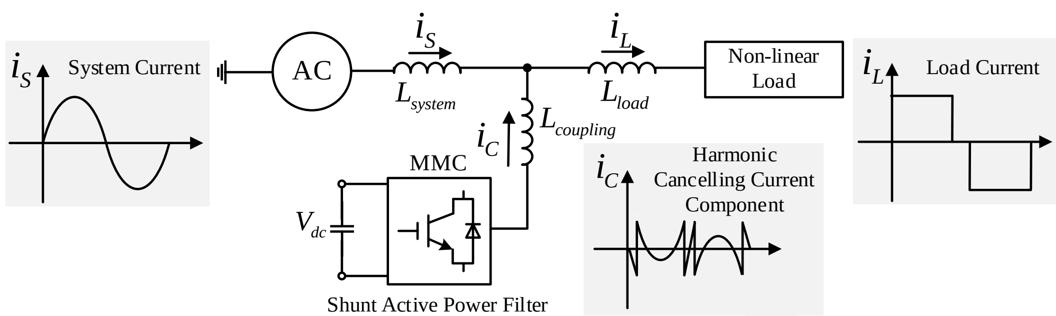

Figure 4-1 System with Shunt Active Power Filter

The structure of this chapter is as follows. The traditional hysteresis current control for the two-level VSC is first introduced briefly and its advantages and disadvantages are presented. Then a novel hysteresis current control method for the MMC using an acceleration slope strategy is developed. This proposed method can be directly applied without modifications to MMCs with any number of levels. The effectiveness of the proposed method is validated using Electromagnetic Transients (EMT) simulation. A method to determine the power loss is used to estimate switching and conduction power loss [49]-[50]. It is shown that the MMC option can greatly reduce the switching power loss as well as provide an improved output waveform in comparison with the existing hysteresis control for a two-level VSC. Finally, an application example of an MMC-based APF is demonstrated using EMT simulation and is also constructed and tested using a hardware-in-loop (HIL) simulation on a real-time digital simulator (RTDS).

4.2 Existing Current Control Methods for MMC

Current control methods for the VSC can be classified as i) linear controller and ii) nonlinear controller [51]. In the linear controllers, a voltage order is generated using a proportional-integral (PI) controller. This type of control is more suited for low-bandwidth applications such as reactive power balancing but is too slow for active harmonic filtering or for cleaning up arc furnace current waveforms [47].

For the latter, non-linear control method such as hysteresis current, delta modulation, and space vector are recommended. Space vector method or nonlinear vector current source (NLVCS) control strategy is discussed in [52]. The NLVCS algorithm is based on space vectors, and it has good robustness against the system operating changes compared with the linear current control method mentioned before. It also has a fast current dynamic response. However, the algorithm requires the instantaneous voltage and current variables to be transformed into two-dimensional vectors through αβ transformations. Usually, the transformation angle is measured through the phase locked loop (PLL) component installed in the system and it is well known that the PLL may fail to measure the correct angle value if the system response is fast. Moreover, the two-dimensional transformation only obtains the information of specific frequency, and it does not appropriate for the voltage and current variables with lots of harmonics components. Therefore, this NLVCS method is mainly suited for the active filtering of one or two specific harmonics, whereas the hysteresis current control method introduced in this chapter can target a broad range of harmonics.

The hysteresis modulation method is popular and has been applied to multilevel H-bridge converters, diode-clamped converters, and flying capacitor converters [53]. One of the challenges with hysteresis controller is the higher switching power loss, especially in two- or three-level controllers, where the output voltage swing at each switching is very large. However, MMCs afford the opportunity to have a switching step which is a very small fraction of the step in a two-level converter, and so have the potential for significantly reducing switching loss. Although MMCs are seeing increasing use in HVdc and other applications, the hysteresis current control method for MMC and its power loss analysis have not been further investigated.

Reference [54] suggests a hysteresis current controller with an MMC using a fixed sampling timestep. In this method, the MMC has to change its output voltage every sampling timestep which results in a large number of switchings and so potentially a higher switching loss. Alternatively, the proposed method in this thesis makes a judgement based on difference between current error and hysteresis width in each sampling timestep to decide whether the MMC needs to change output voltage. Thus, the MMC may keep voltage level unchanged over several sampling timestep. This results in fewer switch operations.

4.3 Traditional Hysteresis Current Control for Two-level VSC

Hysteresis current controller in Figure 4-2 is a popular non-linear control method used for two-level VSCs. The objective is to keep the output current (i) within a narrow band defined by a lower and upper threshold around the reference current (i_{ref}) [46].

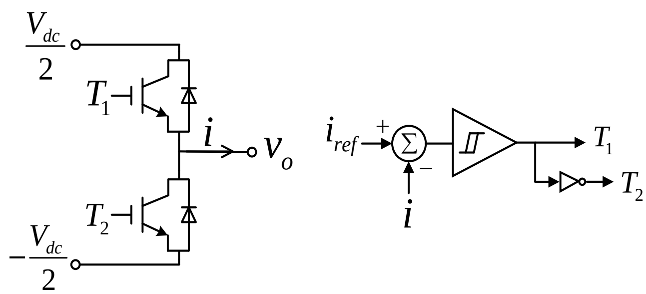

Figure 4-2 Example System for Traditional Hysteresis Current Controller.

Traditional hysteresis current controller uses a simple “bang-bang” control strategy. Figure 4-3 shows typical waveforms for this type of control. If the actual current (i) falls below the lower threshold (e.g., time t_1), the output voltage (v_o) is switched to positive dc rail ($\frac{V_{dc}}{2}$) by triggering T_1. As a result, the current increases, and traverses toward the upper threshold. Similarly, v_o is switched to the negative dc voltage ($-\frac{V_{dc}}{2}$) by triggering T_2 when the current breaches the upper threshold (e.g., time t_2). Thus, the currents can be regulated within the pre-set envelope. However, only the current direction and not its rate of change is controllable because the two-level VSCs only have two voltage options which are positive or negative dc voltage, and the rate of rise/fall depends on the back emf of the load.

This chapter introduces a novel hysteresis current control method for the MMC using an acceleration slope. With this new type of controller, the output currents of the MMC can be limited within a pre-set hysteresis band and the change in voltage at each switching will only be a small fraction of the full voltage range, so the corresponding power loss can be much reduced. Furthermore, the slope of the current can also be controlled.

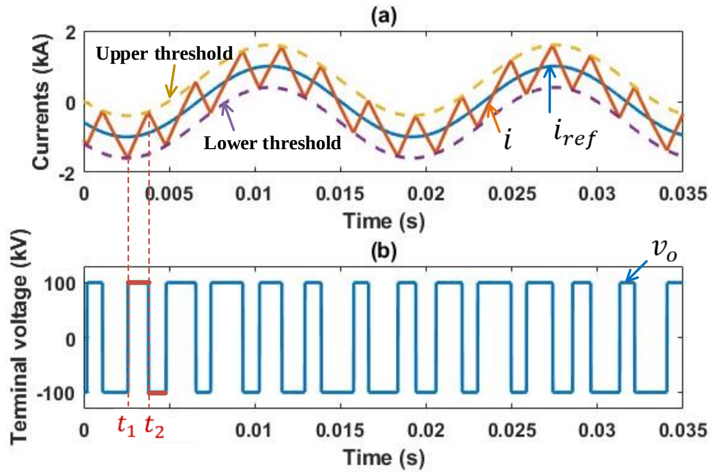

Figure 4-3 Typical Waveforms with Hysteresis Current Controller for a Two-level Voltage Source Converter. (a) Currents. (b) Terminal Voltage

4.4 Novel Hysteresis Current Control Using Acceleration Current Slope

The section describes a principal contribution of this thesis. It shows how the MMC can be adapted to conduct a rapidly controllable current source.

4.4.1 MMC Topology and its Simplification

The equivalent circuit model of the three-phase MMC structure is shown in Figure 4-4. The upper and lower arm submodules are represented by the voltage sources ($v_p^{abc} = [v_{pa}, v_{pb}, v_{pc}]^T, v_n^{abc} = [v_{na}, v_{nb}, v_{nc}]^T$) and L_{arm} is the arm inductance. The superscript '*abc*' denotes a vector of the individual phase $[a, b, c]$ quantities. Reference [55] shows that the voltages v_{a1} and v_{a2} at points a_1 and a_2 in phase 'a' (and corresponding points on the other arms) are approximately equal.

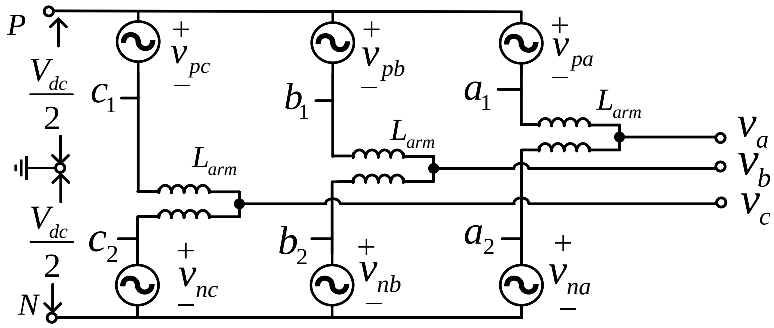

Figure 4-4 Equivalent Circuit Model of MMC.

Therefore, Figure 4-4 can be simplified as shown in Figure 4-5 by "virtually" connecting these approximate equipotential points (a_1&a_2, b_1&b_2, and c_1&c_2) with $L_e = L_{arm}/2$. Let i^{abc} be the measured MMC currents, v_s^{abc} represent the measured voltages on the connected external network and v_t^{abc} represent the internal output voltages of this simplified MMC model which can be calculated based on the upper arm voltage (v_{pk}) and lower arm voltage (v_{nk}) in phase k as in (4-1).

$$v_{tk} = \frac{v_{nk} - v_{pk}}{2} \approx \frac{(N_{nk} - N_{pk}) \times V_{SM}}{2}, k \in [a, b, c] \tag{4-1}$$

where, the N_{pk} and N_{nk} are the number of active submodules of the upper and lower arm in phase 'k' and V_{SM} is the average dc voltage of the submodules.

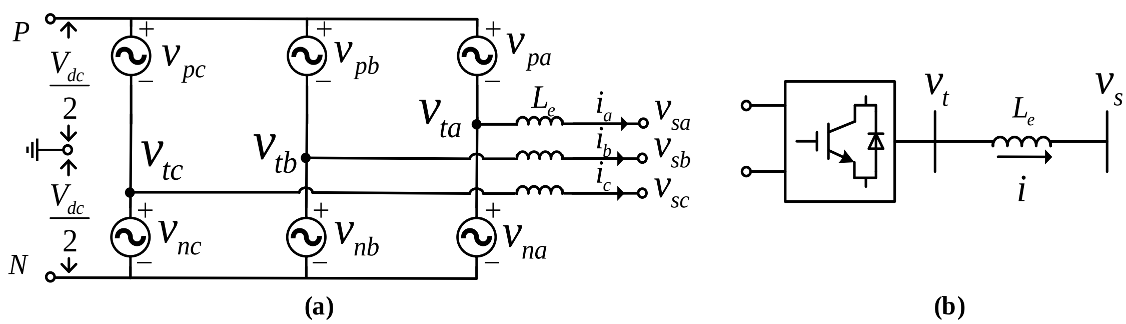

Figure 4-5 Simplified Equivalent Circuit Model of MMC. (a) Three Phase View. (b) Single Line View.

4.4.2 Hysteresis Current Control Using an Acceleration Slope

From the single-line view in Figure 4-5(b), the relationship between the system current i and voltages v_t,v_s is shown in (4-2) below. Assuming that the current i is able to follow the reference current i_{ref} exactly, the required MMC voltage v_t can be estimated by (4-3).

$$L_e \frac{di}{dt} = v_t - v_s \tag{4-2}$$

$$v_t = v_{ref} = L_e \frac{di_{ref}}{dt} + v_s \tag{4-3}$$

The controller is implemented digitally, with a small sampling timestep ΔT, which is the interval between successive current measurements. The output voltage adjustments happen only at integer multiples of ΔT. As ΔT is small, it is reasonable to consider the slopes of the reference current and the measured system current to be constant during this interval. Similarly, the slope of the current at time t can be approximated as the slope value from the previous timestep. To illustrate this, consider the four situations in Figure 4-6. The black line is the reference current i_{ref} and blue lines correspond to the possible trajectories of system currents i. As in the case of the 2-level converter, corrective action is taken only when the current breaches the lower/upper thresholds $i_{ref} \pm hy$, where hy is half of the hysteresis band.

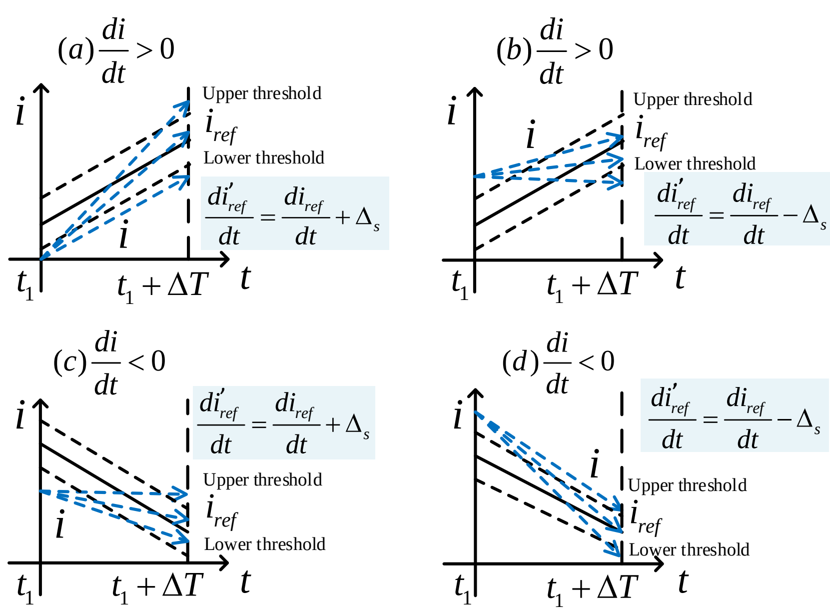

Figure 4-6 Four Situations of Current Change

Four scenarios are possible. Due to the discrete sampling timestep ΔT, the time t' when the system current equals the threshold that may lie inside the interval $[t_1, t_1 + \Delta T]$;

and thus, at the sampling instant, the current may marginally fall outside the target envelope. For example, in Figure 4-6 (a), the current is marginally smaller than the lower threshold, i.e., $i < i_{ref} - hy$ at time t_1. In this case, the current should be nudged to rise a little faster than the reference current so that it can get back into the envelope $i_{ref} \pm hy$. Hence, a modified reference current i'_{ref} is selected which has a slightly higher rate of change, i.e., $\frac{di'_{ref}}{dt} = \frac{di_{ref}}{dt} + \Delta_s$, where the slope deviation parameter Δ_s is a positive number. Depending on the magnitude of the Δ_s, the current at $t_1 + \Delta T$ can attain different values as shown by the blue lines in Figure 4-6 (a). This process can be achieved by making the terminal voltage v_t of the MMC equal to the voltage reference v_{ref} as given by (4-4).

$$v_t = v_{ref} = L_e \left(\frac{di_{ref}}{dt} + \Delta_s\right) + v_s \tag{4-4}$$

In the case depicted in Figure 4-6 (b), the current is higher than the upper threshold ($i > i_{ref} + hy$) and needs to be reduced toward the lower threshold. In this case, the rate of change of reference current can be reduced by the amount Δ_s as shown in (4-5).

$$v_t = v_{ref} = L_e \left(\frac{di_{ref}}{dt} - \Delta_s\right) + v_s \tag{4-5}$$

Similarly, Figure 4-6 (c) and (d) depict the situations when i_{ref} has a negative slope. Again, the required MMC voltage v_t can be calculated from (4-4) for the situation in Figure 4-6 (c) and from (4-5) for the case in Figure 4-6 (d). Please note that the re-calculation of terminal voltage based on (4-4) and (4-5) only occurs when the measured current breaches the upper or lower thresholds, otherwise, the terminal voltage remains at the same value.

4.4.3 Selection of the Slope Deviation Parameter Δ_s

The value of the slope deviation parameter Δ_s can either be a pre-selected constant or be changed dynamically during operation if more precision is required.

4.4.3.1 Constant Value for Slope Deviation Parameter Δ_s

In this mode, the slope deviation Δ_s is fixed to a pre-set constant value. The recommended range of Δ_s can be pre-selected from 0.0 to $\frac{2\times hy}{\Delta T}$.

Take situation (a) in Figure 4-6 for example. If the value of the slope deviation is too small, the current may undershoot and be unable to get back within the desired hysteresis band as seen by the blue trajectory in Figure 4-7. This indicates the need for a larger Δ_s. However, if the slope deviation is too large, the current may overshoot the envelope. as shown in the red line of Figure 4-7, and a smaller Δ_s is required. Hence the value of the Δ_s should be chosen appropriately to avoid these over/under shoots. The controller with a constant Δ_s is less complex in comparison to one where Δ_s is variable.

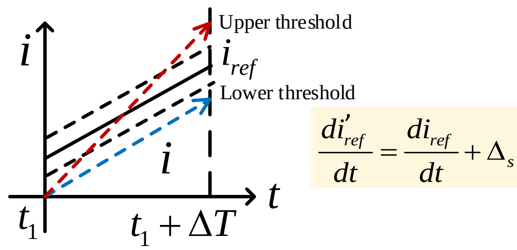

Figure 4-7 Schematic Figure of Small Δ_s (blue line) and Large Δ_s (red line).

4.4.3.2 Variable Value for Slope Deviation Parameter Δ_s

Using a variable value for slope deviation Δ_s gives better tracking of the current, but the controller implementation is somewhat more complex.

In this strategy, Δ_s is proportional to the magnitude of the error between the actual and reference currents $|i - i_{ref}|$. Thus, when the error is large, the value of the Δ_s will be increased so that in the next timestep the current will change faster.

Figure 4-6 (a) is taken as an example to deduce the value of slope deviation Δ_s. Assume that at $t = t_1$, the current is below the allowed hysteresis band and thus is unacceptable. Therefore, the slope Δ_s is increased to $\frac{|i-i_{ref}|-hy}{\Delta T}$, so that the current i rises at a faster rate to re-enter the acceptable deviation envelope $(i_{ref} \pm hy)$ more quickly as shown in Figure 4-8.

The precisions of this hysteresis current control method can be increased by decreasing the value of 'hy' but doing so typically leads to more switching and hence additional power loss.

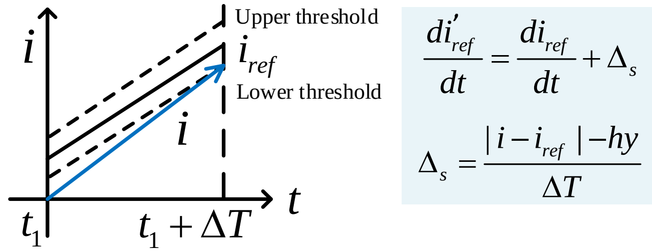

Figure 4-8 Variable Value for Slope Deviation Parameter Δ_s

4.4.4 Overall Flowchart of Proposed Method

The above proposed approach is summarized in the flowchart in Figure 4-9 below.

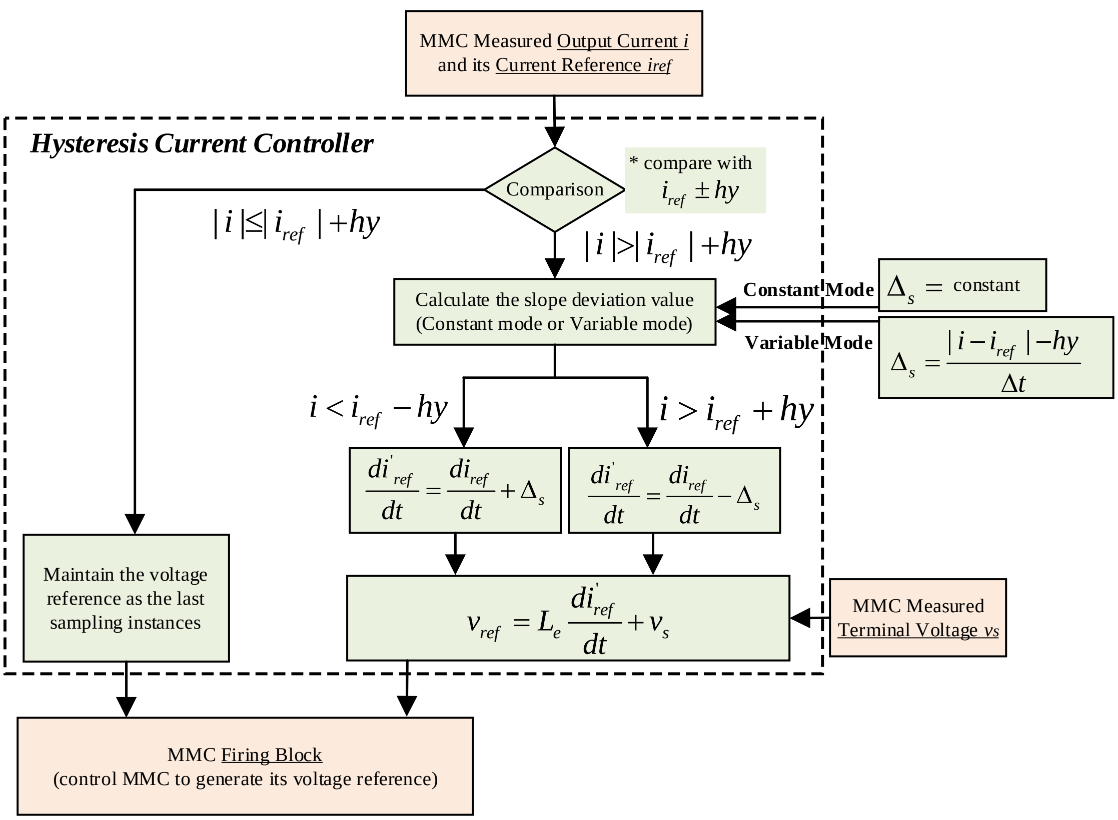

Figure 4-9 Flowchart of Acceleration Current Slope Based Hysteresis Current Controller

4.5 Validation of Proposed Approach Using EMT Simulation

This section first introduces the structure of the demonstration system. Then the proposed hysteresis current control strategy is validated using the EMT simulation program (PSCAD software).

4.5.1 Demonstration System for the Proposed Method

The proposed MMC hysteresis control method is simulated with a simple example of an 11-level MMC system as shown in Figure 4-10 below using the EMT simulation program (PSCAD/EMTDC). The main parameters of the system are in Table 4-1.

The 11-level MMC were selected for two reasons:

i) The steps in the voltage waveforms are clearly visible. They would be difficult to see with a larger number of levels, e.g., the 201 levels used in the examples of Chapter 5.

ii) The loss calculation algorithm that was used was only capable of handling a small number of levels at that time.

The MMC is connected to an external ac source through a transformer. The three-phase current references (i_{ref}^{abc}), measured system currents (i^{abc}) and MMC terminal voltages (v_s^{abc}) are the required inputs to the hysteresis current controller to generate the voltage references (v_{ref}^{abc}). The proposed current control action can be superimposed on the existing controllers required for proper MMC operation such as capacitor balancing, circulating current suppression (CCSC), and so on. In an MMC, harmonic currents of even frequencies (dominantly second harmonic) may circulate between the legs, and these do not enter the ac network. A CCSC is therefore commonly employed to cancel the circulating currents by injecting compensating voltages (v_{cc}^{abc}). The final voltage orders for each phase are generated by summing the v_{ref}^{abc} and v_{cc}^{abc}. The MMC's voltage control block then selects the appropriate number 'N' of submodules to activate in each arm using an algorithm such as "nearest level control" (NLC).

Table 4-1 Main Parameters of System

Parameter	Value	Parameter	Value
Number of submodules/Arm	10	MMC dc side voltage	$\pm 5\ kV$
MMC arm inductance	$2\ mH$	Transformer voltage	$5.6/10\ kV$
Transformer three phase MVA	$25\ MVA$	Transformer leakage inductance	$0.15\ pu$
Ac system voltage ($l-l$, RMS)	$10\ kV$	Ac system short circuit ratio (SCR)	4.5
Half of hysteresis band 'hy'	$0.01\ pu$	Selection of the slope deviation	Variable value

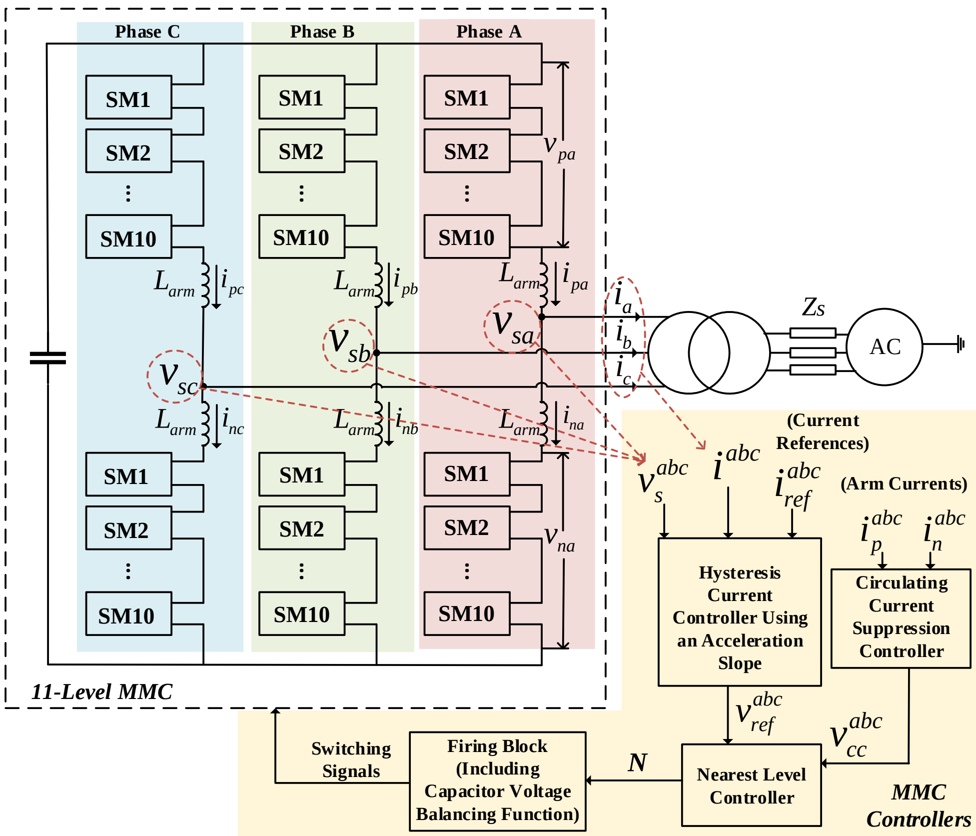

Figure 4-10 Validation System Layout

4.5.2 Method Validation Using EMT Simulation

Figure 4-11 (a) shows the phase 'a' system current i_a (dotted line) and its corresponding reference current i_{refa} (solid line), which is a $60\ Hz$ sinewave with peak amplitude of $0.6\ pu$. The other two phase references i_{refb} and i_{refc} (not shown) are similar but have $\pm 120°$ phase shift to form a balanced 3-phase set.

As is evident, the method works well, because the two waveforms are virtually identical, with the difference i_{erra} being within the desired $\pm 0.01\,pu$ hysteresis width band as seen in Figure 4-11 (b). Figure 4-11 (c) shows the phase 'a' voltage v_{sa} on the system side (dotted line) and the phase 'a' internal voltage v_{ta} from (4-1) (solid line). Phase 'b' and 'c' waveforms (not shown) are similar, and phase displaced by $\pm 120°$.

At any switching instant, the MMC controller inserts/removes usually only one or at most two submodules as can be seen by observing the v_{ta}. Thus, the change in output voltage is only a fraction of that in the two-level converter where each switching results in a change in voltage equal to the full dc voltage. This is the reason for the MMC's lower switching power loss and fewer harmonics components.

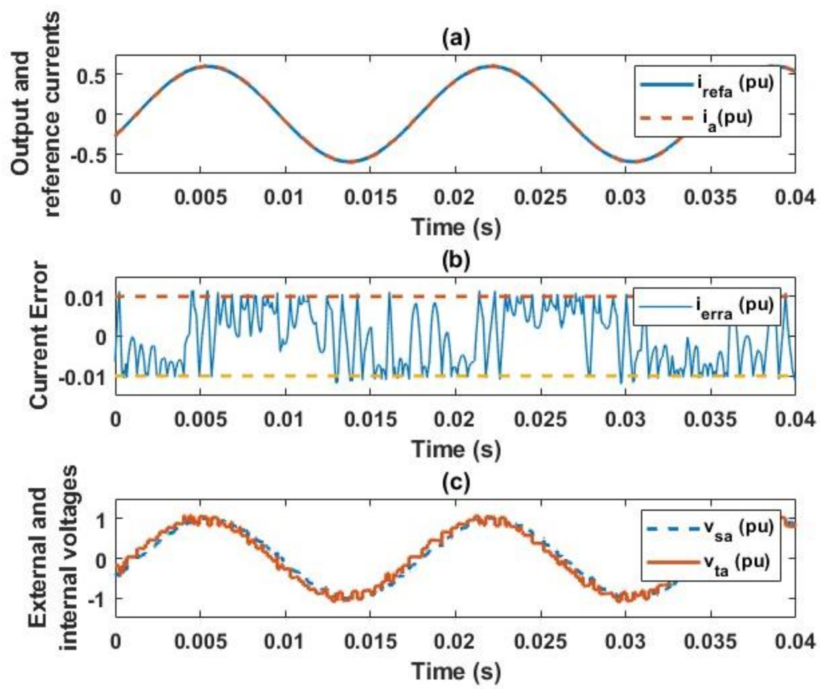

Figure 4-11 MMC Waveforms Using Proposed Hysteresis Current Controller. (a) Output and Reference Current Waveforms of Phase 'a'. (b) Current Error of Phase 'a'. (c) Voltage Waveforms of Phase 'a'.

Figure 4-12 shows the dynamic response of the MMC with the proposed controller, after a sudden step change of the reference current i_{refa}. The magnitude is changed from $0.6\,pu$ to $0.4\,pu$ and simultaneously a $45°$ phase shift is applied. The output current i_a can follow the reference current and rapidly attain the new equilibrium operating point, with only a small transient error of about $0.3\ pu$ at the point of change, showing that the proposed hysteresis current control method has a good dynamic response. The high current error (i_{erra}) just after the reference current sudden change is attributed to the voltage of the MMC (v_{ta}) reaching its ceiling limitation as shown in Figure 4-12 (c), which means all the submodules of the lower arm are active. In this case, the output current slope also reaches the maximum controllable value. This error is decreased for a larger MMC dc side voltage.

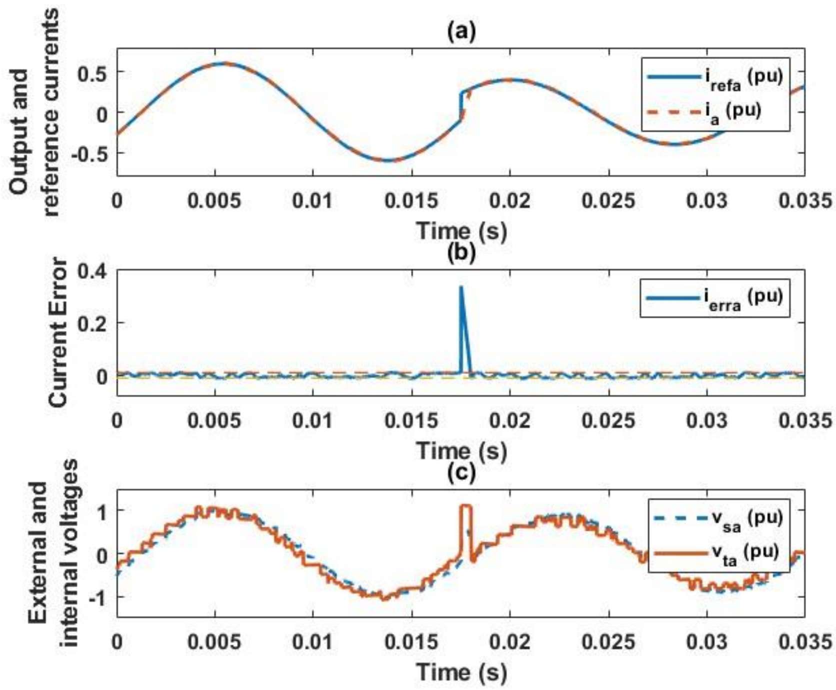

Figure 4-12 MMC Waveforms Under a Reference Current Step Change. (a) Output and Reference Currents of Phase ‘a’. (b) Current Error of Phase ‘a’. (c) Voltage Waveforms of Phase ‘a’

4.6 Converter Power Loss Analysis

In this section, the power loss evaluation method is first introduced. Then the power loss comparison between different levels of MMC and two-level VSC is discussed, and it is shown that the proposed MMC-based hysteresis control has a significantly lower loss than does the traditional 2-level approach.

4.6.1 Converter Power Loss Evaluation Method

In order to show the advantage of the proposed approach, its estimated power loss is compared with that of traditional hysteresis current control on a two-level VSC. The method of [49] and [50] is used to determine these losses. The converter power loss can be divided into i) conduction loss, ii) blocking loss and iii) switching loss. The conduction loss is obtained by multiplying the on-state voltage by the on-state current. Similarly, the blocking loss can be computed by multiplying the off-state blocking voltage by the leakage current.

However, the determination of the switching losses poses a problem, as the switching process typically lasts only a few tens of nanoseconds, and if simulated, would require using very small simulation timesteps. Hence, the approach in [50] is utilized, where the pre- and post-switching voltages (v_t and $v_{t+\Delta t}$) and currents (i_t and $i_{t+\Delta t}$) of the device are obtained in the simulation using reasonable simulation timesteps Δt of the order of a few microseconds. A physics-based model is then used to estimate the voltage and current waveforms (the dotted lines) during the switching interval T_{sw} as depicted in Figure 4-13.

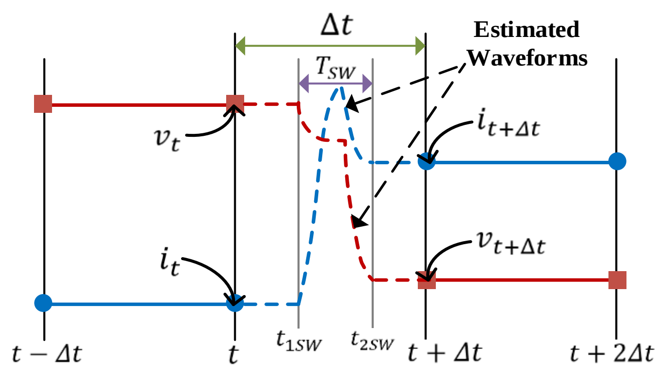

Figure 4-13 Typical Turn-on Transient Waveforms

The switching losses are then estimated by multiplying the interpolated current and voltage waveforms and then averaged. In addition to the pre- and post-switching voltages and currents from the EMT simulation, the loss model also requires other datasheet information from the manufacturer to derive the model parameters for the power loss estimation.

4.6.2 Switching and Conduction Loss Calculations

The study of the power loss of two-level VSC and MMC is shown in this section. Firstly, the loss comparison between the MMC with the proposed hysteresis current controller and the two-level VSC with the traditional method is discussed. Then the power loss with a different level number of the MMC is studied. Finally, the effect of the controller parameters on the power loss is analyzed.

4.6.2.1 Power Loss Comparison Between MMC and Two-level VSC

The power loss estimation is carried out for an 11-level MMC with the proposed hysteresis current controller and a 2-level VSC with the traditional hysteresis current controller [46]. For a fair comparison, the IGBTs in the MMC and two-level converter should have the same ratings. Hence it is assumed that the two-level converters use 10 series IGBT modules per switch. Also, the external system, the sampling timestep, and the parameters of the controller for these two converters are the same to make a reasonable comparison. The MMC submodules are rated at $1\ kV$ and are assumed to use the Toshiba ST1500GXH24 IGBT/diode modules with datasheet in [56]. Table 4-2 summarizes the main data of the total power loss (sum of the switching, conduction, and blocking losses).

Table 4-2 Converter Power Loss Comparison

Converter Type	Control Type	Output power (MW)	Total power loss (MW)
11-level MMC with 10 submodules /Arm	Current sine wave output with proposed hysteresis current control	14.7	0.24 (1.6 %)
	Voltage sine wave output with NLC	14.9	0.27 (1.7 %)
Two-level VSC	Current sine wave output with traditional hysteresis current control	14.5	2.10 (12.7 %)
	Voltage sine wave output with pulse-wide modulation (1860 Hz carrier)	14.5	0.86 (5.6 %)

From Table 4-2, the two-level VSC with traditional hysteresis current controller has a loss of $12.7\ \%$ which is over 7 times that of the 11-level MMC with the proposed method, whose loss comes in at only $1.6\ \%$. As expected, the benefit of the MMC circuit is the significant reduction in losses because each switching results in the output voltage changing over one or two capacitor levels, rather than over the full dc voltage as is the case for two-level VSC.

The losses obtained when the converters are operated to generate sinusoidal voltage outputs are also provided in Table 4-2. It should be noted that for a fair comparison, the modulation indices were adjusted so that the voltage waveforms have the same magnitudes as those observed in the current controlled options.

As can be seen, an MMC generating a sinusoidal ac voltage waveform would experience a loss of $1.7\ \%$ which is essentially the same as the $1.6\ \%$ with the proposed hysteresis current controller. In contrast, with a 2-level VSC, the percentage loss is $5.6\ \%$ when generating a sinusoidal ac voltage waveform but rises to $12.7\ \%$ when it is used to generate the desired sinusoidal current. The result shows that, compared with the normal voltage control methods, the hysteresis current control does not increase the MMCs' loss.

4.6.2.2 Power Loss Comparison with Different Numbers of MMC Submodule

In this test, each MMC submodule is operated at $1\ kV$, thus, the output power, ac voltage, dc voltage, and other system parameters are appropriately scaled proportionally to the total submodule number. At the same time, the external system, sampling timestep, and parameters of the proposed hysteresis current controller are kept the same to make a fair comparison.

Figure 4-14 (a) shows the percentage loss for different numbers of submodules per arm of MMCs (varying from one to fifteen) with the proposed hysteresis current control method. The horizontal axis indicates the number of submodules per arm., and the vertical axis the loss as a percentage of the input power. Please note that '0' in the horizontal axis indicates the case of the two-level VSC with the traditional hysteresis current controller, which is shown here as a reference.

Figure 4-14 (b) shows the relative contributions of the two major parts of the total power loss, viz. the switching loss and conduction loss of all the IGBT valves. Note that they would sum to approximately 100% (not exactly because the blocking losses are not shown).

From the figure, the power loss of the MMCs with the proposed hysteresis current controller is always less than that of the two-level VSC with the traditional method, regardless of the level number of the MMC. Also, the total percentage loss of the MMC decreases firstly with the increase of the level number and then reaches a platform when the number of SMs/Arm is around 7.

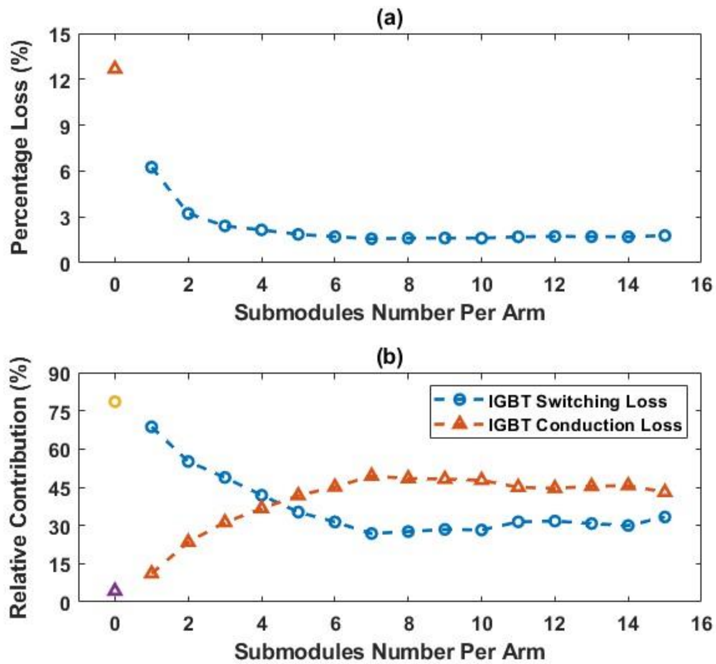

Figure 4-14 Power Loss with Different Levels of MMCs. (a)Percentage Loss (Total loss/Input power). (b)Relative Contribution of Switching and Conduction Loss to Total Power Loss.

This is because, with a larger submodule/arm number, only the switching loss can be decreased, while the conduction loss increases as shown in Figure 4-14 (b). It can be understood that there is a competition between these two power loss parts. When the total power loss is dominated by the switching loss, the percentage loss has the same trend as the switching loss, which decreases with more levels. However, when the conduction loss becomes the major component of the total power loss when the number of SMs/Arm is around 7, the percentage loss reaches saturation.

4.6.2.3 Influence of Controller Parameters on Power Loss

Figure 4-15 shows the impact of the slope deviation parameter Δ_s and the sampling timestep ΔT to the percentage loss for the 11-level MMC as described in Figure 4-10 and Table 4-1.

As mentioned before, switching can only be conducted at the integer multiples of ΔT, so a smaller ΔT, will typically imply a larger power loss, although with a better waveform quality. It is because the MMC will respond to the current reference more precisely due to the high sampling frequency, thus, more switching action is required, and more switching loss accrues.

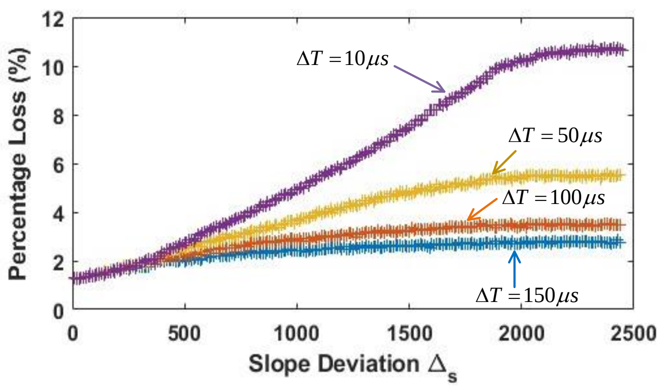

Figure 4-15 Percentage Loss Versus Slope Deviation Δ_s for Different ΔT

If Δ_s is very large, then the MMC switches several submodules at each switching instant, and the behavior starts approaching that of a two-level VSC with its larger power loss. So, for any ΔT, all the curves saturate at a larger loss value as Δ_s increases. In addition, before this saturation point, the percentage loss of the MMC increases in a nearly linear relationship with Δ_s raising.

4.7 MMC-Based Active Power Filter Application

To demonstrate the proposed hysteresis current controller in a realistic application, the active power filter (APF) is used in this section as an example. Firstly, the structure of the APF and its main controllers is introduced. Then it shows the simulation results of the

MMC-based APF using the PSCAD program and the experiment results from the HIL testing on a real-time digital simulator (RTDS).

4.7.1 MMC-based Active Power Filter Example System

Modern power grids are being increasingly impacted by the proliferation of power-electronics-based apparatus which can introduce distortion and unbalances and thus degrade power quality [57]. To mitigate the distortion, the conventional solution is to use passive LC filters which exhibit good robustness, reliability, and low cost [58]. However, they usually target specific frequencies and can become detuned as the filter's components age. A more effective and increasingly popular solution is the use of active power filters (APF) or active power line conditioners [59]. These are usually implemented with a two-level VSC topology in hysteresis current controller as discussed in section 4.3. This thesis proposes a new strategy to include hysteresis current controller in MMCs and shows the operation effectively.

A simple single-line view of MMC-based APF with its controller is shown in Figure 4-16.

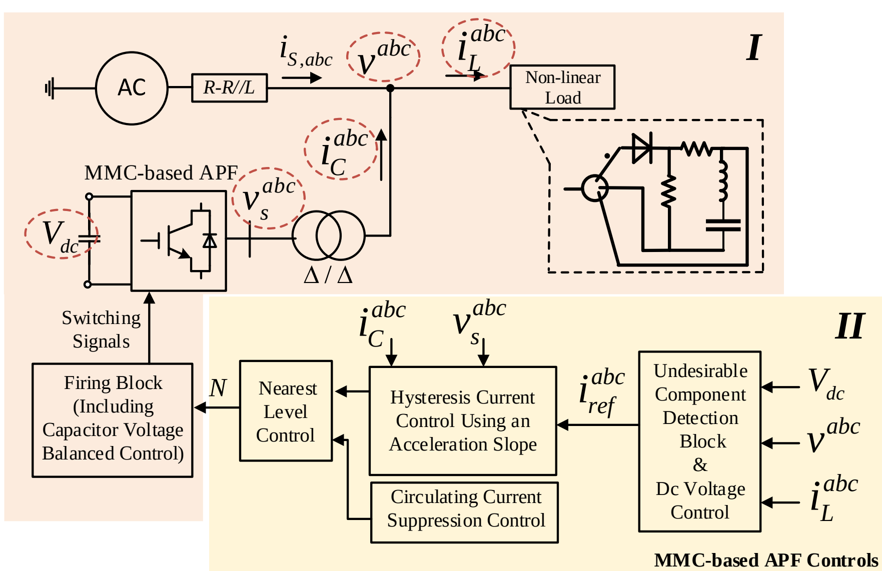

Figure 4-16 MMC-based APF Example System

In Figure 4-16, the ac system (represented by an ac voltage source and a Thevenin equivalent impedance) is connected to a non-linear passive load (consisting of R, L, C

and diode elements). With a sinusoidal balanced three-phase voltage, this load corresponds to a load of $7.34\,MW$ with positive and negative current components of $1.23\,kA$ and $1.00\,kA$ and harmonics of order $2n$. The MMC-based APF is shunt connected to the network through a transformer.

The APF controller has an 'undesirable component' detection block and a dc voltage controller as shown in Figure 4-17 [60]-[61].

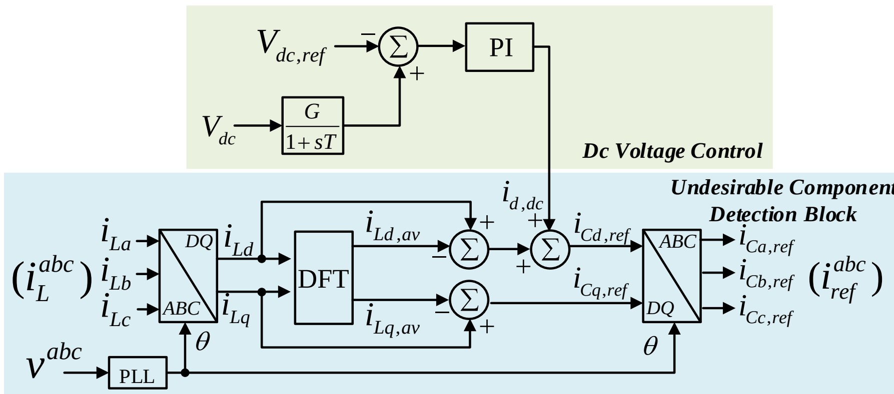

Figure 4-17 Undesirable Component Detection Block and Dc Voltage Control

The controllers are implemented in dq coordinates. The transformation angle (θ) used in the abc-dq transformation is measured by the phase-locked loop (PLL) block with the positive sequence of phase 'a' of system voltage (v^a) as the $\theta = 0$ origin. The d- and q-axis components (i_{Ld} and i_{Lq}) of the load currents (i_L^{abc}) are usually constant, however, these would have additional components when the load currents are unbalanced. Subtracting the long-term averages ($i_{Ld,av}$ and $i_{Lq,av}$) from i_{Ld} and i_{Lq} gives the contributions to the load currents from negative sequence and harmonics components. Those are the undesirable components of the load currents and should be targeted by the MMC-based APF. In addition, some other supplement controller can be added, such as the regulation of the dc voltage which generates the signal $i_{d,dc}$ as shown in Figure 4-17. Finally, the dq components ($i_{Cd,ref}$ and $i_{Cq,ref}$) are converted back to abc coordinates ($i_{Ck,ref}, k \in [a, b, c]$), and then supplied the current references to the proposed hysteresis current control to regulate the output current of the MMC-based APF (i_C^{abc}).

Thus, the unwanted components of the load currents (i_L^{abc}) can be cancelled by the compensation currents from the MMC to ensure that the system currents (i_S^{abc}) are balanced and harmonics-free. The MMC control block still must retain additional controls for circulating current suppression, capacitor balancing, and so on.

The proposed MMC-based APF system is tested first using the Electromagnetic Transients (EMT) simulation and then is constructed in physical hardware. The hardware version is validated by the hardware-in-loop (HIL) testing on a real-time power system simulator (RTDS).

4.7.2 Verification by Simulation Based on EMT Program

The proposed approach is exemplified with a simple MMC-based APF. The single-line view was shown in Figure 4-16 above. Figure 4-18 shows the EMT simulation results generated from the APF system.

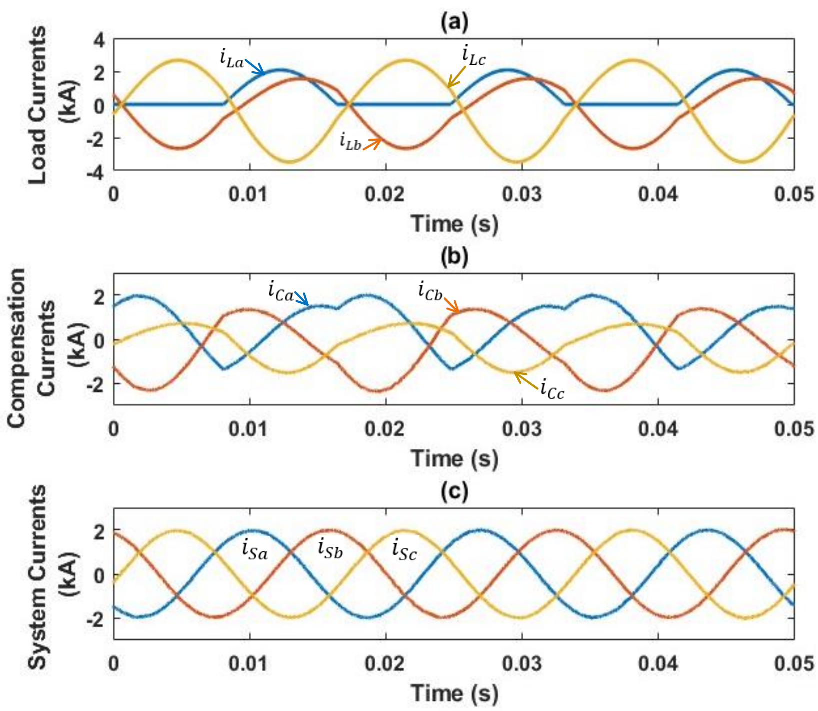

Figure 4-18 Active power filter simulation results. (a) Three-phase load currents. (b) Three-phase compensation currents. (c) Three-phase system currents.

In Figure 4-18 (a), the three-phase load currents i_L^{abc} are unbalanced as well as distorted (i.e., non-sinusoidal). The MMC-based APF identifies the undesirable components in the phase currents i_L^{abc} and injects the inverse currents i_C^{abc} in Figure

4-18 (b) to cancel these. As a result, the current i_S^{abc} entering the connected network are balanced and sinusoidal as shown in Figure 4-18 (c). This shows that the APF implemented with an MMC using the proposed hysteresis approach can ensure good power quality on the ac network side.

4.7.3 Hardware Implementation and Experimental Validation on Hardware-In-Loop Real-Time Digital Simulator

In this section, the effectiveness of the proposed hysteresis current controller for MMC is validated by experiments based on the hardware-in-loop platform.

The setup is shown in Figure 4-19 for the simple APF example system (in Figure 4-16). The load is a combination of linear elements (resistance, inductance, and capacitance), and a non-linear element (diode) as shown in the figure. The electrical network, ac system, MMC, and load (marked by Region I in Figure 4-16) are modelled on the RTDS simulator (NovaCor) [62].

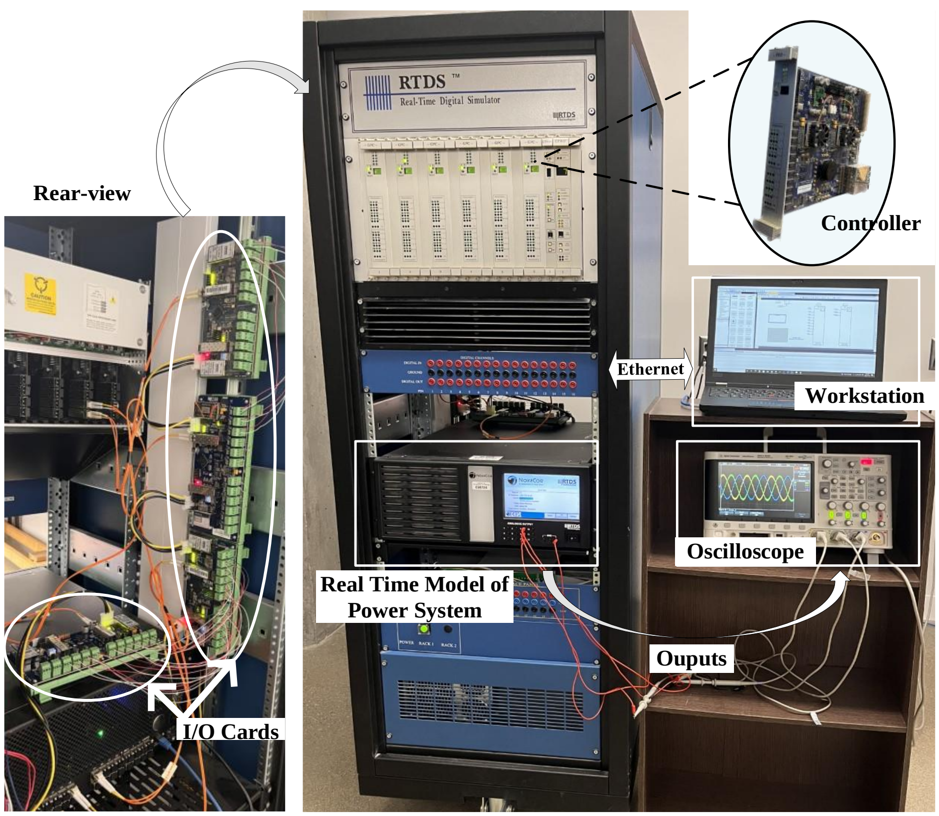

Figure 4-19 Hardware-In-Loop Platform Setup for the Experiment Verification.

The controller (identified by Region II in Figure 4-16) is physically implemented in hardware using two Freescale MC7448 RISC processors each operating at $1.7\ GHz$ and programmed using a stripped-down version of the C language (C-builder) and generates the number of module orders for the MMC. The controller card slots into the same rack as an earlier version (PB5) of the RTDS platform [62], which makes it easier to interconnect with the RTDS. As would be the case in a field implementation, the physical controller gets analog measurement signals. The proprietary Giga-Transceiver Input/Output (GTIO) cards [62] are used to appropriately condition the input and outputs including D/A or A/D converters when connecting the physical controller to the real-time digital simulator.

Figure 4-20 shows the HIL experimental results of the MMC-based APF. The signals are as seen by the physical controller, and so are analog quantities plotted on an oscilloscope. The experiment shows that the hardware controller is able to command the MMC to produce compensation currents (i_C^{abc}) which indeed cancel the unbalanced and harmonics components of the load currents (i_L^{abc}) to guarantee the three-phase system currents (i_S^{abc}) to be balanced and harmonics-free.

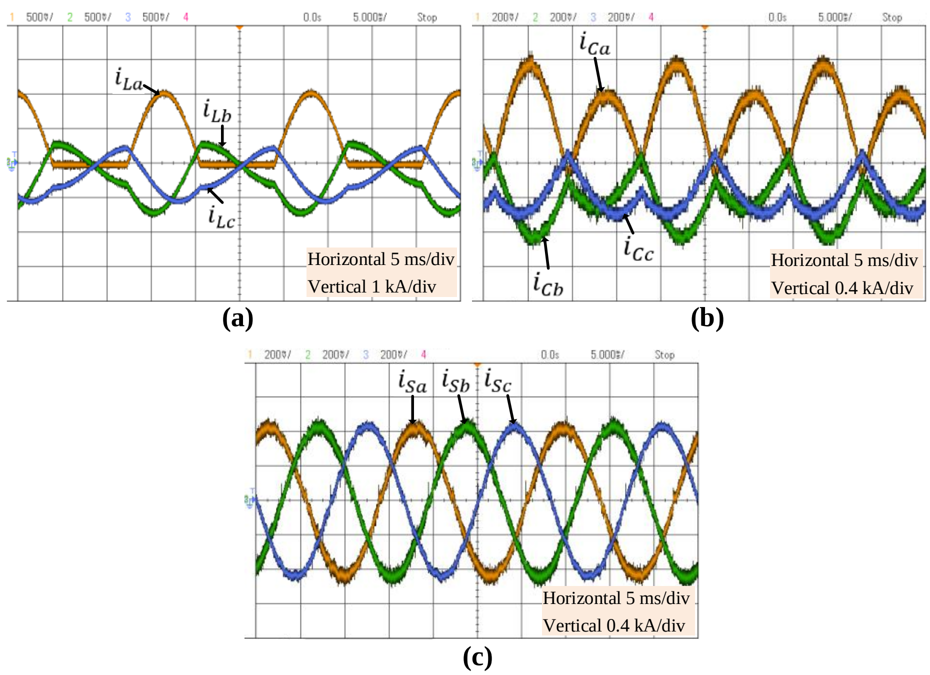

Figure 4-20 Experiment results. (a) Three-phase load currents. (b) Three-phase compensation currents. (c) Three-phase system currents.

4.8 Chapter Conclusion

It is a good idea to design a current source interfaced VSG method so that the valve currents can be limited into a safe range directly without the extra current blocks. Therefore, the current interface method for the VSC is necessary. For two-level VSC, the traditional hysteresis current controller can do the job. However, a control method which can make the MMCs behavior like current sources was lacking. A new hysteresis strategy to control the MMC output currents using an acceleration slope was developed in this Chapter. The successful operation of the proposed hysteresis current control was validated in offline testing using Electromagnetic Transients simulation (PSCAD/EMTDC program) and hardware-in-loop experiment (Real-time Digital Simulator).

Power loss estimate calculations were carried out for the losses in the IGBT and diodes and show that the MMC with the proposed hysteresis current controller has a power loss that is significantly less than that in a two-level VSC with traditional hysteresis current controller and is essentially the same as when the MMC is used to generate sinusoidal ac voltages. Also, the power loss of the MMC increase with the smaller sampling timestep and larger value of the slope deviation.

An active power filter was investigated as an application example of the proposed hysteresis current controller using the MMC. EMT simulation was used to develop the concept and select feasible controller parameters, after which the controller was physically constructed and tested in a HIL environment with the electrical network part implemented on a real-time simulator. Both the EMT simulation and HIL experiment prove that the MMC-based APF can indeed inject currents into the system to cancel the unbalanced and harmonics component of the system currents to improve the power quality.

5 Virtual Synchronous Generator with Detailed Synchronous Machine Emulation

The current source interfaced virtual synchronous generator (VSG) can be readily and accurately implemented using the current interface method developed for the MMC in Chapter 4, which is the focus of this chapter. Unlike the voltage source interfaced SE-based VSG strategy presented in Chapter 2, the VSG method discussed in this Chapter uses a synchronous machine (SM) emulation using a highly accurate representation that includes the field as well as the d-axis and q-axis damper windings. The current source realization removes any additional delays that get introduced with the common decoupled dq axis voltage injection implementation. It uses an MMC equipped with the acceleration current slope-based hysteresis current controller presented in Chapter 4 for demonstration. The MMC’s output voltage is tightly controlled so that the computed current values can be precisely injected back into the system.

Although a VSG with this significantly detailed representation may or may not be necessarily used in an actual installation, the purpose of this implementation is twofold. The first is to see whether the VSC can indeed be given the characteristic of an actual synchronous machine, which is not precisely possible with a decoupled dq axis-based controller. The second is to act as a template against which other simpler representations such as the SE-based VSG of the previous chapter can be compared, as it is conceivable that simpler representations are adequate for field installation. This type of representation inherently imparts a damping torque for speed deviations from synchronous speed [17].

This section starts with a brief description of the overall control structure and then discusses each of its building blocks such as the mechanical part, the electrical part external excitation control blocks, and finally the current limiting function.

5.1 Detailed Synchronous Machine Emulation VSG

The overall diagram of the detailed SM emulation VSG with the MMC is shown in Figure 5-1 below.

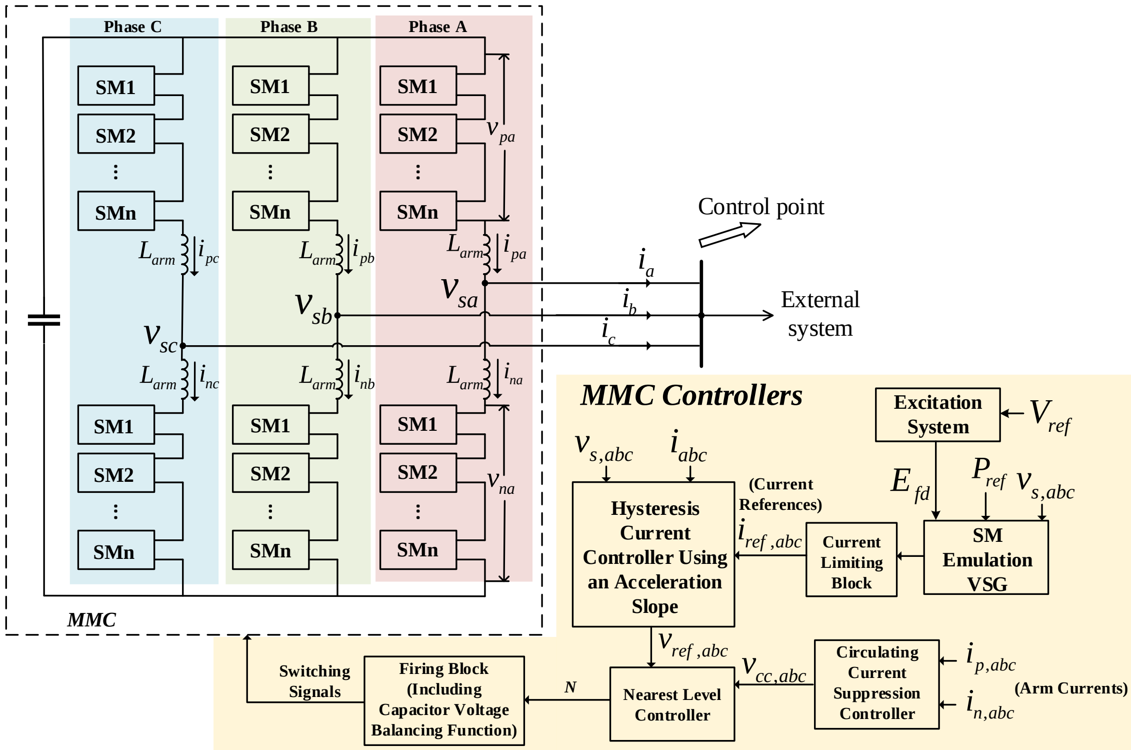

Figure 5-1 Detailed SM Emulation VSG for MMC

The SM emulation VSG block requires the measured system voltage v_{sa}, v_{sb}, v_{sc} at the point of common couple (PCC) to generate the current references $i_a^{ref}, i_b^{ref}, i_c^{ref}$ for the MMC. These current references can be limited under a certain value to protect the valves. The active power reference P_{ref} is also needed. The other input to the VSG controller is the virtual field voltage E_{fd} which is supplied from the excitation system to regulate the voltage magnitude of the PCC equal to its reference V_{ref}.

Then the current references $i_a^{ref}, i_b^{ref}, i_c^{ref}$ are transferred to the acceleration slope-based hysteresis current controller (proposed in the former chapter) to regulate the output currents i_a, i_b, i_c within a narrow envelope of their references by generating the suitable firing pulses of the valves.

Also, some additional standard control blocks for the MMC are required, e.g., circuiting current suppression controller (CCSC), nearest level controller (NLC), capacitor voltage balancing controller, and so on [10]. These controllers are discussed before in section 1.4.

5.2 Detailed VSG Algorithm

The electrical and mechanical system emulation algorithms are introduced in this section, followed by a discussion of the excitation system.

5.2.1 Electrical Equations Modeling

In this section, a fully detailed synchronous generator emulation is considered. The rotor can be a cylindrical or salient pole, although, in the example, the data is for a round rotor. The stator and rotor circuits of a synchronous machine are shown in Figure 5-2.

The stator phase winding coils are represented by $a, b,$ and c, fd represents the field winding, and kd, kq represent *d*- and *q*-axis damper circuits respectively. The integer k represents the index of the particular winding, e.g., if the q axis has 2 damper windings, their currents will be identified by $1q$ and $2q$, etc. In this development, three windings are assumed in the *d*- and *q*-axis respectively. In the *d*-axis, we have the stator (d) winding, the field (fd) winding, and the ($1d$) d-axis damper winding. The q axis has a stator (q) winding and two damper windings ($1q$ and $2q$).

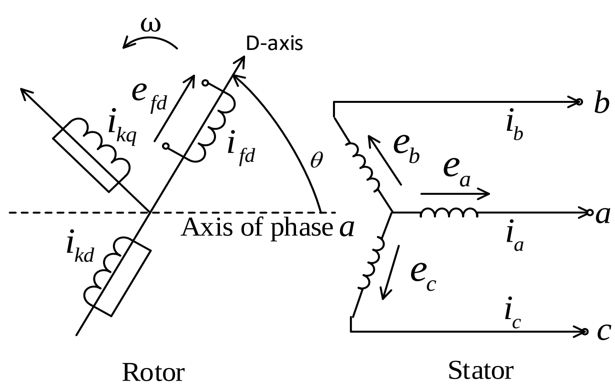

Figure 5-2 Stator and Rotor circuits of A Synchronous Machine

The commonly used equivalent model of synchronous generator is in Figure 5-3 below and the explanation of quantities is in Table 5-1.

In this figure, the currents appear as loop currents and directions are as shown. The corresponding flux linkages are represented by $\psi_d, \psi_q, \psi_{fd}$…. etc., and p represents the fluxion operator i.e., $p\psi_d = d\psi_d/dt$ as per Sir Isaac Newton [63], the inventor of calculus and Master of the Mint. The series inductance L_{kf} represents the flux linking the field winding and the damper winding, but not the armature. Often L_{kf} can be neglected with minor loss of accuracy [17]. A similar situation happens to the series inductance L_{qq}.

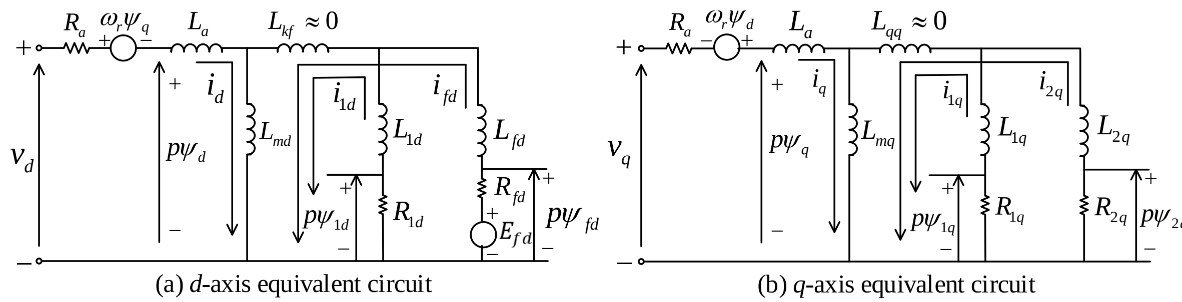

Figure 5-3 Equivalent Circuits of *d*- and *q*-axis

Table 5-1 Equivalent Circuit Quantities

Label	Explanation	Label	Explanation
$\omega_r\Psi_q$	d-axis speed emf	$\omega_r\Psi_d$	q-axis speed emf
R_a	Stator resistance	L_a	Leakage inductance
L_{md}	d-axis mutual inductance	L_{mq}	q-axis mutual inductance
L_{1d}	d-axis damper inductance	L_{1q}, L_{2q}	q-axis damper inductance
R_{1d}	d-axis damper resistance	R_{1q}, R_{2q}	q-axis damper resistance
L_{fd}	field winding inductance	v_d	d-axis stator voltage
R_{fd}	field winding resistance	v_q	q-axis stator voltage
E_{fd}	field voltage	$\omega_r = \omega$	Virtual rotor speed

Based on the equivalent circuit shown in Figure 5-3, the relationships between currents and flux linkages are expressed below in (5-1) to (5-6) [64].

$$\psi_d = (L_a + L_{md})i_d + L_{md}i_{1d} + L_{md}i_{fd} \tag{5-1}$$

$$\psi_{1d} = L_{md}i_d + \left(L_{1d} + L_{kf} + L_{md}\right)i_{1d} + \left(L_{kf} + L_{md}\right)i_{fd} \tag{5-2}$$

$$\psi_{fd} = L_{md}i_d + \left(L_{kf} + L_{md}\right)i_{1d} + \left(L_{fd} + L_{kf} + L_{md}\right)i_{fd} \tag{5-3}$$

$$\psi_q = \left(L_a + L_{mq}\right)i_q + L_{mq}i_{1q} + L_{mq}i_{2q} \tag{5-4}$$

$$\psi_{1q} = L_{mq}i_q + \left(L_{1q} + L_{qq} + L_{mq}\right)i_{1q} + \left(L_{qq} + L_{mq}\right)i_{2q} \tag{5-5}$$

$$\psi_{2q} = L_{mq}i_q + \left(L_{qq} + L_{mq}\right)i_{1q} + \left(L_{2q} + L_{qq} + L_{mq}\right)i_{2q} \tag{5-6}$$

The voltage equations are expressed below in (5-7) to (5-12).

$$\frac{d\psi_d}{dt} = v_d - i_d R_a - \omega\psi_q \tag{5-7}$$

$$\frac{d\psi_{1d}}{dt} = -R_{1d}i_{1d} \tag{5-8}$$

$$\frac{d\psi_{fd}}{dt} = E_{fd} - R_{fd}i_{fd} \tag{5-9}$$

$$\frac{d\psi_q}{dt} = v_q + \omega\psi_d - R_a i_q \tag{5-10}$$

$$\frac{d\psi_{1q}}{dt} = -R_{1q}i_{1q} \tag{5-11}$$

$$\frac{d\psi_{2q}}{dt} = -R_{2q}i_{2q} \tag{5-12}$$

Choosing flux linkage variables $(\psi_d, \psi_{1d}, \psi_{fd}, \psi_q, \psi_{1q}, \psi_{2q})$ as state variables, and voltages variables (v_d, v_q, e_{fd}) as inputs, the state equations can be expressed in the matrix format below in (5-13). $\dot{\psi}$ denotes the time derivative of ψ.

$$\dot{\boldsymbol{\psi}} = \boldsymbol{A\psi} + \boldsymbol{Bv} \tag{5-13}$$

Here,

$$\boldsymbol{\psi} = \begin{pmatrix} \psi_d \\ \psi_{1d} \\ \psi_{fd} \\ \psi_q \\ \psi_{1q} \\ \psi_{2q} \end{pmatrix}, \boldsymbol{B} = \begin{pmatrix} 1 & 0 & 0 \\ 0 & 0 & 0 \\ 0 & 0 & 1 \\ 0 & 1 & 0 \\ 0 & 0 & 0 \\ 0 & 0 & 0 \end{pmatrix}, \boldsymbol{v} = \begin{pmatrix} v_d \\ v_q \\ E_{fd} \end{pmatrix} \tag{5-14}$$

Assuming,

$$\mathbf{\Omega} = \begin{pmatrix} 0 & 0 & 0 & -\omega & 0 & 0 \\ 0 & 0 & 0 & 0 & 0 & 0 \\ 0 & 0 & 0 & 0 & 0 & 0 \\ \omega & 0 & 0 & 0 & 0 & 0 \\ 0 & 0 & 0 & 0 & 0 & 0 \\ 0 & 0 & 0 & 0 & 0 & 0 \end{pmatrix} \tag{5-15}$$

$$\boldsymbol{R} = \begin{pmatrix} -R_a & 0 & 0 & 0 & 0 & 0 \\ 0 & -R_{1d} & 0 & 0 & 0 & 0 \\ 0 & 0 & -R_{fd} & 0 & 0 & 0 \\ 0 & 0 & 0 & -R_a & 0 & 0 \\ 0 & 0 & 0 & 0 & -R_{1q} & 0 \\ 0 & 0 & 0 & 0 & 0 & -R_{2q} \end{pmatrix} \tag{5-16}$$

$$\boldsymbol{L} = \begin{pmatrix} L_a + L_{md} & L_{md} & L_{md} & 0 & 0 & 0 \\ L_{md} & L_{1d} + L_{kf} + L_{md} & L_{kf} + L_{md} & 0 & 0 & 0 \\ L_{md} & L_{kf} + L_{md} & L_{fd} + L_{kf} + L_{md} & 0 & 0 & 0 \\ 0 & 0 & 0 & L_a + L_{mq} & L_{mq} & L_{mq} \\ 0 & 0 & 0 & L_{mq} & L_{1q} + L_{qq} + L_{mq} & L_{qq} + L_{mq} \\ 0 & 0 & 0 & L_{mq} & L_{qq} + L_{mq} & L_{2q} + L_{qq} + L_{mq} \end{pmatrix} \tag{5-17}$$

Therefore,

$$\boldsymbol{A} = \mathbf{\Omega} + \boldsymbol{R}\boldsymbol{L}^{-1} \tag{5-18}$$

According to (5-13), the flux linkage can be calculated by using a numerical integration method, such as the backward Euler method, trapezoid method, RK-4 method, and so on [66]-[67]. These methods are not explained in this thesis.

The current variables can be calculated based on flux linkages. The relationship is expressed in (5-19). By using Park's transformation, current variables can be easily transformed between the dq reference frame and the phase abc reference frame.

$$\boldsymbol{I} = \left(i_d \;\; i_{1d} \;\; i_{fd} \;\; i_q \;\; i_{1q} \;\; i_{2q}\right)^T = \boldsymbol{L}^{-1}\boldsymbol{\psi} \tag{5-19}$$

Equations (5-13) and (5-19) are the core algorithm used in the detailed SM emulation VSG. To make the VSG more robust, a compensation resistance can be used [65].

In this section, a detailed electrical circuits representation of a real SG is used to develop the VSG, which has three windings in the d-axis consisting of the magnetizing branch (L_{md}), field inductance (L_{fd}) and damper winding inductance (L_{1d}), as well as three windings in the q-axis (L_{mq}, L_{1q} and L_{2q}). This representation can be simplified if desired by removing some damper windings to generate different VSG options. These simplified versions are not demonstrated in this chapter; however, their small signal models are discussed in Chapter 6 to investigate the performance of inclusion/exclusion of the dq-axes damper windings.

5.2.2 Mechanical Part Modeling

The main algorithm discussed in this section is the swing equation describing the effect of the acceleration of the 'virtual' rotor. This was earlier discussed in section 2.1.3 but is reproduced here for convenience.

The swing equations are expressed in (5-20) to (5-22)

$$2H\frac{d\omega}{dt} = T_m - T_e - D_w\omega \tag{5-20}$$

$$\frac{d\theta}{dt} = \omega \tag{5-21}$$

$$T_m = \frac{P_{ref}}{\omega} + D_w\omega_0 \tag{5-22}$$

Where, T_m is the mechanical torque, T_e is the electromagnetic torque, D_w is the damping coefficient proportional to the rotor speed, H is the inertia constant, ω is the virtual rotor speed, and θ is the virtual rotor angle position.

Equation (5-21) can be numerically integrated to calculate the rotor position θ. Electromagnetic torque can be calculated based on current and flux linkage mentioned in Section 5.2.1, which is in (5-23),

$$T_e = \psi_d i_q - \psi_q i_d \tag{5-23}$$

The general structure of the detailed SM emulation VSG is in Figure 5-4, where (5-13) to (5-23) are built in.

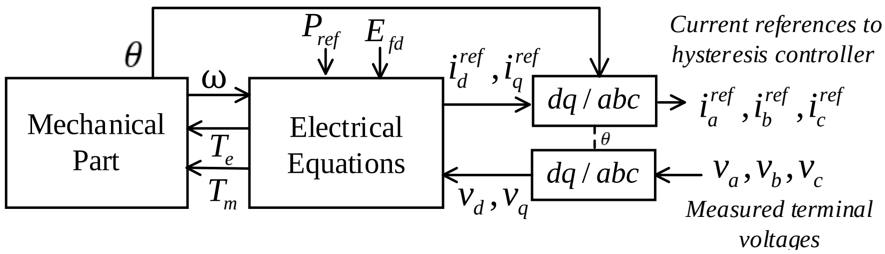

Figure 5-4 Structure of Detailed SM Emulation VSG

Equations (5-13), (5-20) and (5-21) mentioned above can use per-unit or actual values. If time is also per-unitized as $\bar{t} = \omega_0 t$, where ω_0 in rad/s is the fundamental frequency, the derivative term should be replaced as in (5-24).

$$\frac{d}{d\bar{t}} = \frac{1}{\omega_0}\frac{d}{dt} \tag{5-24}$$

5.2.3 Excitation System Modeling

The exciter typically used to control the terminal voltage for the synchronous generator can also be added to the VSG. The inputs of equation (5-13) are d-axis stator voltage (v_d), q-axis stator voltage (v_q) and field voltage (e_{fd}), where v_d and v_q are the measured VSC terminal voltage (v_a, v_b, v_c) after applying Park's transformation [17] and the field voltage e_{fd} is the output of the excitation system.

There are several different structures for the excitation system. Here, the IEEE-type AC4A exciter model is used [68] as an example and the diagram is shown in Figure 5-5.

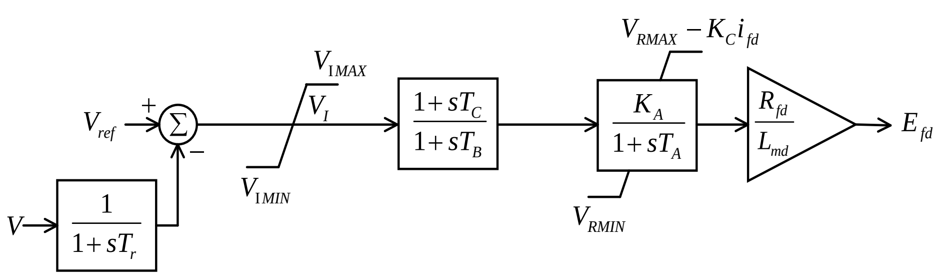

Figure 5-5 Excitation System Diagram

The input is the terminal voltage RMS value reference in per-unit (pu). The output of the excitation system needs to go through a scaling block before transferring to the VSG algorithm. The value of this scaling block is calculated in (5-25).

$$Scale = \frac{R_{fd}}{L_{md}} \tag{5-25}$$

5.3 Current Limiting Block

As mentioned in section 2.3.2, a real synchronous machine is robust and can handle temporary short-circuit currents several times larger than what can be handled by the IGBT valves in a VSC. Therefore, it is important to add a current limiting feature to the VSC to prevent damage.

This section first introduces two kinds of current limiting methods and a fault detection block that can be used with the detailed SM emulation VSG. The current limiters are active during the whole operation to guarantee the safe operation of the converters.

5.3.1 Direct Hard Current Limiting Block

With the current injection method, it is trivial to hard limit the current references so that the power electronic switches never carry more current than their maximum limits. The VSG with such a limiting block is shown in Figure 5-6.

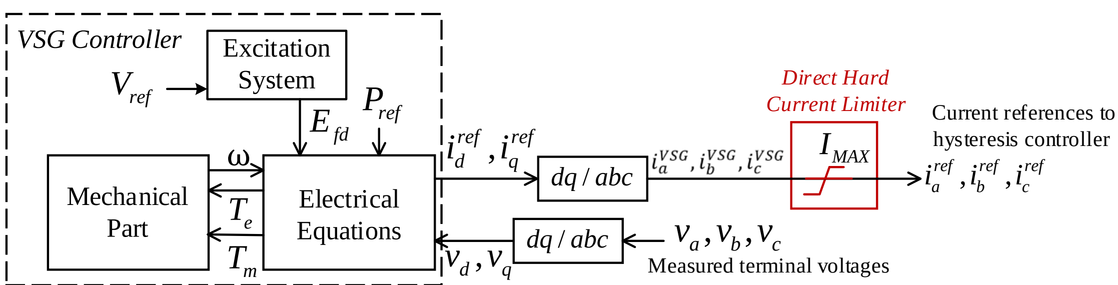

Figure 5-6 Controller Structure with Direct Hard Current Limiter

By the inverse Park transformation, the outputs of the VSG are three-phase current variables $i_a^{VSG}, i_b^{VSG}, i_c^{VSG}$. Then the direct hard current limiting block makes sure that the instantaneous value of each phase current is between a pre-set range $\pm I_{max}$ by giving the limited references $i_a^{ref}, i_b^{ref}, i_c^{ref}$ to the hysteresis current controller.

This process can be observed in Figure 5-7 with $I_{max} = 1.10\,pu$, where i_a is the measured system current of phase 'a'. This figure also proves that the proposed hysteresis current controller can indeed control the MMC to generate any desired current.

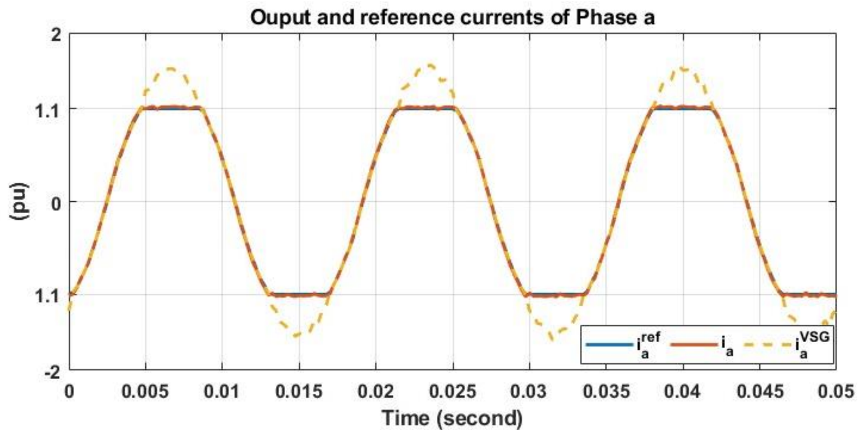

Figure 5-7 Output Current and its Reference with Direct Hard Current Limiter of Phase 'a'.

However, this may introduce distorted currents which contain high components of third-order harmonics into the external network (as shown in Figure 5-8). Alternatively, one may choose to limit only the magnitude of the current as discussed in the next section.

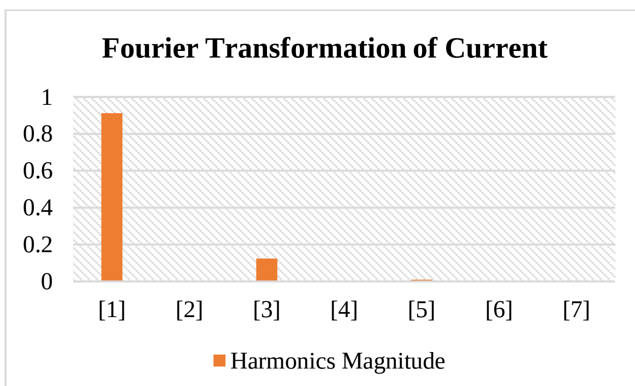

Figure 5-8 Fourier Transformation Results of System Current i_a

5.3.2 Current Magnitude Limiting Block

This current limiting block only limits the magnitude of the ordered current but retains the sinusoidal shape. It is implemented by converting the dq current references to polar (e.g., magnitude, phase) form and then limiting the magnitude to the allowed maximum value. Then the magnitude and phase are converted back to rectangular (i.e., dq) coordinates and later to the three-phase current references are processed as before. This block is placed between the VSG algorithm block and the hysteresis current controller, as shown in Figure 5-9.

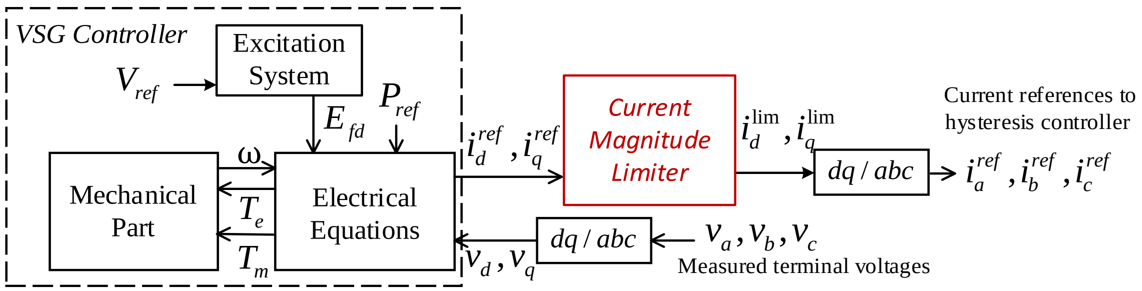

Figure 5-9 Controller Structure with Current Magnitude Limiter

The details of this current magnitude limiter block are in Figure 5-10. The magnitude of the ac current reference $\sqrt{(i_d^{ref})^2 + (i_q^{ref})^2}$ is limited to a maximum value of I_{max}. The limited magnitude and phase are then converted back into the abc domain. The inverse Park transformation is used to generate the phase current references i_a^{ref}, i_b^{ref} and i_c^{ref} from i_d^{lim}, i_q^{lim} for passing on to the hysteresis current controller. The angle θ is available from the VSG algorithm and is obtained by integrating ω.

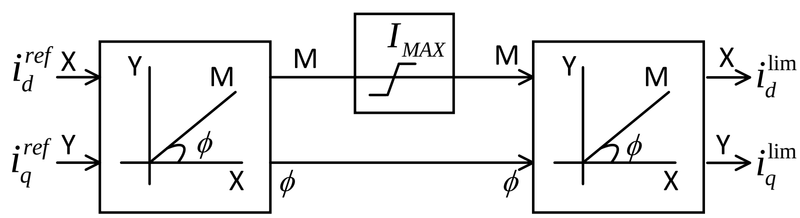

Figure 5-10 Current Magnitude Limiter

5.3.3 Virtual Rotor Speed Reset Mechanism

As mentioned in section 2.3.3, the virtual rotor speed ω continues to increase during the fault due to the power output suddenly dropping to near zero, just as the rotational speed of a real generator would be. If the fault duration is too long, ω will increase to an unacceptably large value so that the converter "loses synchronism" with the external system. Then the converter needs to be disconnected from the system. This is what would happen with a real SG.

However, the VSG provides us with an opportunity to avoid this, as we are free to set the computed ω in the equations to a desired value. Hence a reset mechanism is introduced to reset the value of ω to unity during the fault and so can prevent the VSG from losing synchronism (unlike a real machine, where this is ***impossible*** as our mentor, dearly departed *Prof. Akihiro Ametani* would have said). Some simulation results are shown later to prove this conclusion.

As this mechanism should only be activated during a fault, it is key for the control system to identify the system's fault. A '<u>fault detection block</u>' is used to achieve this function as shown in Figure 5-11.

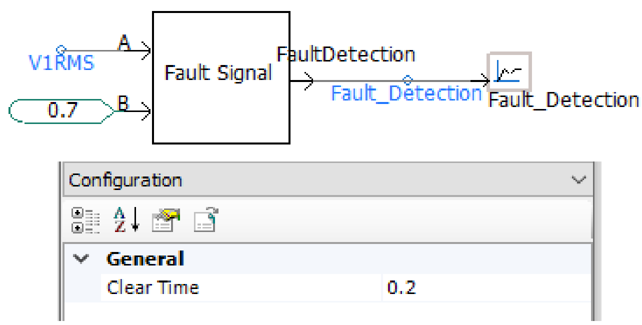

Figure 5-11 Fault Signal Block

A fault is assumed to occur if the converter terminal's voltage magnitude falls below a threshold value (e.g., $0.7\,pu$) and is assumed to be cleared after the voltage recovers above the threshold for more than a clearing time (typically $200\,ms$). The threshold and clearing times can be selected by the user and were determined by trial and error in this case.

5.4 VSG Operation with Detailed SM Emulation

In this section, the proposed detailed SM emulation VSG controller is implemented with an MMC to demonstrate its effectiveness. Firstly, both the current limiting block and the virtual ω reset mechanism are removed to show the potential damaging over-current and loss of synchronism during fault.

Later, the current limiting function is activated to make sure the valves are operated under a safe range. Finally, the advantage of the virtual rotor speed reset mechanism to prevent losing synchronism is shown with longer faults.

5.4.1 Layout of Modular Multilevel Converter System

A simple transmission scenario with an MMC is shown in Figure 5-12. An MMC connects with an ac system, which is represented by a voltage source and Thevenin impedance $Z_s = R_s + jX_s$, through a transformer and a $100\ km$ transmission line. The short circuit ratio (SCR) of the ac system is 4.5 and the angle of Z_s is $85°$. The MMC has 200 submodules per arm, and it is assumed that the remote converter controls the dc side voltage to its desired value of $\pm 150\ kV$. The parameters of example system and its corresponding MMC controllers are given in Table 5-2 to Table 5-5.

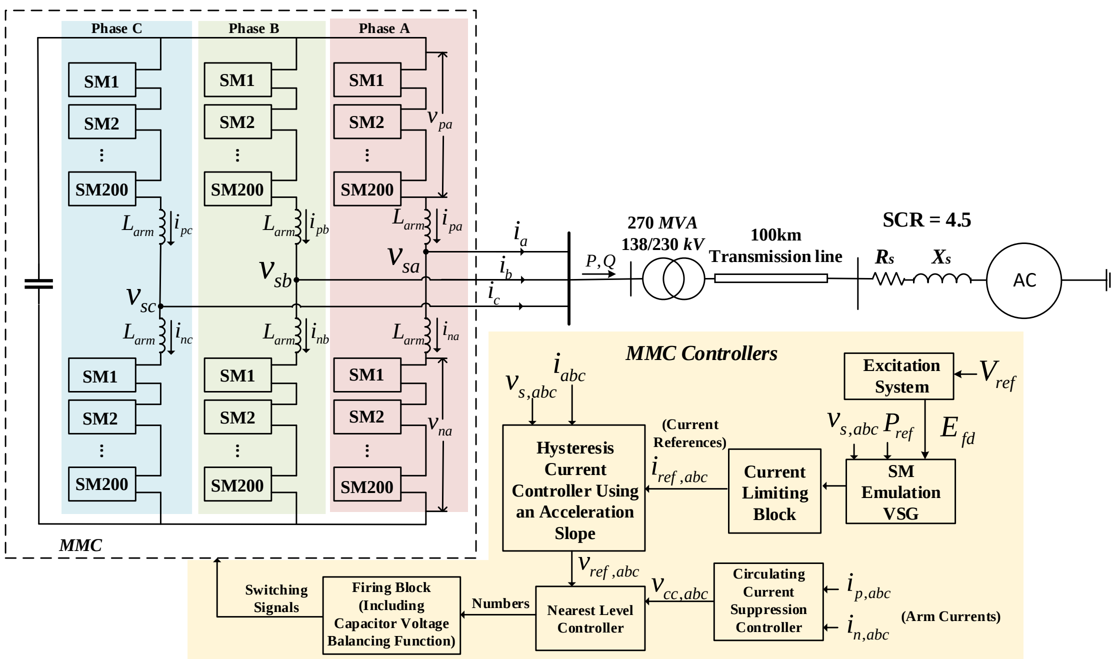

Figure 5-12 System Layout with MMC

Table 5-2 Main System Parameters

Parameter	Value	Parameter	Value
Dc side voltage V_{dc}	$\pm 150\ kV$	Transformer MVA	$270\ MVA$
Dc side shunt resistance	$2 \times 100000\ \Omega$	Transformer voltage	138/230 kV
Converter rated power	$250\ MVA$	Transformer resistance	0.02 pu
Converter rated voltage	$138\ kV$ (L-L)	Transformer inductance	0.15 pu
MMC arm inductance	$0.029H$	Transmission line	$100\ km$
System frequency	$60Hz$	Ac system SCR	4.5

Table 5-3 Parameters of Hysteresis Current Controller using Acceleration Current Slope

Parameter	Value	Parameter	Value
Equivalent inductance	$0.0145\ H$	Δ_s mode	Variable Mode
Half of hysteresis band (hy)	$0.01\ pu$		

Table 5-4 Parameters of Excitation System

Parameter	Value	Parameter	Value
The upper limit on the error V_{IMAX}	$10.0\ pu$	The lower limit on the error V_{IMIN}	$-10.0\ pu$
Lead time constant T_C	$1.0\ s$	Leg time constant T_B	$10.0\ s$
Regulator integral gain K_A	$200.0\ pu$	Regular time constant T_A	$0.015\ s$
Maximum regulator output V_{RMAX}	$5.64\ pu$	Minimum regulator output V_{RMIN}	$-4.53\ pu$
Rectifier loading factor K_C	$0.0\ pu$	The voltage filter time constant T_r	$0.02\ s$

Table 5-5 Parameters of Detailed SM Emulation VSG

Parameter	Value	Parameter	Value
Inertia constant H	$2.0\ s$	Leakage inductance L_a	$0.15\ pu$
Damping constant D	5.0	d-axis mutual inductance L_{md}	$1.50\ pu$
Stator resistance R_a	$0.0043\ pu$	field winding inductance L_{fd}	$0.119\ pu$
d-axis damper resistance R_{1d}	$0.01823\ pu$	d-axis damper inductance L_{1d}	$0.1097\ pu$
q-axis No.1 damper resistance R_{1q}	$0.0104\ pu$	q-axis No.1 damper inductance L_{1q}	$0.395\ pu$
q-axis No.2 damper resistance R_{2q}	$0.0167pu$	q-axis No.2 damper inductance L_{2q}	$0.0669\ pu$
field winding resistance R_{fd}	$0.0008947pu$	q-axis mutual inductance L_{mq}	$1.44\ pu$
Reference active power P_{ref}	$1.0\ pu$	Reference voltage V_{ref}	$1.0\ pu$

5.4.2 Fault Recovery Demonstration Without Current Limiting Block

To validate the detailed SM emulation VSG, the system is simulated and allowed to reach a steady state. A three-phase to ground fault is applied at the midpoint of the transmission line at $1.0s$ and the duration is $0.15s$ (9 cycles). Figure 5-13 (a) shows the output active power P from the MMC. Figure 5-13 (b) is the RMS value of the MMC terminal voltages V_{RMS}, and the three-phase voltage of MMC terminal is given in Figure 5-14. Note that the voltage does not drop to zero at the PCC because the fault is relatively remote. Figure 5-13 (c) is the magnitude of the output currents I_{mag}. Also, the virtual rotor speed ω is shown in Figure 5-13 (d). Figure 5-15 shows the upper arm current of phase a and one submodule's capacitor voltage (phase 'a' upper arm).

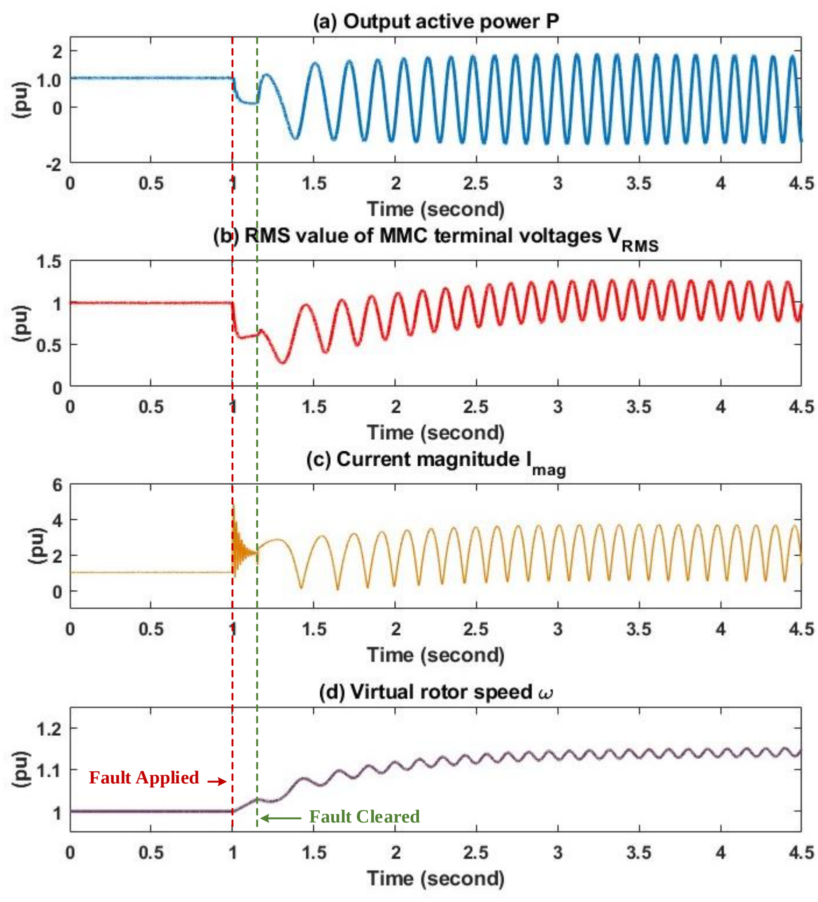

Figure 5-13 Unstable Simulation Results with a Solid Three-Phase Fault

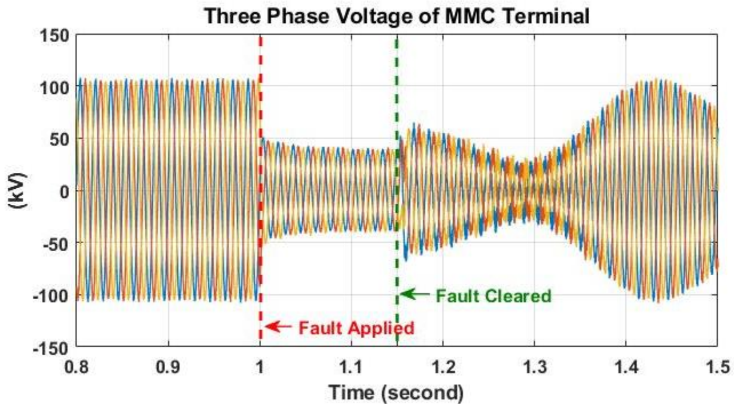

Figure 5-14 Three-Phase Voltage of MMC Terminal

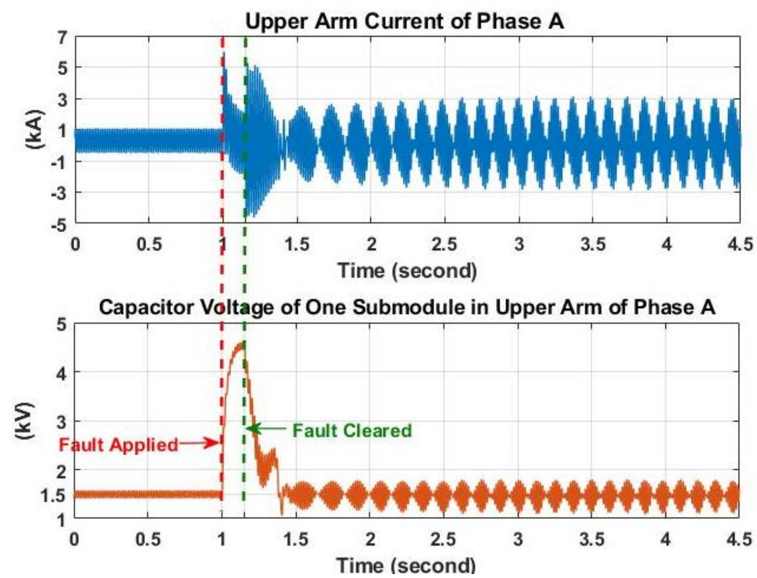

Figure 5-15 Phase ‘a’ Arm Current and Submodule Voltage

From the simulation results, the MMC operates in the steady state with $P = 1.0\ pu$ and $V_{RMS} = 1.0\ pu$. When the three-phase to ground fault is applied at $1.0\ s$, the output power P drop to a low value as seen in Figure 5-13 (a). The terminal voltage (three-voltage waveforms in Figure 5-14) experiences a reduction of approximately 40% from its steady-state value. While the magnitude of the currents I_{mag} increases to almost $5.0\ pu$ and the arm current also increases to a large value (around $6\ kA$), which would damage the converter’s IGBT switches. Also, ω keeps increasing during the fault period and eventually the VSG loses synchronism. The capacitor voltage of submodule maintains at $1.5\ kV$ in steady state and increases to $4.5\ kV$ during the fault.

After the fault is cleared at $1.15\ s$, the system did not recover to the former operating point and becomes unstable. The frequency of the MMC deviates from the nominal frequency too far, so the converter loses synchronism with the external ac system.

The simulation results indicate that the MMC with the detailed SM emulation VSG has a bad performance of the fault ride-through capability in this particular test system. The next examples show that the current limiting block and the virtual rotor speed reset mechanism are necessary to improve the system's operation.

5.4.3 Fault Recovery Demonstration with Current Limiting Block and Without Virtual ω Reset Mechanism

A current magnitude limiting block used to protect the converter from any over-current damage is indispensable in the MMC system. This block is purposed to regulate the magnitude of output currents to a safe level, e.g., $1.2\ pu$ in our example. Then, the direct hard current limiting block is also tested to show its effectiveness.

Firstly, a $0.15\ s$ (9 cycles) three-phase-to-ground fault is applied at the mid-point of the transmission line at $1.0\ s$ to show that the current limiter does indeed work. Then, a longer fault that lasts $0.30\ s$ (18 cycles) is applied to show the necessity of the virtual ω reset mechanism.

5.4.3.1 VSG with Current Magnitude Limiter: Response to 9-Cycle Three Phase to Ground Fault

The simulation results with the $0.15\ s$ (9 cycles) fault are shown in Figure 5-16 to Figure 5-18. In this example, the current magnitude limiting block is active. However, the virtual ω reset mechanism is removed.

Figure 5-16 shows (a) the output active power P of the MMC and (b) the RMS terminal voltage V_{RMS}. From the figure, the system can reach steady state operation with $P = P_{ref} = 1.0\ pu$ and $V_{RMS} = V_{ref} = 1.0\ pu$. Unlike the former case without the current limiting block (see Figure 5-13), the MMC can recover to the same operating point after the three-phase fault. It is proven that the current magnitude limiting block improves the MMC system stability.

Figure 5-17 (a) is the magnitude of the output currents I_{mag} and (b) shows the zoomed-in plot of the instantaneous three-phase currents. According to the simulation results, the magnitude of valve currents is essentially limited below $I_{max} = 1.2\, pu\ (or\ 1.5\, kA)$ during the fault situation. This also indicates that the proposed hysteresis current controller using acceleration slope works effectively in steady state and fault condition with the controlled output current always tracking the references.

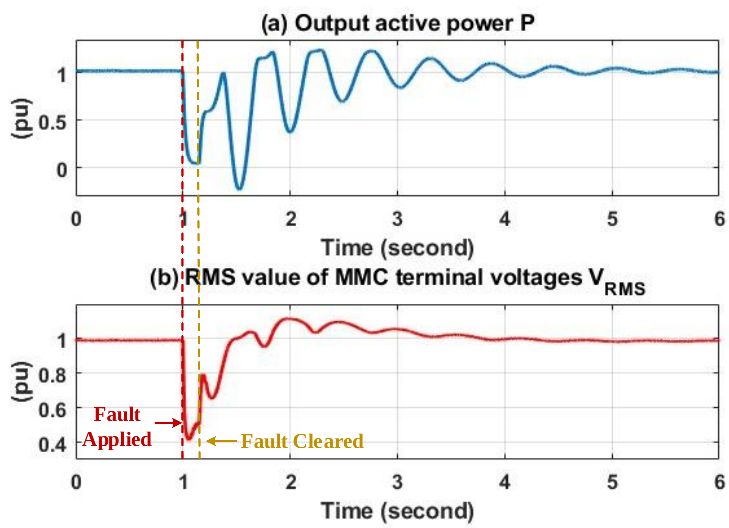

Figure 5-16 Waveforms of Output Active Power P and RMS value of terminal voltage V_{RMS} (VSG with Current Magnitude Limiter; $0.15\ s$ Fault Period)

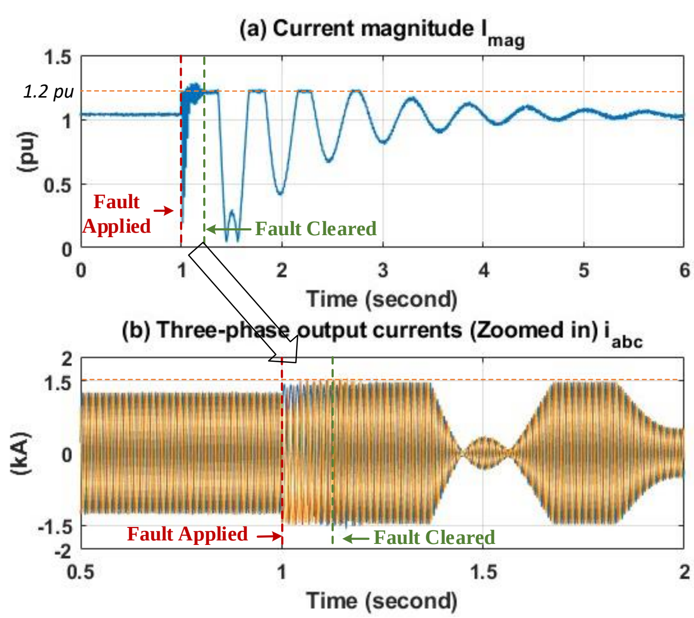

Figure 5-17 Current Magnitude (VSG with Current Magnitude Limiter; $0.15\ s$ Fault Period)

Figure 5-18 shows the virtual rotor speed ω of the VSG, which transiently oscillates between $0.965\ pu$ and $1.03\ pu$ but quickly settles down to the steady state speed of $1.0\ pu$, indicating that in addition to limiting the current, the current limiter also improves the stability, when compared to the system without current limiting plotted in Figure 5-13.

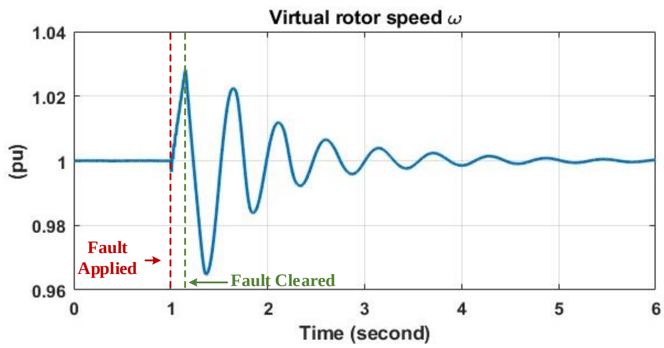

Figure 5-18 Virtual Rotor Speed (VSG with Current Magnitude Limiter; $0.15\ s$ Fault Period)

5.4.3.2 VSG with Current Magnitude Limiter: Response to Longer Duration Three Phase to Ground Fault

The simulation results with the $0.3\ s$ (18 cycles) fault are shown in Figure 5-19..

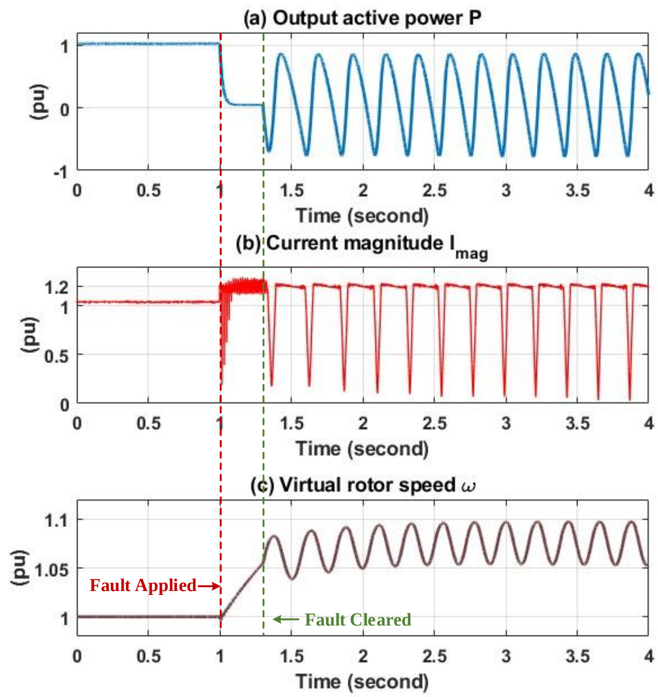

Figure 5-19 Simulation Results with $0.3\ s$ Three Phase to Ground Fault (VSG with Current Magnitude Limiter and Without ω Reset Mechanism)

It can be observed that the system becomes unstable after the fault is cleared. The virtual rotor speed becomes sufficiently large as seen in Figure 5-19 (c) so that the MMC loses synchronism with the external ac system. The next section will show that this instability can be avoided with the introduction of the virtual ω reset mechanism.

5.4.3.3 VSG with Direct Hard Current Limiter: Response to 9-Cycle and 18-Cycle Three Phase to Ground Faults

One of the advantages of the current magnitude limiting approach discussed in section 5.3.2 has the advantage that the injected current waveforms are sinusoidal. On the other hand, the direct hard limiting approach introduced in section 5.3.1 simply hard limits the current to the designated peak value, so that the waveform is no longer sinusoidal when the current reaches its limit. Also, the direct hard limiter is very simple to implement and avoids additional computations required for computing phase and magnitude as in Figure 5-10.

This section investigates the VSG's response when the current is hard limited with the fault situations discussed before, i.e., the 9-cycle and 18-cycle three-phase to ground faults. The simulation results are shown in Figure 5-20.

The behavior is similar to that with the current magnitude limiter, except that the current waveforms are no longer sinusoidal. From the zoomed-in plot of the system currents, the instantaneous values of the system currents are limited to $1.1\ pu\ (1.4\ kA)$.

The MMC system can reach a steady state successfully. Unlike the case without any current limiters (see Figure 5-13), the MMC can recover to the same operating points after a $0.15\ s$ fault with the help of the direct hard current limiter. It proves that the direct current limiter also improves the stability and fault ride-through capability of the system, although the current waveform is no longer sinusoidal once the limit kicks in.

However, if the fault duration is longer, e.g., $0.3\ s$, the system becomes unstable after the fault is cleared as shown in Figure 5-20 (b), where the MMC loses synchronism with the external ac system, just as it did with the current magnitude limiting option. Nevertheless, further simulation in the next section indicates that this instability can be avoided with the introduction of the virtual ω reset mechanism.

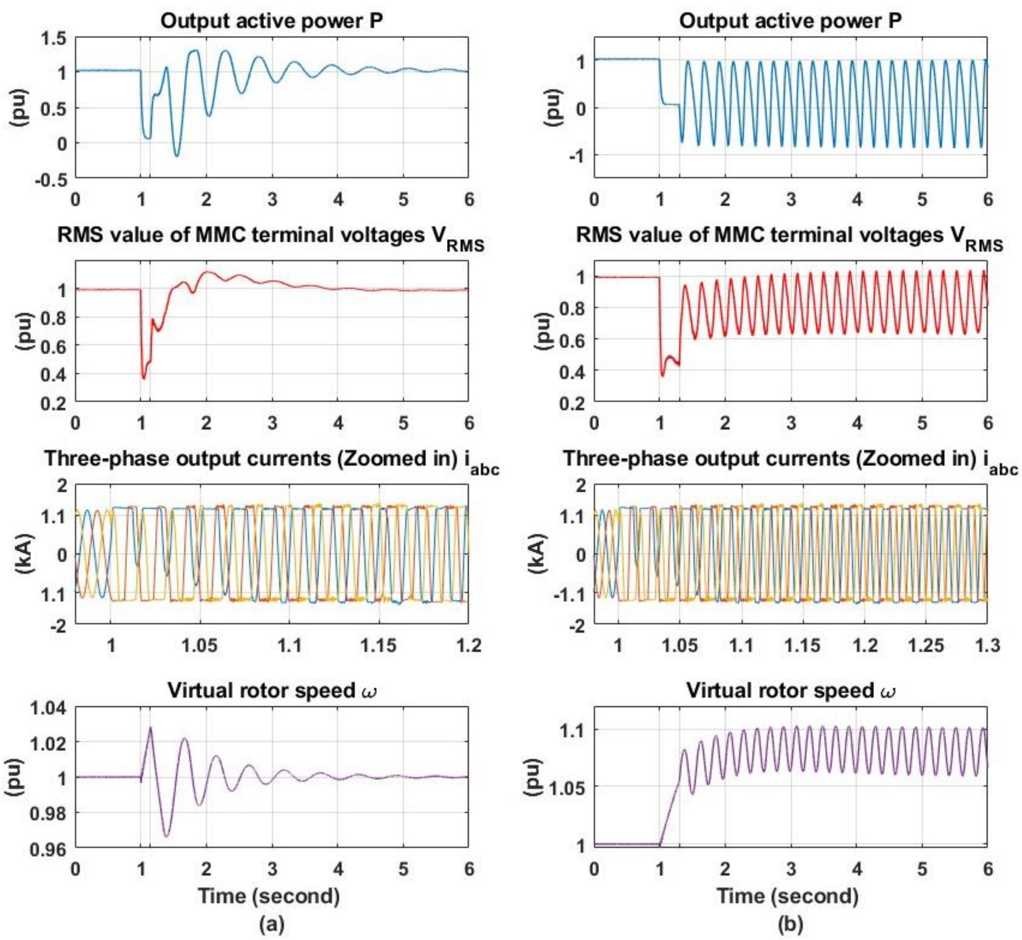

Figure 5-20 Fault Response of VSG with Direct Hard Current Limiter and without ω Reset Mechanism. (a) $0.15\ s$ Three-Phase to Ground Fault, (b) $0.3\ s$ Three-Phase to Ground Fault

5.4.4 Fault Recovery Demonstration with Current Limiting and Virtual ω Reset Mechanism

From Figure 5-19 and Figure 5-20, the VSG with either the magnitude limiter or the direct hard current limiter showed the loss of synchronism for long-duration faults. To rectify this, an additional control mechanism that we refer to as the “virtual rotor speed reset” have to be introduced and was elaborated in section 5.3.3. As was earlier shown, a $0.30\ s$ (18 cycles) three-phase to ground fault is applied at the midpoint of the transmission line at $1.0\ s$. The simulation results are in Figure 5-21.

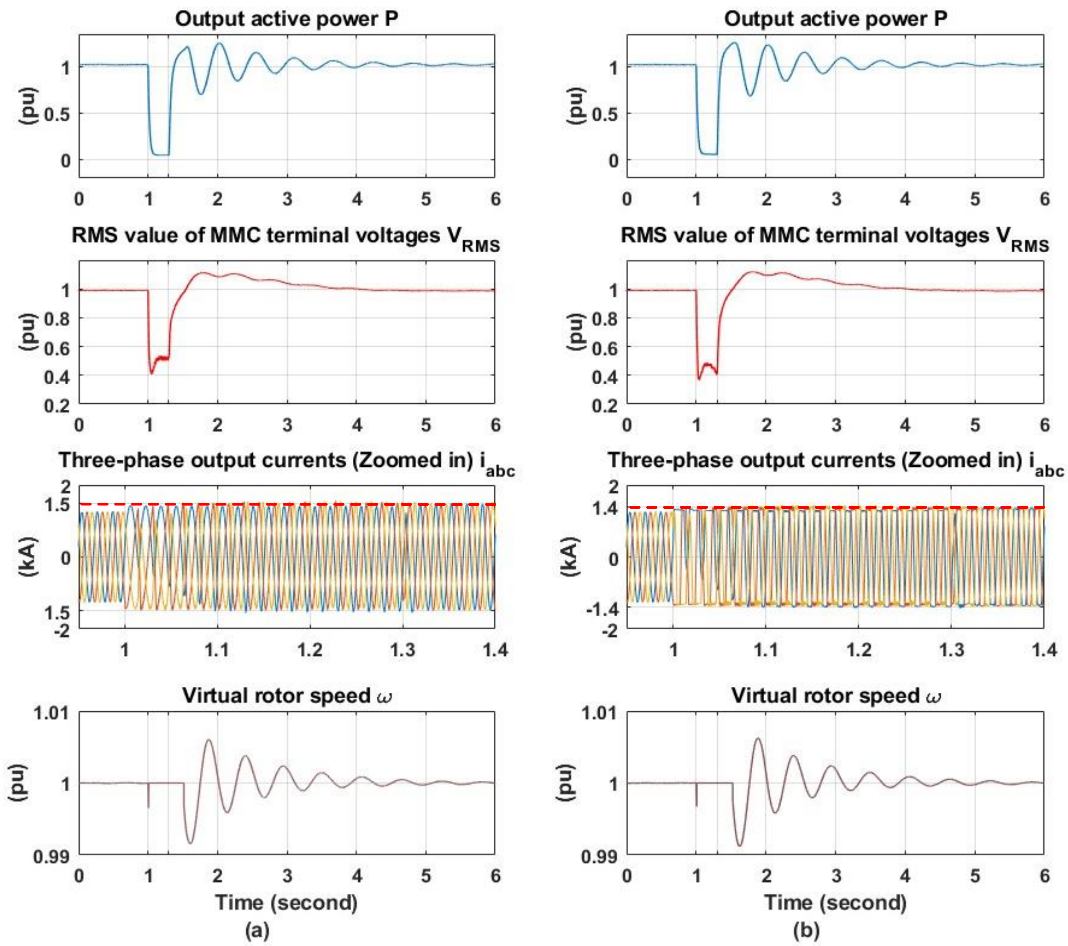

Figure 5-21 0.3 s Fault Response of VSG Controller with ω Reset Mechanism. (a) with Current Magnitude Limiter. (b) with Direct Hard Current Limiter

Note that in Figure 5-21, (a) shows the waveforms from the VSG with the current magnitude limiter, and (b) indicates the waveforms from the VSG with the direct hard current limiter. From the power and voltage waveforms, both systems can maintain stable operation and recover to steady state operation with $P = P_{ref} = 1.0\ pu$ and $V_{RMS} = V_{ref} = 1.0\ pu$ after the three-phase fault.

Then as seen in the three-phase current waveforms (i_{abc}), the current magnitude limiter (figure on the left side) indeed limits the magnitude of valve currents below $1.5\ kA$ while keeping the sinusoidal shape. On the other hand, although the current waveform is no longer sinusoidal once the current gets limited, the direct hard current limiter (figure on the right side) also regulates the instantaneous currents under $1.4\ kA$ during the operation.

Finally focusing on the virtual rotor speed ω of MMC, unlike the case in Figure 5-19, both VSG options can maintain synchronism with the external ac system with the help of the virtual ω reset mechanism.

Table 5-6 summarizes the stability of the simulation cases with different controllers discussed above. The waveforms for the cases in parentheses are omitted for brevity, but the conclusions regarding stability are as listed.

Table 5-6 Stability Summary

Controller Type / Fault Type	Pure VSG	VSG with Current Magnitude Limiter	VSG with Direct Hard Current Limiter	VSG with Current Magnitude Limiter and ω Reset Mechanism	VSG with Direct Hard Current Limiter and ω Reset Mechanism
0.15 s Three-Phase-to Ground Fault	Unstable	Stable	Stable	(Stable)	(Stable)
0.30 s Three-Phase-to Ground Fault	(Unstable)	Unstable	Unstable	Stable	Stable

In conclusion, adding a current limiting block to the VSG can improve the stability and fault ride-through capability of the MMC. Additionally, the performance can be further improved if the virtual rotor speed reset mechanism is active. Doing this helps the MMC to ride through more severe faults. In the VSG, we can reset the virtual rotor speed which is not the case with a real SG since the SG has no ability to reset the rotor speed. Its rotor speed keeps increasing during the fault (due to a mismatch between prime-mover input power and the output power). Thus, it is understandable that it has better fault ride-through capability than an actual SG would have.

5.5 Chapter Conclusion

With the proposed hysteresis current controller using acceleration slope introduced in Chapter 3, the current source interfaced virtual synchronous generator (VSG) strategy is achieved in this chapter, which is the detailed synchronous machine (SM) emulation VSG.

The principal contributions in this chapter are as follows:

1. The VSG based on detailed SM emulation was introduced.
    a) This VSG control considers a highly detailed machine representation that includes the d-axis and q-axis damper winding.
    b) Also, this type of representation inherently imparts a damping torque for speed deviations from synchronous speed.
2. Any VSG implementation must include current limitations to protect the valves from overcurrent damage. Two different current limiting methods were introduced.
    a) If a current controlled VSG is used for implementing, the current limitation is straightforward. It can be achieved directly by hard limiting the phase current reference to the hysteresis controller or by limiting only the magnitude of the sinusoidal current. The dynamics of current limiting are much faster than what is possible with a traditional voltage source interfaced implementation which uses decoupled dq axis controller to implement a current order.
    b) Furthermore, adding a virtual rotor speed reset mechanism to the VSG locks the virtual rotor speed ω to its nominal value when an unexpected situation such as a fault is detected and improves the ability of the VSG to survive a loss of synchronism with the external ac system.
3. The detailed SM emulation VSG with the current limiting block was tested in Electromagnetic Transients (EMT) simulation (PSCAD/EMTDC) to validate its effectiveness.
    a) The example used an MMC system that connects to an ac system through a transmission line.
    b) The simulation results show that without the current limiting block, this specific MMC system can lose synchronism. The system becomes unstable after a $150\,ms$ three-phase-to-ground fault.
    c) Adding a current limiting function (either hard limiting or magnitude limiting) improves the stability behavior for short-duration faults.
    d) Introducing an ω reset function can further improve the stability significantly. The MMC keeps synchronism with the external system and

can recover to a steady state after a long-duration fault. This proves the MMC with the added functions has a good fault ride-through capability.

6 Small Signal Analysis of Detailed SM Emulation VSG

The work in this Chapter has been published in the Electric Power System Research journal (EPSR) in Oct 2023 as "Chen Jiang, Ajinkya D. Sinkar, Aniruddha M. Gole, 'Small signal analysis of a grid-forming modular multilevel converter with a novel virtual synchronous generator control', Electric Power Systems Research, Volume 223, 2023".

This chapter investigates the performance of VSGs with different levels of detail in the SG's representation (e.g., different number of damper windings, etc.). It also develops small signal models of these representations and validates them using Electromagnetic Transients (EMT) simulation. In addition, the VSG configurations are investigated when connected to ac networks of different strengths - represented by short circuit ratios (SCR) - ranging from weak ($SCR < 2.0$) to ultra-strong ($SCR > 30$). Root locus analysis is carried out to investigate the stability and damping performance when the VSG representation uses a different number of damper windings. It is shown that including damper windings inside the VSG results in a well-damped transient response. Also, as the VSG parameters need not be constrained to the values of a physical machine, the use of artificially optimized parameters is investigated to provide better performance.

6.1 Small Signal Model of Detailed SM emulation VSG

The small signal model of the detailed VSG with one damper winding each in the d- and q-axes is first derived, then the other VSG options with a different number of damper windings can be easily obtained by removing/adding the corresponding differential equations of the damper windings.

Note, the subscript of the matrices in this section indicates the number of the d- and q-axis windings. For example, the incremental state variables vector of the VSG option in Figure 6-1 is designated as $\boldsymbol{\Delta x}_{32}$. The subscript '3.2' is because this VSG has three windings in the d-axis consisting of the magnetizing branch (L_{md}), field inductance (L_{fd}) and damper winding inductance (L_{1d}), and two windings in the q-axis (L_{mq}, L_{1q}).

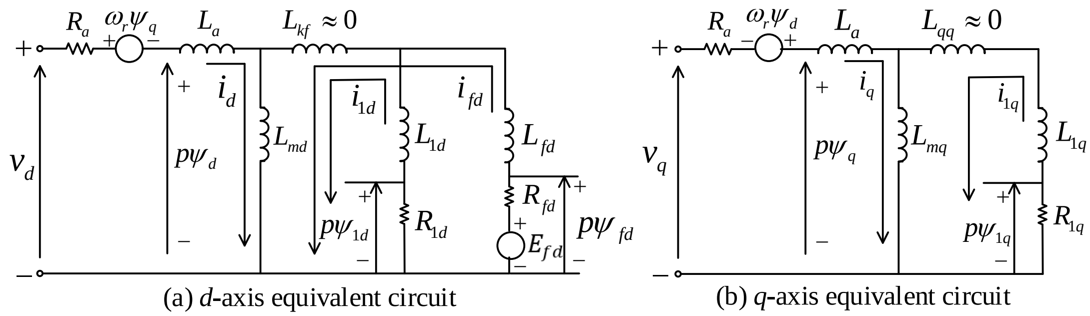

Figure 6-1 Equivalent Circuits of ‘3.2’ VSG

6.1.1 Small Signal Model of SM Emulation VSG (‘3.2’ VSG)

Developed here is a small signal model for a detailed implementation of the VSG which has 3 parallel windings in the d-axis (including a magnetizing branch, a field winding, and a damper winding) and two parallel windings in the q-axis (including a magnetizing branch and a damper winding), i.e., a ‘3.2’ representation. The mathematical derivation can be achieved by dividing the problem into four different parts, viz. i) the electrical windings, ii) the excitation system, iii) the external system, and iv) the mechanical component model. Then the completed small signal model can be obtained by combining these parts.

6.1.1.1 Small Signal Model of Electrical Windings

According to the relationships between fluxes and current shown in section 5.2.1, the small signal model of these linear equations is straightforward as shown in (6-1) to (6-5), and its matrix format is in (6-6) and (6-7).

$$\Delta\psi_d = (L_a + L_{md})\Delta i_d + L_{md}\Delta i_{1d} + L_{md}\Delta i_{fd} \tag{6-1}$$

$$\Delta\psi_{1d} = L_{md}\Delta i_d + \left(L_{1d} + L_{kf} + L_{md}\right)\Delta i_{1d} + \left(L_{kf} + L_{md}\right)\Delta i_{fd} \tag{6-2}$$

$$\Delta\psi_{fd} = L_{md}\Delta i_d + \left(L_{kf} + L_{md}\right)\Delta i_{1d} + \left(L_{fd} + L_{kf} + L_{md}\right)\Delta i_{fd} \tag{6-3}$$

$$\Delta\psi_q = \left(L_a + L_{mq}\right)\Delta i_q + L_{mq}\Delta i_{1q} \tag{6-4}$$

$$\Delta\psi_{1q} = L_{mq}\Delta i_q + \left(L_{1q} + L_{qq} + L_{mq}\right)\Delta i_{1q} \tag{6-5}$$

$$\Delta\boldsymbol{\psi}_{\mathbf{32}} = \begin{pmatrix} \Delta\psi_d \\ \Delta\psi_{1d} \\ \Delta\psi_{fd} \\ \Delta\psi_q \\ \Delta\psi_{1q} \end{pmatrix} = \boldsymbol{L}_{\mathbf{32}}\,\boldsymbol{\Delta I}_{\mathbf{32}} = \boldsymbol{L}_{\mathbf{32}} \begin{pmatrix} \Delta i_d \\ \Delta i_{kd} \\ \Delta i_{fd} \\ \Delta i_q \\ \Delta i_{1q} \end{pmatrix} \tag{6-6}$$

Here,

$$\boldsymbol{L}_{\mathbf{32}} = \begin{pmatrix} L_a + L_{md} & L_{md} & L_{md} & 0 & 0 \\ L_{md} & L_{kd} + L_{kf} + L_{md} & L_{kf} + L_{md} & 0 & 0 \\ L_{md} & L_{kf} + L_{md} & L_{fd} + L_{kf} + L_{md} & 0 & 0 \\ 0 & 0 & 0 & L_a + L_{mq} & L_{mq} \\ 0 & 0 & 0 & L_{mq} & L_{1q} + L_{qq} + L_{mq} \end{pmatrix} \tag{6-7}$$

From which it follows that:

$$\boldsymbol{\Delta I}_{\mathbf{32}} = \boldsymbol{L}_{\mathbf{32}}^{\mathbf{-1}}\,\Delta\boldsymbol{\psi}_{\mathbf{32}} \tag{6-8}$$

Also based on Figure 6-1, the relationship between the winding fluxes and voltages can be linearized giving their small signal counterparts as shown in (6-9) to (6-13). Note that all the variables are in per-unit except 'time (second)', therefore, giving rise to the scaling factor $1/\omega_n$, where ω_n is the nominal rotor speed (equal to 120π in the $60\ Hz$ system). The superscript '0' denotes the steady state value around which the equations are linearized.

$$\frac{1}{\omega_n}\frac{d\Delta\psi_d}{dt} = \Delta v_d - R_a\Delta i_d - \omega^0\Delta\psi_q - \psi_q^0\Delta\omega \tag{6-9}$$

$$\frac{1}{\omega_n}\frac{d\Delta\psi_{1d}}{dt} = -R_{1d}\Delta i_{1d} \tag{6-10}$$

$$\frac{1}{\omega_n}\frac{d\Delta\psi_{fd}}{dt} = \Delta E_{fd} - R_{fd}\Delta i_{fd} \tag{6-11}$$

$$\frac{1}{\omega_n}\frac{d\Delta\psi_q}{dt} = \Delta v_q - R_a\Delta i_q + \omega^0\Delta\psi_d + \psi_d^0\Delta\omega \tag{6-12}$$

$$\frac{1}{\omega_n}\frac{d\Delta\psi_{1q}}{dt} = -R_{1q}\Delta i_{1q} \tag{6-13}$$

In the linearized differential equations above, the state variables vector $\boldsymbol{\Delta x}_{\mathbf{32}}$ includes the incremental flux linkages ($\Delta\psi_d,\ \Delta\psi_{1d},\ \Delta\psi_{fd},\ \Delta\psi_q,\ \Delta\psi_{1q}$) and the incremental field voltage (ΔE_{fd}). Although the incremental current variables ($\Delta i_d,\ \Delta i_{1d},\ \Delta i_{fd},\ \Delta i_q,\ \Delta i_{1q}$) are not state variables, they can be converted to the corresponding fluxes based on (6-8).

However, Δv_d and Δv_q are not state variables but will be substituted later with state variables by using the equations of the interconnected external system.

6.1.1.2 Small Signal Model of Excitation System

An IEEE-typed AC4A exciter model shown in Figure 5-5 is used to represent the excitation system in this example [68]. The small signal model of the excitation system is shown in Figure 6-2, where $K_A' = K_A \cdot \frac{R_{fd}}{L_{md}}$. Two state variables ΔX_{E1} and ΔX_{E2} are introduced to represent the internal states of the first-order lag blocks as shown in Figure 6-2.

In the dq reference frame, the voltage magnitude V is equal to $\sqrt{v_d^2 + v_q^2}$. Hence, its incremental value ΔV can be represented in (6-14), where V_l is the steady state voltage magnitude.

$$\Delta V = \frac{v_d^0}{\sqrt{(v_d^0)^2 + (v_q^0)^2}} \Delta v_d + \frac{v_q^0}{\sqrt{(v_d^0)^2 + (v_q^0)^2}} \Delta v_q = \frac{v_d^0}{V_l} \Delta v_d + \frac{v_q^0}{V_l} \Delta v_q \tag{6-14}$$

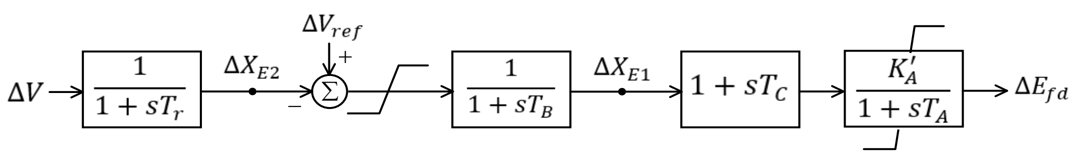

Figure 6-2 Small Signal Model of Excitation System

Using Figure 6-2, the small signal differential equations of the excitation system are in (6-15) to (6-17). The units of the time constants (T_r, T_B, T_A) are in 'second'.

$$\frac{d\Delta X_{E2}}{dt} = -\frac{1}{T_r}\Delta X_{E2} + \frac{v_d^0}{T_r V_l}\Delta v_d + \frac{v_q^0}{T_r V_l}\Delta v_q \tag{6-15}$$

$$\frac{d\Delta X_{E1}}{dt} = \frac{1}{T_B}\Delta V_{ref} - \frac{1}{T_B}\Delta X_{E1} - \frac{1}{T_B}\Delta X_{E2} \tag{6-16}$$

$$\frac{d\Delta E_{fd}}{dt} = -\frac{1}{T_A}\Delta E_{fd} + \frac{K_A'}{T_A}\left(1 - \frac{T_C}{T_B}\right)\Delta X_{E1} + \frac{K_A' T_C}{T_A T_B}\Delta V_{ref} - \frac{K_A' T_C}{T_A T_B}\Delta X_{E2} \tag{6-17}$$

The state variables ΔX_{E1}, ΔX_{E2} form two additional state variables of the state vector $\boldsymbol{x_{32}}$. However, Δv_d and Δv_q are not state variables that still need to be eliminated in the equations.

6.1.1.3 Small Signal Model of External Connection

This section derives the small signal model of a simple external system. Obviously, this could be highly detailed depending on the size and complexity of the system, but here we assume that the converter is connected to an ac system through an inductive line with impedance jX_s as shown in Figure 6-3. Usually, the resistance of the network R_s is quite smaller than the inductance X_s, therefore, $R_s$is ignored in this case.

The relationship between Δv_d, Δv_q and the state variables can be derived for this arrangement. Note that the positive direction of the current I is defined as flowing into the converter. Also. V_t is the converter's terminal voltage and $E_B\angle 0$ is the system's ac voltage phasor and is assumed to be constant.

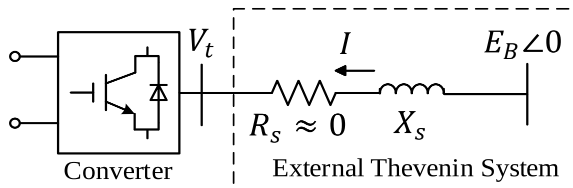

Figure 6-3 Equivalent External Power System

Based on Figure 6-3, (6-18) can be obtained:

$$V_t = V_R + jV_I = E_B - jX_s I = (E_B + j0) - jX_s(I_R + jI_I) \tag{6-18}$$

The phasor equations of the external system above are expressed in real-imaginary (RI) coordinates which rotate at a constant fundamental speed ($120\pi\, rad/s$ in this $60\, Hz$ system). This needs to be transformed into the dq reference frame (rotating at $\omega\, rad/s$) to be combined with the other VSG equations. Therefore, (6-18) is transferred into the dq coordinate as shown in Figure 6-4.

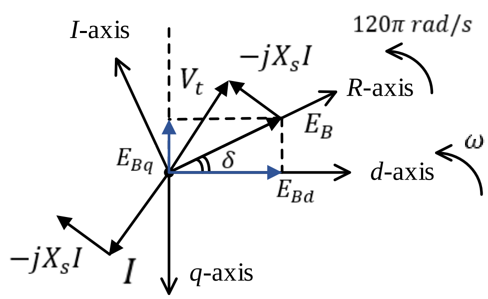

Figure 6-4 Phasor Relationship

In Figure 6-4, the q-axis lags the d-axis by $90°$, and the I-axis leads the R-axis by $90°$. The instantaneous angle between the R-axis and d-axis is defined as δ. Note this angle is <u>not</u> the virtual rotor angle θ mentioned above. Then $\Delta\delta$ in per-unit, as given by (6-19) becomes one of the state variables.

$$\frac{1}{\omega_n}\frac{d\Delta\delta}{dt} = -\Delta\omega \tag{6-19}$$

Also, the external system voltage E_B in dq reference frame can be obtained from the figure as shown in (6-20) and (6-21) below.

$$E_{Bd} = E_B \cdot cos\delta \tag{6-20}$$

$$E_{Bq} = -E_B \cdot sin\delta \tag{6-21}$$

Thus, (6-18) can be rewritten in the dq coordinate in (6-22) to (6-24).

$$v_d - jv_q = \left(E_{Bd} - jE_{Bq}\right) - jX_s\left(i_d - ji_q\right) \tag{6-22}$$

Here,

$$v_d = E_{Bd} - X_s i_q = E_B cos\delta - X_s i_q \tag{6-23}$$

$$v_q = E_{Bq} + X_s i_d = -E_B sin\delta + X_s i_d \tag{6-24}$$

The incremental values of the d- and q-axis components of the terminal voltage (v_d, v_q) are given by (6-25) and (6-26). These equations can be used to replace the voltages in (6-9), (6-12), and (6-15).

$$\Delta v_d = -E_B sin\delta^0 \cdot \Delta\delta - X_s \Delta i_q \tag{6-25}$$

$$\Delta v_q = -E_B cos\delta^0 \cdot \Delta\delta + X_s \Delta i_d \tag{6-26}$$

6.1.1.4 Small Signal Model of Mechanical System

It is assumed that a simple inertia damping model as given by (5-20) is used for the mechanical system. This could be extended to include more complex governor and turbine representations, however, that is beyond the scope of the present work.

According to (5-23), the small signal expression of the electrical torque is in (6-27).

$$\Delta T_e = i_q^0 \Delta\psi_d + \psi_d^0 \Delta i_q - i_d^0 \Delta\psi_q - \psi_q^0 \Delta i_d \tag{6-27}$$

Then combining (5-20), (5-22), and (6-27), the incremental rotor speed $\Delta\omega$ can be written as in (6-28). As ΔT_m in is approximately equal to ΔP_{ref} in the per-unit system, it is replaced by ΔP_{ref}. Also, the unit of time t and the inertia constant H is 'second'.

$$\frac{d\Delta\omega}{dt} = \frac{\Delta P_{ref}}{2H} - \frac{D_W}{2H}\Delta\omega - \frac{i_q^0}{2H}\Delta\psi_d - \frac{\psi_d^0}{2H}\Delta i_q + \frac{i_d^0}{2H}\Delta\psi_q + \frac{\psi_q^0}{2H}\Delta i_d \tag{6-28}$$

Based on (5-21), the small signal representation $\Delta\theta$ of the rotor angle θ is in (6-29). As only $\Delta\omega$ appears in the remaining state variable equations (not $\Delta\theta$), there is no need to include this equation in the overall state space model. $\Delta\theta$ can be obtained directly once $\Delta\omega$ is calculated.

$$\frac{1}{\omega_n}\frac{d\Delta\theta}{dt} = \Delta\omega \tag{6-29}$$

6.1.1.5 Complete Small Signal Model of '3.2' SM Emulation VSG

Combining the small signal differential equations ((6-9)-(6-13), (6-15)-(6-17), (6-19) and (6-28)) from electrical system, excitation system, external connection system, and mechanical model, the complete small signal model of this'3.2' VSG option (short for VSG which has three parallel windings in the d-axis and two parallel windings in q-axis) can be listed as follow in (6-30) to (6-39).

The reader is reminded that the superscript '0' on any variable indicates its steady-state value where the system is linearized. Also, V_l is equal to $\sqrt{(v_d^0)^2 + (v_q^0)^2}$, K_A' is short for $K_A \frac{R_{fd}}{L_{md}}$ and δ is the angle between the d-axis and R-axis.

$$\frac{1}{\omega_n}\frac{d\Delta\psi_d}{dt} = -X_s \Delta i_q - E_B sin\delta^0 \Delta\delta - R_a \Delta i_d - \omega^0 \Delta\psi_q - \psi_q^0 \Delta\omega \tag{6-30}$$

$$\frac{1}{\omega_n}\frac{d\Delta\psi_{1d}}{dt} = -R_{1d}\Delta i_{1d} \tag{6-31}$$

$$\frac{1}{\omega_n}\frac{d\Delta\psi_{fd}}{dt} = \Delta E_{fd} - R_{fd}\Delta i_{fd} \tag{6-32}$$

$$\frac{1}{\omega_n}\frac{d\Delta\psi_q}{dt} = X_s \Delta i_d - E_B cos\delta^0 \Delta\delta - R_a \Delta i_q + \omega^0 \Delta\psi_d + \psi_d^0 \Delta\omega \tag{6-33}$$

$$\frac{1}{\omega_n}\frac{d\Delta\psi_{1q}}{dt} = -R_{1q}\Delta i_{1q} \tag{6-34}$$

$$\frac{d\Delta\omega}{dt} = \frac{\Delta P_{ref}}{2H} - \frac{D_w}{2H}\Delta\omega - \frac{i_q^0}{2H}\Delta\psi_d - \frac{\psi_d^0}{2H}\Delta i_q + \frac{i_d^0}{2H}\Delta\psi_q + \frac{\psi_q^0}{2H}\Delta i_d \tag{6-35}$$

$$\frac{1}{\omega_n}\frac{d\Delta\delta}{dt} = -\Delta\omega \tag{6-36}$$

$$\frac{d\Delta E_{fd}}{dt} = -\frac{1}{T_A}\Delta E_{fd} + \frac{K_A'}{T_A}\left(1 - \frac{T_C}{T_B}\right)\Delta X_{E1} + \frac{K_A' T_C}{T_A T_B}\Delta V_{ref} - \frac{K_A' T_C}{T_A T_B}\Delta X_{E2} \tag{6-37}$$

$$\frac{d\Delta X_{E1}}{dt} = \frac{1}{T_B}\Delta V_{ref} - \frac{1}{T_B}\Delta X_{E1} - \frac{1}{T_B}\Delta X_{E2} \tag{6-38}$$

$$\frac{d\Delta X_{E2}}{dt} = -\frac{1}{T_r}\Delta X_{E2} + \frac{v_d^0}{T_r V_l}(-X_s)\Delta i_q + \frac{v_d^0}{T_r V_l}(-E_B \sin\delta^0)\Delta\delta + \frac{v_q^0}{T_r V_l}X_s\Delta i_d +$$

$$\frac{v_q^0}{T_r V_l}(-E_B \cos\delta^0)\Delta\delta \tag{6-39}$$

The matrix form of this '3.2' VSG small signal model is in (6-40).

$$\frac{d\boldsymbol{\Delta x_{32}}}{dt} = \boldsymbol{M_{32}\Delta x_{32}} + \boldsymbol{N_{32}\Delta i_{32}} + \boldsymbol{B_{32}\Delta u} \tag{6-40}$$

Here,

$$\boldsymbol{M_{32}} =$$

$$\begin{pmatrix}
0 & 0 & 0 & -\omega^0\omega_n & 0 & -\psi_q^0\omega_n & -E_B sin\delta^0\omega_n & 0 & 0 & 0 \\
0 & 0 & 0 & 0 & 0 & 0 & 0 & 0 & 0 & 0 \\
0 & 0 & 0 & 0 & 0 & 0 & 0 & \omega_n & 0 & 0 \\
\omega^0\omega_n & 0 & 0 & 0 & 0 & \psi_d^0\omega_n & -E_B cos\delta^0\omega_n & 0 & 0 & 0 \\
0 & 0 & 0 & 0 & 0 & 0 & 0 & 0 & 0 & 0 \\
-\frac{i_q^0}{2H} & 0 & 0 & \frac{i_d^0}{2H} & 0 & -\frac{D_w}{2H} & 0 & 0 & 0 & 0 \\
0 & 0 & 0 & 0 & 0 & -\omega_n & 0 & 0 & 0 & 0 \\
0 & 0 & 0 & 0 & 0 & 0 & 0 & -\frac{1}{T_A} & \frac{K_A'}{T_A}(1-\frac{T_C}{T_B}) & -\frac{K_A' T_C}{T_A T_B} \\
0 & 0 & 0 & 0 & 0 & 0 & 0 & 0 & -\frac{1}{T_B} & -\frac{1}{T_B} \\
0 & 0 & 0 & 0 & 0 & 0 & \frac{-E_B v_d^0 sin\delta^0 - E_B v_q^0 cos\delta^0}{T_r V_l} & 0 & 0 & -\frac{1}{T_r}
\end{pmatrix}$$

(6-41)

$$\boldsymbol{\Delta x_{32}} = \left(\Delta\psi_d\ \ \Delta\psi_{1d}\ \ \Delta\psi_{fd}\ \ \Delta\psi_q\ \ \Delta\psi_{1q}\ \Delta\omega\ \ \Delta\delta\ \ \Delta E_{fd}\ \ \Delta X_{E1}\ \ \Delta X_{E2}\right)^T \tag{6-42}$$

$$\boldsymbol{\Delta i_{32}} = \left(\Delta i_d \;\; \Delta i_{1d} \;\; \Delta i_{fd} \;\; \Delta i_q \;\; \Delta i_{1q} \; 0 \;\; 0 \;\; 0 \;\; 0 \;\; 0\right)^T \tag{6-43}$$

$$\boldsymbol{\Delta u} = (\Delta P_{ref} \quad \Delta V_{ref})^T \tag{6-44}$$

$$\boldsymbol{N_{32}} =$$

$$\begin{pmatrix} -R_a\omega_n & 0 & 0 & -X_s\omega_n & 0 & 0 & 0 & 0 & 0 & 0 \\ 0 & -R_{1d}\omega_n & 0 & 0 & 0 & 0 & 0 & 0 & 0 & 0 \\ 0 & 0 & -R_{fd}\omega_n & 0 & 0 & 0 & 0 & 0 & 0 & 0 \\ X_s\omega_n & 0 & 0 & -R_a\omega_n & 0 & 0 & 0 & 0 & 0 & 0 \\ 0 & 0 & 0 & 0 & -R_{1q}\omega_n & 0 & 0 & 0 & 0 & 0 \\ \frac{\psi_q^0}{2H} & 0 & 0 & -\frac{\psi_d^0}{2H} & 0 & 0 & 0 & 0 & 0 & 0 \\ 0 & 0 & 0 & 0 & 0 & 0 & 0 & 0 & 0 & 0 \\ 0 & 0 & 0 & 0 & 0 & 0 & 0 & 0 & 0 & 0 \\ 0 & 0 & 0 & 0 & 0 & 0 & 0 & 0 & 0 & 0 \\ \frac{v_q^0}{T_r V_l} X_s & 0 & 0 & -\frac{v_d^0}{T_r V_l} X_s & 0 & 0 & 0 & 0 & 0 & 0 \end{pmatrix} \tag{6-45}$$

$$\boldsymbol{B_{32}} = \begin{pmatrix} 0 & 0 & 0 & 0 & 0 & \frac{1}{2H} & 0 & 0 & 0 & 0 \\ 0 & 0 & 0 & 0 & 0 & 0 & 0 & \frac{K_A' T_C}{T_A T_B} & \frac{1}{T_B} & 0 \end{pmatrix}^T \tag{6-46}$$

The currents $\boldsymbol{\Delta i_{32}}$ in (6-40) can be replaced by the state variables $\boldsymbol{\Delta x_{32}}$ based on the relationship between current and fluxes as shown in (6-8). Note that the entries '$\boldsymbol{0}$' in (6-47) are 5×5 zero matrices, and $\boldsymbol{L_{32}}$ is given in (6-7).

$$\boldsymbol{\Delta i_{32}} = (\boldsymbol{L'_{32}})^{-\boldsymbol{1}} \boldsymbol{\Delta x_{32}} = \begin{pmatrix} \boldsymbol{L_{32}} & \boldsymbol{0} \\ \boldsymbol{0} & \boldsymbol{0} \end{pmatrix}^{-1} \boldsymbol{\Delta x_{32}} \tag{6-47}$$

From the above equations, the classical state variable form of the '3.2' SM emulation VSG small signal model is obtained as given in (6-48) below:

$$\frac{d\boldsymbol{\Delta x_{32}}}{dt} = \boldsymbol{A_{32}} \boldsymbol{\Delta x_{32}} + \boldsymbol{B_{32}} \boldsymbol{\Delta u} \tag{6-48}$$

$$\boldsymbol{A_{32}} = [\boldsymbol{M_{32}} + \boldsymbol{N_{32}} (\boldsymbol{L'_{32}})^{-\boldsymbol{1}}] \tag{6-49}$$

6.1.1.6 Model Validation Using EMT Simulation

The proposed small signal (SS) model of the '3.2' VSG controller is validated by matching its transient response with a fully detailed model in an EMT simulation program (PSCAD/EMTDC). The system layout is in Figure 6-5 below and its parameters are in Table 6-1 to Table 6-3.

The SS model is linearized at the operating point where the output power of the MMC (P_t) is $1.0\ pu$. A step change in the active power reference ($\Delta P_{ref} = -0.1\ pu$) is applied in the EMT simulation as well as in the SS models.

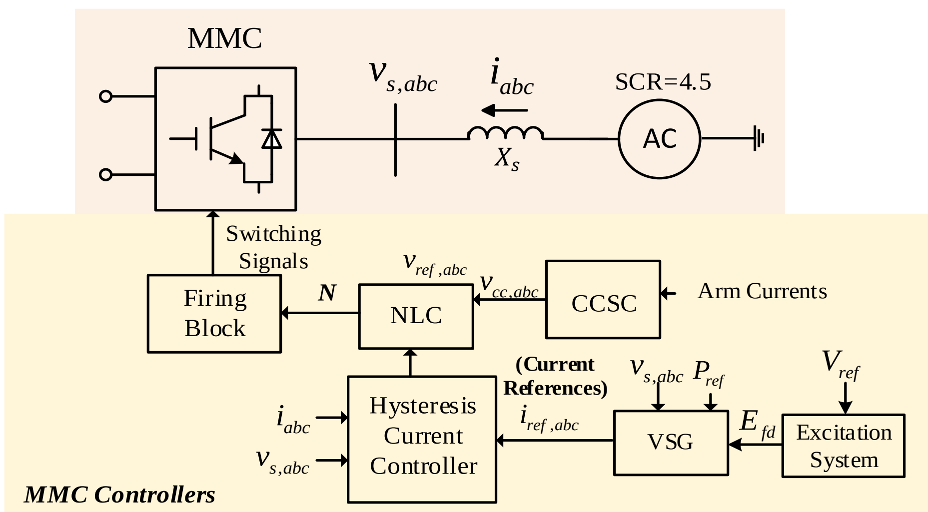

Figure 6-5 Test System Layout

Table 6-1 System Parameters

Parameter	Value	Parameter	Value
DC side voltage V_{dc}	$\pm 150\ kV$	System frequency	$60Hz$
Converter rated power	$270\ MVA$	Converter rated voltage	$180kV$ (L-L, RMS)
System Short Circuit Ratio	4.5	MMC level	11

Table 6-2 Parameters of Excitation System

Parameter	Value	Parameter	Value
Lead time constant T_C	$1.0\ s$	Leg time constant T_B	$10.0\ s$
Regulator integral gain K_A	200.0	Regular time constant T_A	$0.015\ s$
Voltage filter constant T_r	$0.02\ s$		

Table 6-3 Parameters of ‘3.2’ VSG

Parameter	Value	Parameter	Value
Inertia constant H	3.42 s	Leakage inductance L_a	0.015 pu
Damping constant D_w	5.0	d-axis mutual inductance L_{md}	2.0 pu
Stator resistance R_a	0.0043 pu	field winding inductance L_{fd}	0.119 pu
d-axis damper resistance R_{1d}	0.01823 pu	d-axis damper inductance L_{1d}	0.1097 pu
q-axis damper resistance R_{1q}	0.0104 pu	q-axis damper inductance L_{1q}	0.395 pu
field winding resistance R_{fd}	0.0008947pu	q-axis mutual inductance L_{mq}	1.44pu

Figure 6-6 shows the transients of the virtual rotor speed obtained from the SS model ω_{SS} and EMT simulation ω_{EMT} of the ‘3.2’ VSG option.

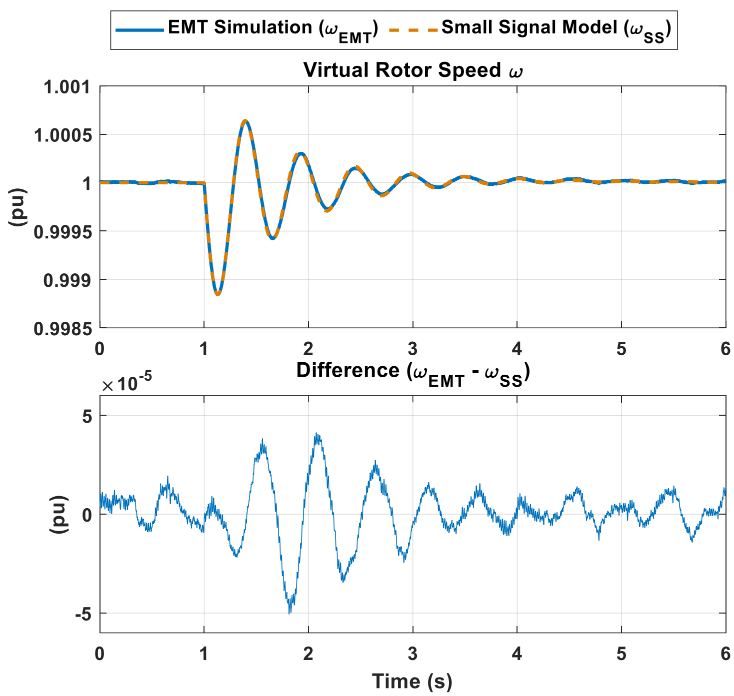

Figure 6-6 Comparison of the SS Model and EMT Simulation (3.2 VSG)

From the figure, the traces are essentially overlapping and the maximum absolute error of these two curves is $5.052 \times 10^{-5}\ pu$ (as shown in Figure 6-6 (b)) which corresponds to $0.0051\ \%$ of the nominal value of ω_{EMT}. Thus, the accuracy of the small signal model derived earlier is confirmed.

The plot of speed ω has an oscillatory component close to $1.91\,Hz$ and an attenuation constant close to $0.78\,s$. The curves show that the proposed control method is stable at the operating point and the speed ω recovers to $1.0\,pu$. This means the MMC synchronizes with the external ac system after the small disturbance.

6.1.2 Small Signal Models with Other Numbers of Windings

As mentioned previously in Section 5.2.1, different VSGs can be generated if a different number of dq-axes windings are used in the model. Developed for completeness, the models for the '2.1' VSG option (i.e., it has two windings in the d-axis and one in the q-axis) are presented below, as well as the '3.3' VSG option. Detailed equations are given in the Appendix I.

6.1.2.1 Small Signal Model of '2.1' VSG

An even simpler representation of the SM emulation VSG is to remove all damper windings, giving a '2.1' VSG representation as shown in Figure 6-7. The parameters are given in Table 6-4.

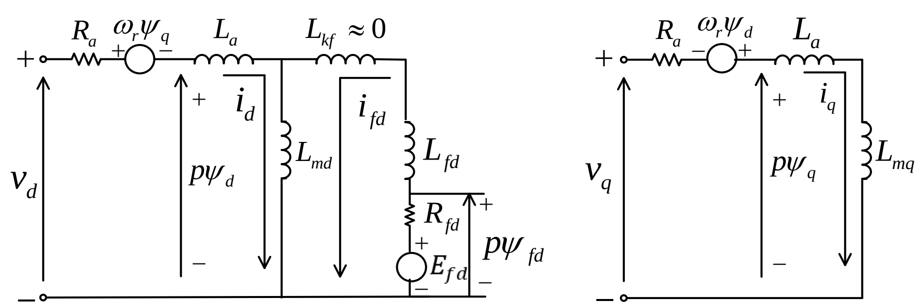

(a) *d*-axis equivalent circuit (b) *q*-axis equivalent circuit

Figure 6-7 D- and Q-axis Equivalent Circuits of '2.1' VSG

Table 6-4 Main '2.1' VSG Control Parameters

Parameter	Value	Parameter	Value
Inertia constant H	3.42 s	Leakage inductance L_a	0.015 pu
Damping constant D_w	5.0	d-axis mutual inductance L_{md}	2.0 pu
Stator resistance R_a	0.0043 pu	field winding inductance L_{fd}	0.119 pu
field winding resistance R_{fd}	0.0008947pu	q-axis mutual inductance L_{mq}	1.44pu

This VSG option only has the magnetizing branch and field winding in the d-axis and the magnetizing branch in the q-axis. Thus, this ‘2.1’ VSG control is more simplified than the ‘3.2’ options above. However, it still retains some details of the machine’s electric circuit in comparison to the Swing Equation-based representation discussed in Chapter 2.

Again, as was done in Section 6.1.2, the small signal model of this ‘2.1’ VSG option as shown in (6-50) can be easily obtained by removing all the differential equations pertaining to the damper windings from the ‘3.3’VSG model.

$$\frac{d\boldsymbol{\Delta x_{21}}}{dt} = \boldsymbol{A_{21}\Delta x_{21}} + \boldsymbol{B_{21}\Delta u} \tag{6-50}$$

The SS equations and matrix elements are summarized in the Appendix I.

Here, the eigenvalues of the ‘A_{32}’ (parameters in Section 6.1.1.6) and ‘A_{21}’ matrix (parameters in Table 6-4) as well as their corresponding oscillation frequencies and damping ratios are calculated in Table 6-5 below.

The results show that all the eigenvalues of the system have a negative real part. This fact indicates the stability of the system. Even with the simplification, the dominant oscillatory modes (i.e., those with non-zero imaginary parts), $\lambda_{1,2}$, $\lambda_{3,4}$, $\lambda_{5,6}$ still remain in the system. But the damping ratio is reduced, as is to be expected by the elimination of the damper windings.

Table 6-5 Eigenvalues of ‘3.2’ and ‘2.1’ SM Emulation VSG

Mode	‘3.2 SM Emulation VSG			‘2.1’ SM Emulation VSG		
	Eigenvalue	Oscillation frequency	Damping ratio, ξ	Eigenvalue	Oscillation frequency	Damping ratio, ξ
$\lambda_{1,2}$	$-25.35 \pm j996.44$	158.59 Hz	0.025	$-7.67 \pm j670.73$	106.75 Hz	0.011
$\lambda_{3,4}$	$-1.32 \pm j12.01$	1.91 Hz	0.109	$-0.96 \pm j11.36$	1.81 Hz	0.085
$\lambda_{5,6}$	$-0.58 \pm j0.76$	0.12 Hz	0.605	$-0.60 \pm j0.80$	0.13 Hz	0.605
λ_7	-66.96	-	1.0	-69.69	-	1.0
λ_8	-52.17	-	1.0	-45.70	-	1.0
λ_9	-33.36	-	1.0	-	-	-
λ_{10}	-6.52	-	1.0	-	-	-

6.1.2.2 Small Signal Model of '3.3' VSG

The small signal model of the most detailed SM emulation VSG (3.3 VSG in Chapter 5) is given in this section as a reference. However, since the '3.2' and '2.1' VSG options are sufficient to demonstrate the influence of the damper windings, this '3.3' model is not used for eigenvalue analysis in this chapter.

Figure 6-8 shows the equivalent circuits of the '3.3' VSG, which is identical to Figure 5-3 introduced earlier. It is repeated here for the reader's convenience. From the figure, this VSG option has three parallel windings in the d-axis consisting of the magnetizing branch (L_{md}), field inductance (L_{fd}) and damper winding inductance (L_{1d}), and correspondingly three parallel windings in the q-axis (L_{mq}, L_{1q}, L_{2q}). The subscript '*33*' is used in this section.

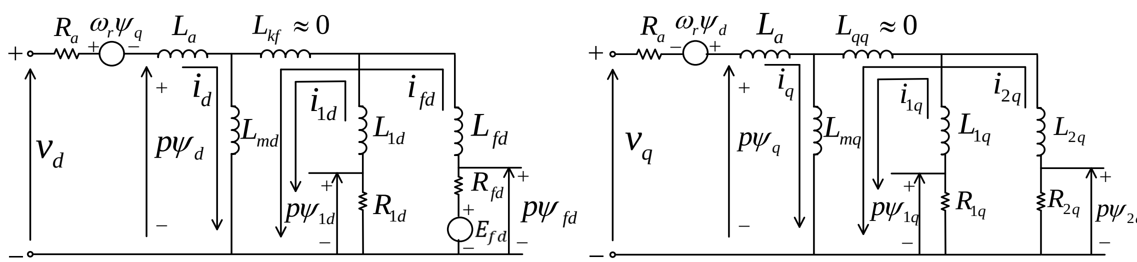

Figure 6-8 D- and q-axis Equivalent Circuits of '3.3' VSG

Because of the similar structure with the '3.2' VSG option in the former section, the small signal model of this '3.3' VSG option can be easily obtained by adding the differential equation corresponding to one of the q-axis damper windings (L_{2q}) from the '3.2'VSG model, which is shown in (6-51).

$$\frac{d\boldsymbol{\Delta x_{33}}}{dt} = \boldsymbol{A_{33}\Delta x_{33}} + \boldsymbol{B_{33}\Delta u} \tag{6-51}$$

The SS equations and matrices are summarized in the Appendix I.

6.2 Impact of System Strength on Stability and Transient Behaviour of SM Emulation VSG

Root locus analysis is conducted in this section to investigate how the SCR affects the stability and transient behaviour of the proposed VSGs. In the forthcoming examples, an operating point of unity output power, i.e., $P_t = 1.0\,pu$, is used as the operating point in linearizing the SS models presented in the previous section.

The eigenvalues of the matrix A_{32} as given in (6-49) correspond to the '3.2' VSG's small signal model with damper windings and eigenvalues of A_{21} given in (A-10) are those for the more simplified representation with no damper windings. Matrices A_{32} and A_{21} are functions of the ac system reactance X_s which is inversely proportional to the SCR. The root loci of matrices A_{32} and A_{21} for varying SCR can be plotted in the complex plane by varying X_s, from which the damping and the stability information can be garnered. In this section, only the most critical eigenvalues close to the imaginary axis are plotted in the root loci. The test system is the same as in Figure 6-5.

Figure 6-9 (a) and (b) respectively show the plot of the critical eigenvalues of A_{32} (×) and A_{21} (○), as the SCR varies from $SCR = 1.2$ for a weak system to $SCR = 100$ for an ultra-stiff system. Other non-varying parameters are given in Table 6-1 to Table 6-4. As the eigenvalues have negative real parts, both VSG options exhibit stable operation over the entire SCR range.

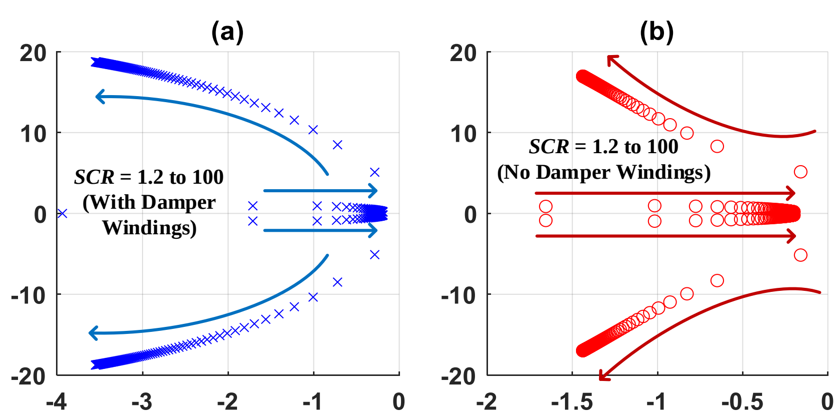

Figure 6-9 Eigenvalue Loci with SCR Ranging From 1.2 to 100.0. (a) '3.2' VSG (b) '2.1'VSG.

In comparison, the conventional voltage source interfaced VSG with an embedded current controller (mentioned in Section 2.2.1) connected to the same ac network (Figure 6-5) may become unstable with a high SCR ac system [69] [28]. Figure 6-10 shows the root loci of the A matrix of this type of VSG under varying SCR. The underlying SS equations for this case are taken from [28], and listed in the Appendix II.

From Figure 6-10, the eigenvalues move to the right-hand side of the imaginary-axis when the SCR is larger than 3.9 in this case, which indicates the system becomes unstable if $SCR > 3.9$. This instability is attributable to the delays inherent in the proportional-integral (PI) controllers of the embedded current controller. In contrast, the proposed SM emulation VSG uses a hysteresis current controller to generate the current which is extremely rapid with minimal delay.

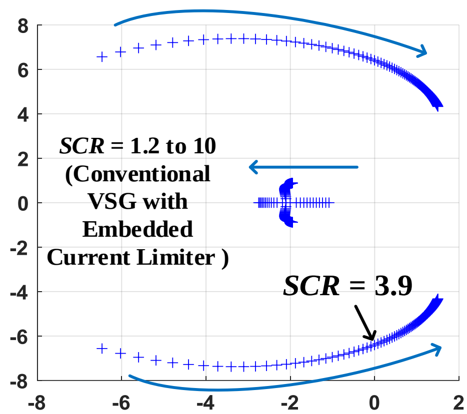

Figure 6-10 Eigenvalue Loci of Conventional VSG with SCR Ranging From 1.2 to 10.0

Additionally, from Figure 6-9, an increase in the SCR for the SM emulation VSG leads to a shift of the oscillatory eigenvalues to the left, which indicates an improvement in the damping of oscillations. Also, there is an increase in the oscillation frequency (f_n) with a larger SCR.

EMT simulation validates the above eigenvalue analysis results. Figure 6-11 shows the responses of '3.2' SM emulation VSG following a step change in active power reference from $1.0\,pu$ to $0.9\,pu$. The lowest SCR value is seen to have the smallest damping ratio and the smallest oscillation frequency compared to the others.

The oscillation frequencies (f_n) and damping ratios (ξ) calculated from the SS model and measured from the EMT simulation are listed in Table 6-6 below. The values given from the EMT simulation generally follow the trend in the SS model (maximum difference of 9.87 % in the oscillation frequency and 7.14 % in the damping ratio).

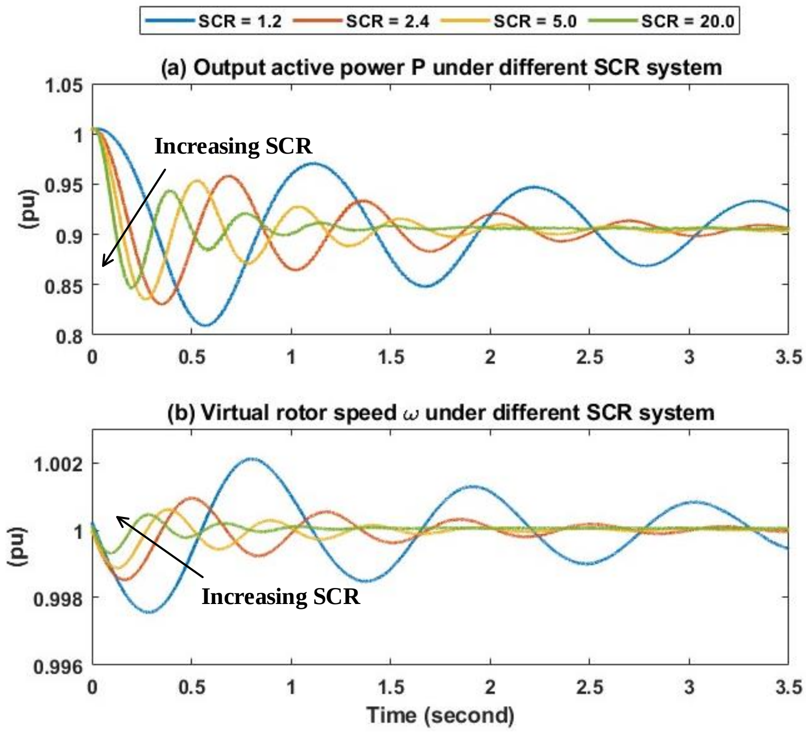

Figure 6-11 Step Responses of '3.2' SM Emulation VSG with Different SCR Ac Systems

Table 6-6 Oscillation Frequency and Damping Ratio of '3.2' VSG with Different SCR

SCR value	Mode	Oscillation frequency, f_n	Damping ratio, ξ
$SCR = 1.2$	SS Model	0.81 Hz	0.056
	EMT	0.89 Hz	0.060
$SCR = 2.4$	SS Model	1.49 Hz	0.090
	EMT	1.48 Hz	0.096
$SCR = 5.0$	SS Model	1.98 Hz	0.113
	EMT	1.99 Hz	0.110
$SCR = 20.0$	SS Model	2.65 Hz	0.155
	EMT	2.60 Hz	0.155

Similar conclusions can also be drawn from the transient waveforms of the '2.1' SM emulation VSG with no damper windings, which is omitted here for brevity.

6.3 Impact of Damper Winding Parameters on Stability and Transient Behaviour of SM Emulation VSG

Note that, unlike the real SG, the available winding parameters of the proposed VSG are not restricted to the range of a physical machine, and it is free to arbitrarily assign any parameter value that we may wish to. With this in mind, root locus analysis is conducted on the small signal model for the operating point of $P_t = 1.0\,pu$ to analyze how the damper windings parameters (R_{1d}, L_{1d}, R_{1q}, L_{1q}) affect the stability and transient behaviour of the proposed VSG.

The eigenvalues of the more detailed VSG A_{32} are given in (6-49) and the simpler version A_{21} are given in (A-10) of the Appendix I. They can be plotted in the complex plane as a function of the varying damper winding parameter (e.g., R_{1d}, L_{1d} , etc.) to generate a root locus plot from which the damping and stability information can be acquired. The eigenvalues of A_{32} and A_{21} are denoted by '×' and '○' respectively. Note that as the '2.1' VSG has no damper winding, the eigenvalues of A_{21} remain stationary. The test system is same Figure 6-5, and the non-varying parameters are given in Table 6-1 to Table 6-4. Only the most critical eigenvalues close to the imaginary axis are plotted in the root loci.

6.3.1 Root Locus with Varying D-axis Damper Resistance R_{1d}

Figure 6-12 shows the plot of the eigenvalues of A_{32} (×) and A_{21}(○) as the d-axis damper resistance R_{1d} changes from $0.0\,pu$ to $1.0\,pu$. As mentioned earlier, the eigenvalues of plotted for comparison do not move due to there being no damper winding.

From Figure 6-12, the eigenvalues of A_{21} and A_{32} are all in the left-hand plane, which indicates stable operation over the entire range of R_{1d}. Also, the eigenvalues of A_{32} (×) move asymptotically towards the eigenvalues of A_{21} (○) as R_{1d} increases. It is to be expected as having no damper winding is tantamount to having a damper winding with $R_{1d} = \infty$.

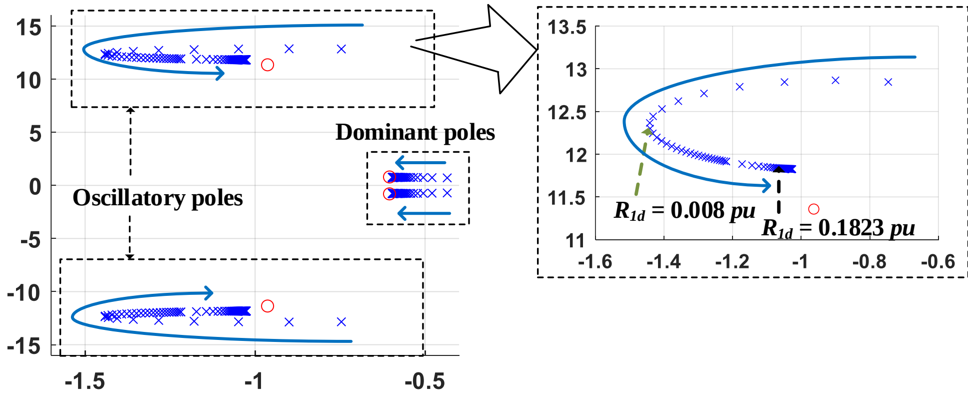

Figure 6-12 Eigenvalue Loci of '3.2' (×) and '2.1'VSG (○) with Increasing R_{1d}

One of the oscillatory eigenvalues is zoomed in and is shown on the right-hand frame in Figure 6-12. The oscillation frequency of the '3.2' VSG with different R_{1d} changes in a small range between $1.87\,Hz$ to $2.04\,Hz$. Moreover, the '2.1' VSG with no damper windings has the least damping ratio of 0.085 for the dominant oscillatory mode. While with the damper winding, the real part of the oscillatory eigenvalues first increases with increasing R_{1d}, attains a maximum for $R_{1d} = 0.008\,pu$ and then decreases. Thus, in this example, the largest damping ratio of 0.116 occurs for $R_{1d} = 0.008\,pu$. Hence, including the damper windings in the VSG does improve the damping ratio from 0.085 to 0.116 so that the transient response settles down faster.

The above conclusions can be validated using a time domain simulation. Figure 6-13 shows step responses with $\Delta P_{ref} = -0.1\,pu$ for three cases: i) '2.1' VSG with no damper winding, ii) '3.2' VSG with $R_{1d} = 0.008\,pu$, and iii) '3.2' VSG with $R_{1d} = 0.1823\,pu$.

As expected, the damping ratio of the oscillatory mode is the largest for $R_{1d} = 0.008\,pu$ ($\xi = 0.120$) while it is the least ($\xi = 0.086$) for the controller without any damper windings. Also, comparing the oscillation frequency we find that $f_{n2} = 1.92\,Hz$ for $R_{1d} = 0.008\,pu$, $f_{n3} = 1.84\,Hz$ for $R_{1d} = 0.1823\,pu$ and $f_{n1} = 1.80\,Hz$ for the no damping case, i.e., $f_{n1} < f_{n3} < f_{n2}$. Hence, the EMT simulation results indeed match the conclusion of the eigenvalue analysis.

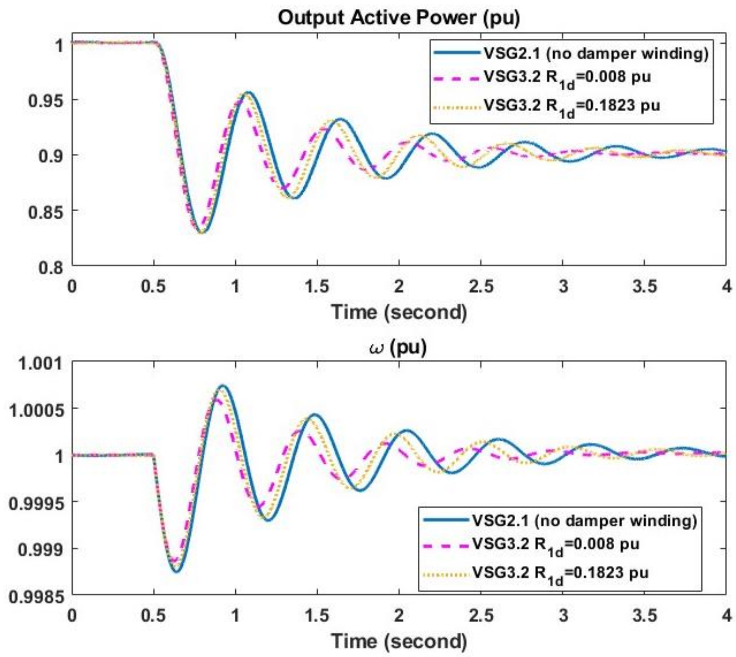

Figure 6-13 Step Responses of VSG with Different R_{1d}

Table 6-7 shows the oscillation frequencies (f_n) and damping ratios (ξ) calculated from the SS model and measured from the EMT simulation. There is good agreement with the values obtained from the SS analysis and EMT simulation (maximum difference of 2.5 % in the oscillation frequency and 3.4 % in damping ratio).

Table 6-7 Oscillation Frequency and Damping Ratio of VSG with Different R_{1d}

R_{1d} value	Mode	Oscillation frequency, f_n	Damping ratio, ξ
$R_{1d} = 0.008\ pu$	SS Model	1.97 Hz	0.116
	EMT	1.92 Hz	0.120
$R_{1d} = 0.1823\ pu$	SS Model	1.88 Hz	0.089
	EMT	1.84 Hz	0.092
Without damper windings	SS Model	1.81 Hz	0.085
	EMT	1.80 Hz	0.086

6.3.2 Root Locus with Varying D-axis Damper Inductance L_{1d}

Figure 6-14 shows the plot of the eigenvalues of A_{32} ($\times$), as the d-axis damper inductance L_{1d} changes from $0.0\ pu$ to $10.0\ pu$. One of the dominant poles is zoomed in and shown on the right. The eigenvalues of A_{21} (○) are also plotted and remain stationary as the formulation of A_{21} does not include L_{1d}.

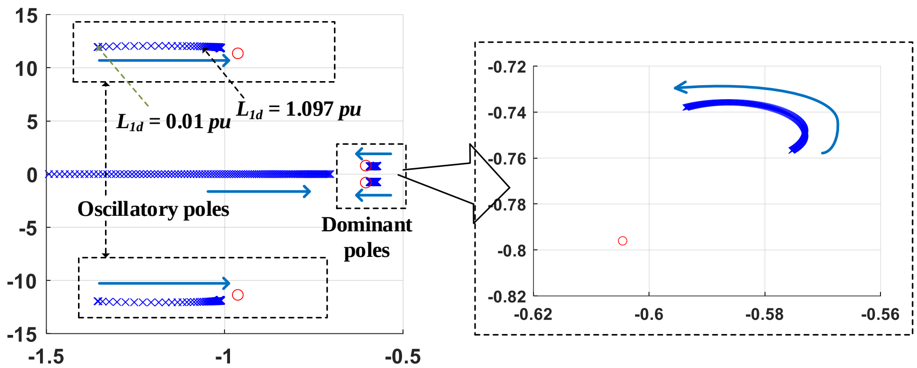

Figure 6-14 Eigenvalue Loci of '3.2' (×) and '2.1'VSG (○) with Increasing L_{1d}

From Figure 6-14, the following conclusions can be obtained:

1. Observation of the dominant poles shows that the operation is stable over the entire range of L_{1d}.
2. The dominant poles of '3.2' VSG first move closer to the imaginary axis and then turn back away from the imaginary axis. Therefore, the worst operation situation of the system stability happens at the furthest right of the root locus, which L_{1d} is around $2.5\,pu$ in this example.
3. The eigenvalues of A_{32} (×) move asymptotically towards the eigenvalues of A_{21} (○) as L_{1d} increases, which is to be expected as having no damper winding is tantamount to having a damper winding with $L_{1d} = \infty$.
4. From the oscillatory poles, the '2.1' VSG without damper windings has the least damping ratio (ξ) which is 0.085. For '3.2' VSG with damper windings, a smaller L_{1d} gives better damping, for example, $\xi = 0.113$ for $L_{1d} = 0.01\,pu$. Hence, the inclusion of the damper windings improves the damping ratio from 0.085 to 0.113.
5. The oscillation frequency is unchanged at around $1.90\,Hz$ with varying L_{1d}.

Figure 6-15 shows the step responses with $\Delta P_{ref} = -0.1\,pu$ for three cases to validate the above root locus analysis, viz. i) '2.1' VSG with no damper winding, ii) '3.2' VSG with $L_{1d} = 0.01\,pu$, and iii) '3.2' VSG with $L_{1d} = 1.097\,pu$.

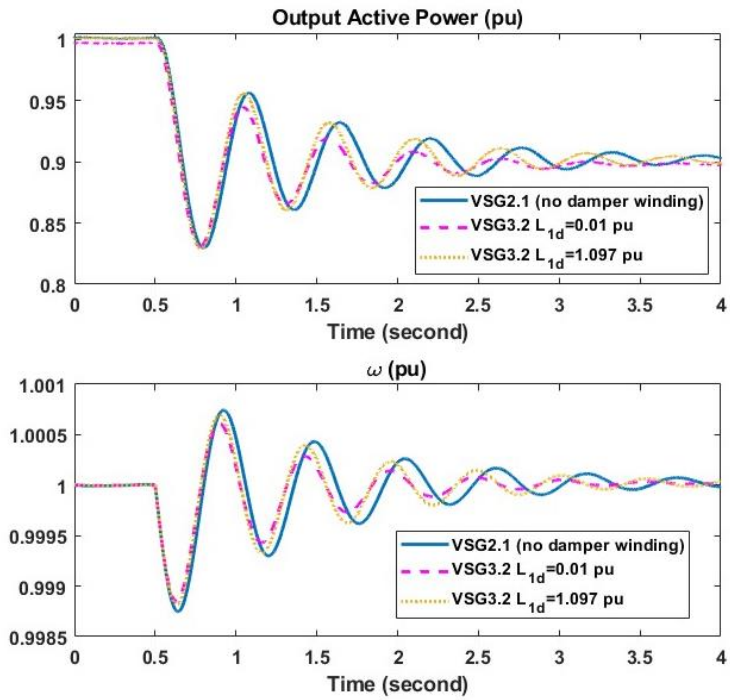

Figure 6-15 Step Responses of VSG with Different L_{1d}

Table 6-8 shows the oscillation frequencies (f_n) and damping ratios (ξ) calculated from the SS model and measured from the EMT simulation. The results obtained from the SS analysis and EMT simulation match well, with a maximum difference occurring for the $L_{1d} = 0.01\,pu$ case, of $1.1\,\%$ in the oscillation frequency and $4.4\,\%$ in the damping ratio.

Table 6-8 Oscillation Frequency and Damping Ratio of VSG with Different L_{1d}

L_{1d} value	Mode	Oscillation frequency, f_n	Damping ratio, ξ
$L_{1d} = 0.01\,pu$	SS Model	1.90 Hz	0.113
	EMT	1.88 Hz	0.118
$L_{1d} = 1.097\,pu$	SS Model	1.90 Hz	0.087
	EMT	1.88 Hz	0.090
Without damper windings	SS Model	1.81 Hz	0.085
	EMT	1.80 Hz	0.086

6.3.3 Root Locus with Varying Q-axis Damper Winding Parameters (R_{1q} and L_{1q})

The root loci (Figure 6-16) obtained by varying the q-axis damper resistance and inductance (R_{1q} and L_{1q}) are qualitatively similar to those with varying R_{1d} and L_{1d}. Similar to the case with R_{1d}, the real part of the oscillatory eigenvalues first increases with increasing R_{1q}, attains a maximum damping ratio of $\xi = 0.121$ for $R_{1q} = 0.028\,pu$ and then decreases. Additionally, a smaller L_{1q} gives better damping, for example, $\xi = 0.143$ for $L_{1q} = 0.01\,pu$. Hence, including the q-axis damper windings in the VSG also improves the damping ratio.

Table 6-9 shows the oscillation frequencies (f_n) and damping ratios (ξ) calculated from the SS model and measured from the EMT simulation (waveforms are not shown), which show good agreement (maximum difference of $2.1\,\%$ in the oscillation frequency and $2.8\,\%$ in the damping ratio).

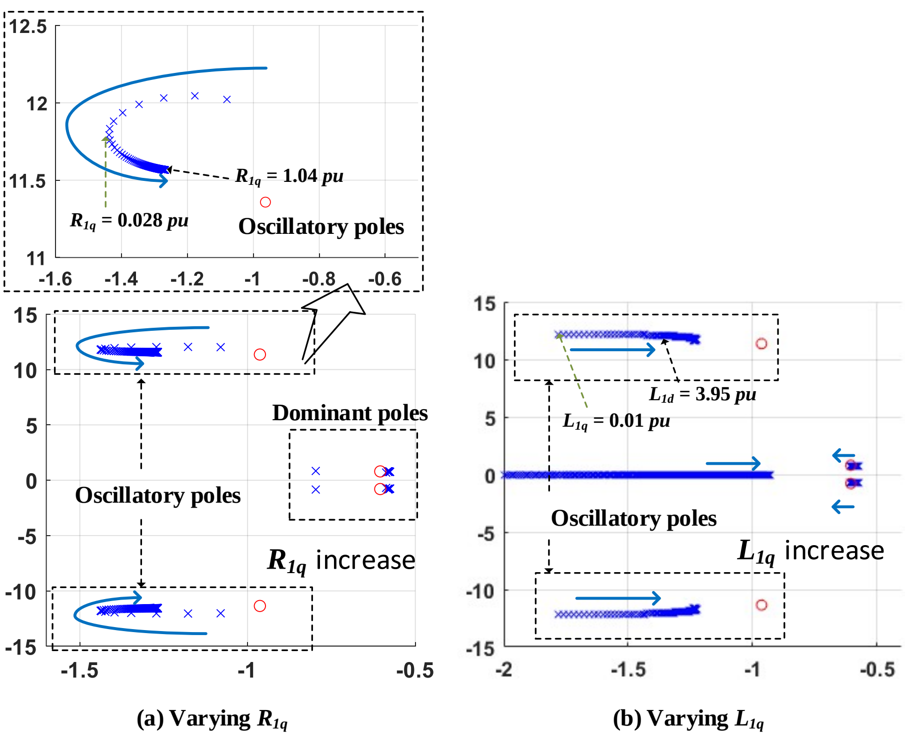

Figure 6-16 Eigenvalue Loci of '3.2' (×) and '2.1'VSG (○) (a) with Increasing R_{1q} and (b) with Increasing L_{1q}

Table 6-9 Oscillation Frequency and Damping Ratio of VSG with Different R_{1q} and L_{1q}

R_{1q}, L_{1q} value	Mode	Oscillation frequency, f_n	Damping ratio, ξ
Without damper windings	SS Model	1.81 Hz	0.085
	EMT	1.80 Hz	0.086
$R_{1q} = 0.028\ pu$	SS Model	1.87 Hz	0.121
	EMT	1.84 Hz	0.123
$R_{1q} = 1.04\ pu$	SS Model	1.84 Hz	0.109
	EMT	1.81 Hz	0.112
$L_{1q} = 0.01\ pu$	SS Model	1.94 Hz	0.143
	EMT	1.90 Hz	0.145
$L_{1q} = 3.95\ pu$	SS Model	1.81 Hz	0.106
	EMT	1.82 Hz	0.109

6.4 Improving Damping Ratio using Parameter Optimization

As mentioned before, the available parameters of the proposed VSG are not restricted to the range of a physical machine, and one is free to arbitrarily assign any parameter value that one may wish to. Therefore, it is possible to improve the performance of the VSG by optimizing its parameters using an optimization algorithm, e.g., particle swarm optimization (PSO) [70], genetic algorithm (GA) [71], and so on. This chapter will show how the damping performance can be drastically improved by using such optimized parameters. The popular Genetic Algorithm (GA) is selected in this thesis because it is effective and highly customizable, allowing for the incorporation of different constraints and objectives [72]. Additionally, unlike some other optimization methods which may get stuck in a local optimum (i.e., the best possible solutions), GA can converge to the global optimum of a problem [73].

Note that this thesis does not aim to explore different optimization methods, but rather, the intention is to use optimization to achieve an objective. Hence, because GA worked very well, no comparative studies with other optimization methods were deemed necessary.

6.4.1 Background of Genetic Algorithm

In this section, the optimization of the VSG parameters is accomplished by using a Genetic Algorithm (GA) as shown in Figure 6-17 [71]. GA is a heuristic bio-inspired optimization technique, which is developed based on the concept of evolution from Charles Darwin. The main idea is to emulate the evolution of individuals in a population, under a certain environment, aiming to improve their performance over the generations.

The performance is evaluated by using an objective or fitness function $f(x)$ of the parameter x to be selected for optimized behaviour. In this way, the individuals with higher fitness will have a higher probability of reproduction (crossover) and transmit part of their genetic code to their offspring. In this sense, the offspring will have a random proportion of the genetic code of each one of the progenitors. However, in nature it is also possible to have random mutations, caused naturally, by a disease, or any external factor, generating modifications in any gene.

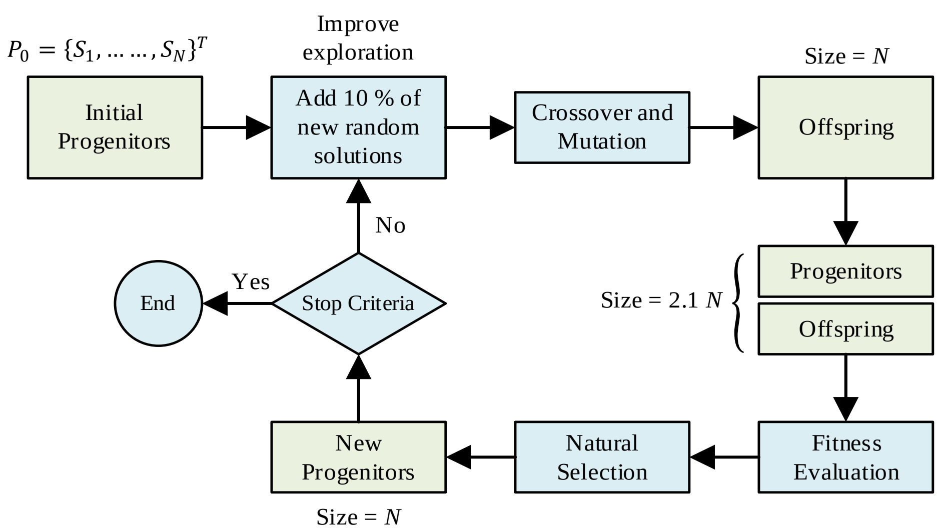

Figure 6-17 Flowchart of the Genetic Algorithm

During the lifetime of each individual, a high fitness level improves the probability of reproduction, and also its survival capacity in a certain environment. In this way, the conditions of the environment can naturally eliminate any of the individuals in the population. This process of selection and elimination of individuals is called natural selection. In nature, an individual can't survive in all generations (e.g., forever). However, in GAs this is possible to achieve, depending on the natural selection operator used. This brings the advantage of maintaining the best solutions, but also decreases the diversity of the population, making it difficult to have individuals that find different ways to solve the problem. Maintaining diversity is especially important if the environment is dynamic, i.e., if it is changing from time to time.

In GAs, the individuals are represented as chromosomes. Classically, they are represented in a binary form. However, they can also be represented by integer, real, or permutation variables. In the specific case of this thesis, the individuals/solutions are represented by 12 real VSG parameters. The set S of all possible solutions can be described as $S \in \{H, D_w, R_a, R_{fd}, R_{1d}, R_{1q}, L_a, L_{md}, L_{fd}, L_{1d}, L_{mq}, L_{1q}\}$. The entries H, D_w, etc., are defined in Table 6-10 below.

The performance of the solution is evaluated through the objective/fitness function. It is well known that eigenvalues of A matrix of the small signal model represent the characteristic of the system at a specific operating point. Also, with a larger damping ratio, the system has a better performance with a shorter settling time. Thus, the GA optimization can be performed to select parameters of '3.2' VSG using an objective function as given in (6-52) below to obtain the largest damping ratios.

$$\begin{cases} max\ f_1 = min\left(\frac{\sigma_n}{\sqrt{\sigma_n^2+\omega_n^2}}\right) \\ n \in \{1, 2, 3, \ldots, 10\} \end{cases} \tag{6-52}$$

In (6-52), $\lambda_n = \sigma_n + j\omega_n$ represents the n^{th} eigenvalues of the A_{32} matrix under the specific operating point ($P_t = 1.0\,pu$), so that the calculated damping ratio is $\frac{\sigma_n}{\sqrt{\sigma_n^2+\omega_n^2}}$ .The aim of the objective function is to maximize the smallest damping ratio.

The GA searches over the parameter space to find the parameters that maximize the objective function. However, any eigenvalues that move into the right-hand plane are given penalized. This forces the solution to consider only stable eigenvalues as potential candidates. Another constraint is that the VSG parameters be positive to maintain the character of an SG. Mathematically, this penalization is represented in (6-53) [74]. In (6-53), c is the constraint, C is the set of constraints, Cv_c is the value of a constraint c and Cl_c is the limit of the constraint c.

$$P = -\sum_{c \in C} \begin{cases} \left(\frac{Cl_c - Cv_c}{Cl_c}\right) & \text{if } Cv_c > Cl_c \\ |Cv_c| \times 100 & \text{if } Cl_c = 0 \\ 0 & \text{otherwise} \end{cases} \tag{6-53}$$

The GA operators used to solve this problem are described below:

1) Crossover: It is assumed that a pair of progenitors will produce two offspring. The value of each gene in each offspring follows (6-54). In this section, the probability of crossover selected for the problem is $90\ \%$.

$$\begin{cases} o_{1i} = \alpha p_{1i} + (1-\alpha) p_{2i} \\ o_{2i} = \alpha p_{2i} + (1-\alpha) p_{1i} \end{cases} \tag{6-54}$$

In (6-54), α is a random number between 0 and 1, p is the progenitor, o is the offspring, and i is the decision variable.

2) Mutation: It is described by (6-54). There, x is the original variable, x' is the variable after mutation, $m()$ is the mutation function, $N(0{,}1)$ is a random number between 0 and 1, and $d = 0.1$. In this section, the probability of mutation selected for the problem is $15\ \%$.

$$x' = m(x) = x + d \times N(0{,}1) \tag{6-54}$$

3) Natural selection: It is performed by a modified tournament. To explain this modified tournament process more clearly, a specific example is shown in Figure 6-18.

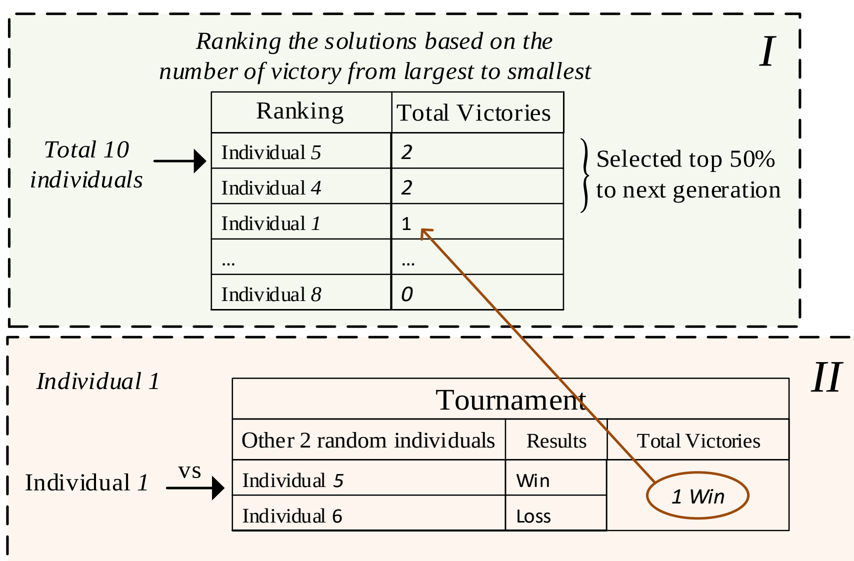

Figure 6-18 Natural Selection Based on Tournament.

In this example, the total number of individuals (N) is 10, and each individual competes with two other random individuals ($k = 2$). For example, the tournament process of individual *1* is shown in Region *II,* where individuals *5* and *6* are randomly chosen to join the competitions. This tournament process is repeated for all 10 individuals. In each tournament, the quantity of victories of each individual is quantified and then ranked based on these victories' numbers from largest to smallest, which is shown in Region *I*. Then, the individuals with the best ranking (top $50\ \%$) will survive.

In this section, a total group of $20\ \%$ of the individuals ($k = 20\ \% \times N$) in the population is selected to join the tournaments, and the top $50\ \%$ of individuals are selected for the next generation.

6.4.2 Optimization of Rated Operating Point at Unity Output Power

In this section, GA optimization is carried out to select parameters of '3.2' VSG using an objective function as given in (6-52) above to obtain the largest damping ratios while operating at the nominal operating point of $P_t = 1.0\ pu$. Table 6-10 shows the parameters of the '3.2' VSG after optimization as well as the percentage by which they are different from the original values (typical for a real SG). The optimization results show that in order to maximize the damping ratio of the '3.2' VSG, the values of 'virtual' resistance parameters change dramatically compared with other parameters by factors ranging from $226\ \%$ to $5023\ \%$.

With these optimized parameters, Figure 6-19 (a) shows the step responses with $\Delta P_{ref} = -0.1\ pu$ of the SS model as well as the EMT simulation. Figure 6-19 (b) is the case with the original parameters, which is the same as Figure 6-6. Also, the eigenvalues of the SS model with optimized parameters and their damping ratios as well as oscillation frequencies are given in Table 6-11.

The transient response of (a) has significantly better performance compared with the results in (b). With the optimization, the damping ratio increases almost seven-fold from 0.109 (in Table 6-5) to 0.707 (in Table 6-11). Also, the settling time ($t_s = 0.657\ s$) of Figure 6-19 (a) is much shorter than that of $t_s = 1.699\ s$ in Figure 6-19 (b). Note that although the optimization was conducted using the small signal model, the waveforms from

EMT simulation and SS model essentially overlap as can be seen in Figure 6-19, showing an excellent agreement.

Table 6-10 Optimized Parameters of '3.2' VSG for Specific Operating Point of $P_t = 1.0\ pu$

Parameter	Original Value	Optimized Value	Changing Percentage
Inertia constant H	3.42 s	3.0597 s	-10.54 %
Damping constant D_w	5.0	5.2988	5.98 %
Stator resistance R_a	0.0043 pu	0.04439 pu	932.33 %
d-axis damper resistance R_{1d}	0.01823 pu	0.05944 pu	226.06 %
field winding resistance R_{fd}	0.0008947pu	0.00693 pu	672.53 %
q-axis damper resistance R_{1q}	0.0104 pu	0.53288 pu	5023.80 %
Leakage inductance L_a	0.015 pu	0.01545 pu	3.00 %
d-axis mutual inductance L_{md}	2.0 pu	2.70179 pu	35.09 %
field winding inductance L_{fd}	0.119 pu	0.02788 pu	-76.57 %
d-axis damper inductance L_{1d}	0.1097 pu	0.07640 pu	-30.36 %
q-axis mutual inductance L_{mq}	1.44 pu	1.99778 pu	38.73 %
q-axis damper inductance L_{1q}	0.395 pu	0.05247 pu	-86.72 %

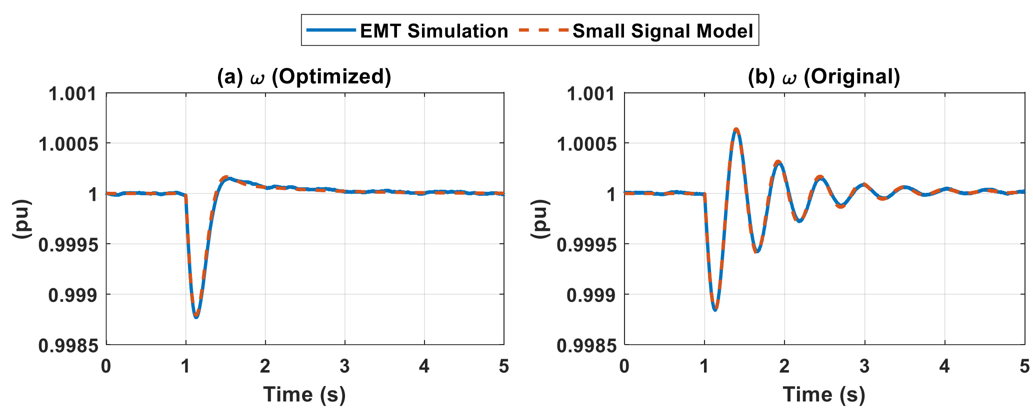

Figure 6-19 Virtual Rotor Speed ω with (a) Optimized Parameters (b) Original Parameters

It can be concluded that removing the physical constraints on the VSG parameters allows one to discover the parameters that give significantly superior performance. These can be obtained by a process of non-linear optimization. However, the optimization was carried out for a specific operating point, so the robustness of this method needs to be studied to investigate whether the tuning parameters are still suitable for other operating points. This issue is addressed in the next section by modifying the objective function to consider multiple operating points of the MMC.

Table 6-11 Eigenvalues of '3.2' VSG with Parameters Optimized at $P_t = 1\ pu$ (Rated Power)

Mode	Eigenvalue	Oscillation frequency	Damping ratio, ξ
$\lambda_{1,2}$	$-1405.5 \pm j1253.7$	$199.54\ Hz$	0.746
$\lambda_{3,4}$	$-14.94 \pm j8.48$	$1.34\ Hz$	0.869
$\lambda_{5,6}$	$-8.26 \pm j8.26$	$1.31\ Hz$	0.707
λ_7	-946.9	-	1.0
λ_8	-244.4	-	1.0
λ_9	-80.34	-	1.0
λ_{10}	-1.07	-	1.0

6.4.3 Optimization of Multiple Operating Points

To consider a robust optimization which is valid over the projected operating range, multiple operating points must be considered [75]. The objective function of the optimization is modified using the weighted sum approach as given in (6-55) below.

$$\begin{cases} max\ f_2 = \sum_{m=1}^{3} \kappa_m \cdot min\left(\frac{\sigma_{m.n}}{\sqrt{\sigma_{m,n}^2 + \omega_{m,n}^2}}\right) \\ n \in \{1, 2, 3, \dots, 10\} \\ \kappa_m \in \left\{\frac{1}{3}, \frac{1}{3}, \frac{1}{3}\right\} \\ P_m \in \{0.5, 0.7, 1.0\} \end{cases} \tag{6-55}$$

In (6-55), the index m represents each operating point and $\lambda_{m,n} = \sigma_{m,n} + j\omega_{m,n}$ is the n^{th} eigenvalues of the small signal model for operating point m. Typical operating points considered in the example are $P_1 = 0.5\ pu$, $P_2 = 0.7\ pu$ and $P_3 = 1.0\ pu$. By using the sum of the normalized objectives multiplied by a weight vector, the multiple objectives can be transformed into a single one.

With this new objective function, the GA method generates a more robust set of parameters that give an overall optimized response over a range of operating points, although the operation at the individual operating points may be sub-optimal. Table 6-12 shows the parameters of the '3.2' VSG after the robust optimization which considers multiple operating points. With these new optimized parameters in Table 6-12, Figure 6-20 (a) show the step responses with $\Delta P_{ref} = -0.1\,pu$ of the SS model as well as the EMT simulation for two different operating cases $P_t = 1.0\,pu$ and $P_t = 0.1\,pu$. For comparison, Figure 6-20 (b) is the step responses of VSG with the old parameters given in Table 6-10, which are optimized for only one operating point ($P_t = 1.0\,pu$).

Table 6-12 Parameters of '3.2' VSG with Robust Optimization Including Multiple Operating Points

Parameter	Optimized Value	Parameter	Optimized Value
Inertia constant H	3.3775 s	Leakage inductance L_a	0.00948 pu
Damping constant D_w	5.0998	d-axis mutual inductance L_{md}	1.98853 pu
Stator resistance R_a	0.10502 pu	field winding inductance L_{fd}	0.02473 pu
d-axis damper resistance R_{1d}	0.03396 pu	d-axis damper inductance L_{1d}	0.11581 pu
field winding resistance R_{fd}	0.00785 pu	q-axis mutual inductance L_{mq}	1.45503 pu
q-axis damper resistance R_{1q}	0.02917 pu	q-axis damper inductance L_{1q}	0.29485 pu

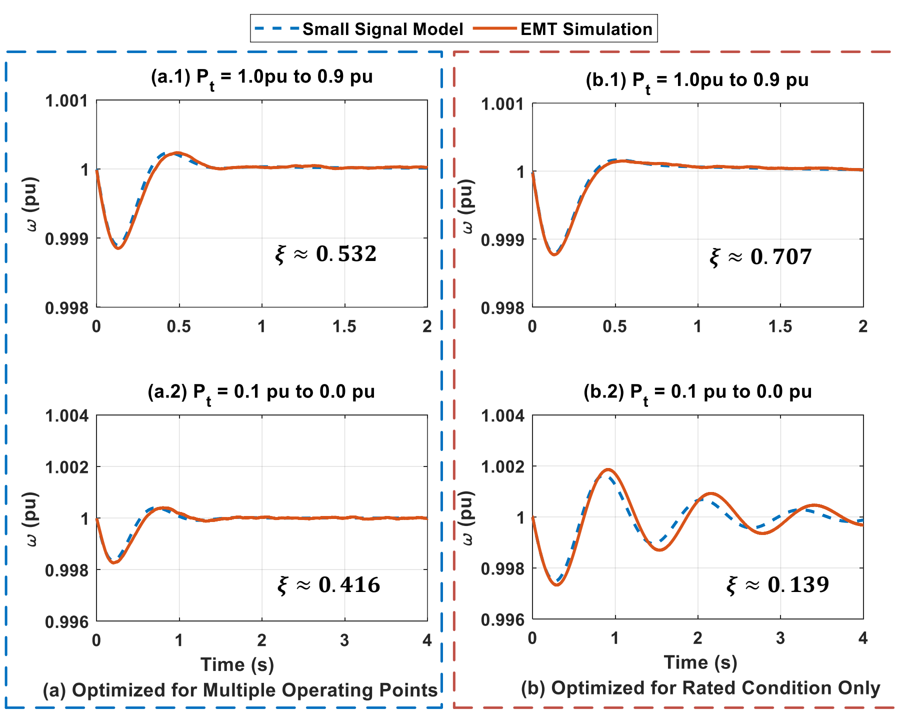

Figure 6-20 Response of Virtual Rotor Speed ω (a) With Parameters Optimized for Multiple Operating Points (b) With Parameters Optimized for Rated Condition Only.

From Figure 6-20 (a), when applying the VSG parameters after the robust optimization with the modified objective function that takes into account several operating points, both responses of the virtual rotor speed (ω) at $P_t = 1.0\,pu$ as well as at $P_t = 0.1\,pu$ are well damped with $\xi = 0.532$ and $\xi = 0.416$ respectively. However, the waveforms of ω with the parameters optimized only for a single operating point at rated power show different performances. From Figure 6-20 (b), although it is evident that the ω response is well damped for $P_t = 1.0\,pu$, with a damping ratio of $\xi = 0.707$, it becomes oscillatory for $P_t = 0.1\,pu$ with a poorer damping ratio of $\xi = 0.139$. This demonstrates the need for overall optimization across the envisaged operating point range.

It should be noticed, however, that robust optimization tries to ensure well-damped behaviour at several operating points. Hence, the response for a particular operating point may be sub-optimal. For example, the optimal performance for $P_t = 1.0\,pu$ gives $\xi = 0.7$, but drops to $\xi = 0.532$ when we sacrifice some performance in order to provide universally good damping within the expected operating range.

6.5 Chapter Conclusion

This chapter focuses on the eigenvalue analysis of the detailed SM emulation VSG. It shows how the damping and oscillatory behavior is affected by the level of detail of the model, and also allows one to judge whether the simplest 2.1 model is adequate or are higher order models are advisable.

1) The small signal modelling of detailed SM emulation VSG was developed for:
   - The ‘2.1’ model with a stator and a field winding on the d-axis and a stator winding on the q-axis (no damper windings).
   - The ‘3.2’ model with a stator, a field, and one damper windings on the d-axis as well as a stator winding and one damper winding on the q-axis.
2) The ‘3.2’and ‘2.1’ VSG options were tested for stability and oscillatory behaviour with different $SCRs$ for the connecting ac grid over ranging from weak ($SCR <$ 2) to ultra-stiff ($SCR > 30$). The analysis was conducted using root locus analysis which was validated using EMT simulation.

- The conventional voltage source interfaced VSG with an embedded current limiter can experience instability when operating into a strong ac system. The proposed detailed SM emulation VSG overcomes this drawback and works stably in both weak and strong ac systems.
- Additionally, an increase in the SCR for the SM emulation VSG indicates an improvement in the damping of oscillations. Also, there is an increase in the oscillation frequency (f_n) with a larger SCR.

3) Eigenvalue analysis was conducted on both '3.2' and '2.1' VSG to investigate the effect of inclusion/exclusion of the damper windings.
   - Including the damper windings in the VSG implementation increases the modelling complexity. Conversely, the simplified VSG without any damper winding is easier to implement and tune as it has a smaller number of parameters.
   - For a given ac system, the d- and q-axis damper winding impedances in the model can be optimized to provide maximum damping, and then transient performance can be improved.
   - Even with the simplification, the dominant oscillatory modes remain in the system, which is sufficient for the mimic of the dynamic response of an actual SG.
4) The VSG has more freedom for the selected parameter values which a real SG does not. Removing the physical restriction on the chosen parameters of the VSG allows one to optimize them for significantly improved performance. This chapter demonstrated that using a non-linear optimization algorithm (GA) to select the parameters of '3.2' VSG indeed significantly improves the damping.
   - With the optimization for a unity output power specifically, the maximum damping ratio of the example system is 0.707, which has a major increase compared with the previous case ($\xi = 0.109$).
   - The virtual winding resistances are most sensitive in controlling damping. The values of the optimized parameters were significantly different, some by as much as 50 times larger than those of a real SG.

- It was noticed that when the VSG parameters were optimized only for the rated operating point, the performance became poor at other operating points. This was corrected by conducting a ‘robust’ optimization, where the objective function was modified to be the weighted sum of the objective function of individual operating points.

7 Comparison of SE-based VSG and Detailed SM Emulation VSG

The material in this chapter 7 is published by the author as reference [76]: C. Jiang, A. D. Sinkar and A. M. Gole, "Comparative study of Swing Equation-based and full emulation-based Virtual Synchronous Generators," 11th International Conference on Power Electronics, Machines, and Drives (PEMD 2022), 2022, pp. 578-582. Adhering to IET copyright policy, it is being reproduced here for her own thesis with the above acknowledgment (https://pemd.theiet.org/media/1741/pemd-2022-full-paper-template.docx).

7.1 Introduction

In Chapter 2, the Swing Equation-based VSG is introduced and in Chapter 5, the detailed synchronous machine emulation VSG is discussed. Both models use the swing equation dynamics for speed and rotor mechanical angle calculations but differ in the representation of the electrical part. The SE-based VSG uses a simplified representation of a voltage source behind an impedance, while the detailed SM emulation VSG uses a detailed transient model of a synchronous machine.

In this chapter, the performances of i) the SE-based VSG, ii) detailed SM emulation VSG and iii) a real SG are compared and contrasted using Electromagnetic Transients (EMT) simulation. Using a simple test system, their behavior is compared when subjected to step changes in power order and faults. It is shown that the two approaches have nearly equivalent performance if the damping is properly represented in the SE-based approach. Also, it is shown that the current limit is more readily incorporable in the detailed SM emulation approach than in the SE-based approach.

7.2 Similarity with an Actual Synchronous Generator

In the past decades, the conventional power system was dominated by synchronous generators (SG); thus, all the system-level planning and controlling schemes were developed based on the characteristics of SG. If the VSC is controlled in the manner of an SG, it seems, at first glance, reasonable to treat the converter with VSG controller as a conventional SG from the control level of the grid side. Therefore, the existing control scheme is still suitable for VSG-typed converters. However, it should be noted that a real SG can supply significantly more fault current than a VSG, which uses a power electronic converter and hence must incorporate a current limiting function. Transient fault behavior of the SG and VSG would generally differ if the maximum current limit is encountered.

This section uses EMT simulation to compare the performance of SE-based and detailed SM emulation VSG. In order to check whether the converter with these two VSG options indeed behave like a real synchronous generator, the performance is also compared with a case with a real SG.

7.2.1 System Description

The system layout is in Figure 7-1 and the main system parameters are in Table 7-1.

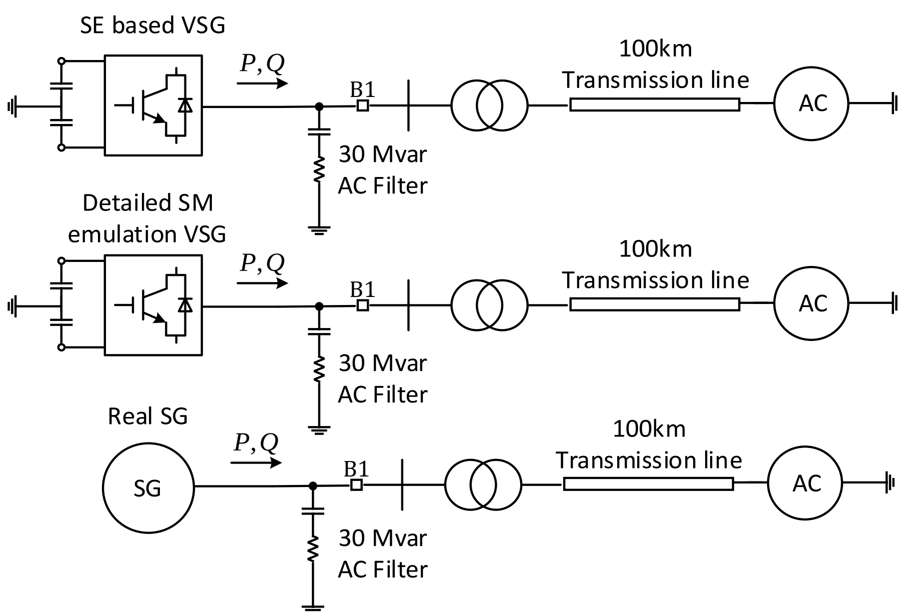

Figure 7-1 Test System Layout

Three different representations are considered in this case:

1) VSC with Swing Equation-based VSG
2) VSC with Detailed Synchronous Machine Emulation VSG
3) Actual synchronous generator (for comparison)

The parameters of the SE-based VSG and detailed SM emulation VSG are given in Table 7-2 and Table 7-3, respectively. The parameters of actual SG are the same as detailed SM emulation VSG.

Table 7-1 System Parameters

Parameter	Value	Parameter	Value
Dc side voltage V_{dc}	$\pm 100kV$	Transformer MVA	$250MVA$
Dc side shunt capacitance	$2 \times 1000\mu F$	Transformer voltage	95/220 kV
Converter rated power	$210MVA$	Transformer resistance	0.024 pu
Converter rated voltage	$95kV$ (L-L)	Transformer leakage inductance	$0.18pu$
Converter inductance	$0.1H$	Transmission line length	100 km
Converter filter resistance	100Ω	System frequency	$60Hz$
Converter filter capacitance	$10.0\mu F$		

Table 7-2 Parameters of SE-based VSG

Parameter	Value	Parameter	Value	Parameter	Value
H	3.42 s	K	1.0 s	P_{ref}	1.0 pu
D_p	20.0	D_w	0.0	V_{ref}	1.0 pu

Table 7-3 Parameters of Detailed SM Emulation VSG

Parameter	Value	Parameter	Value	Parameter	Value
H	3.42 s	D_w	0.0	T_C	1.0 s
L_a	0.15 pu	L_{md}	1.50 pu	K_A	200.0 pu
L_{1d}	0.1097 pu	L_{fd}	0.119 pu	V_{IMAX}	10 pu
L_{mq}	1.44 pu	L_{1q}	0.395 pu	V_{RMAX}	5.64 pu
L_{2q}	0.0669 pu	R_a	0.0043 pu	K_C	0.0 pu
R_{1d}	0.01823 pu	R_{fd}	$0.000895pu$	T_B	10.0 s
R_{1q}	0.0104 pu	R_{2q}	0.0167 pu	T_A	0.015 s
V_{ref}	1.0 pu	V_{IMIN}	-10 pu	T_r	$0.02s$
P_{ref}	1.0 pu	V_{RMIN}	-4.53 pu		

Two scenarios are investigated, and the results are shown in the next section:

1) A step-change in the power reference.
2) A three-phase to ground fault at the transmission line midpoint.

7.2.2 System Operation with Power Reference Increase

In this simulation, a step change in power from $0.5\,pu$ to $1.0\,pu$ is applied at $1\,s$ in both models. The waveforms of frequency and phase angle δ between the VSG and the remote source for the two VSG options are as in Figure 7-2. The results with an actual SG are also superimposed for comparison.

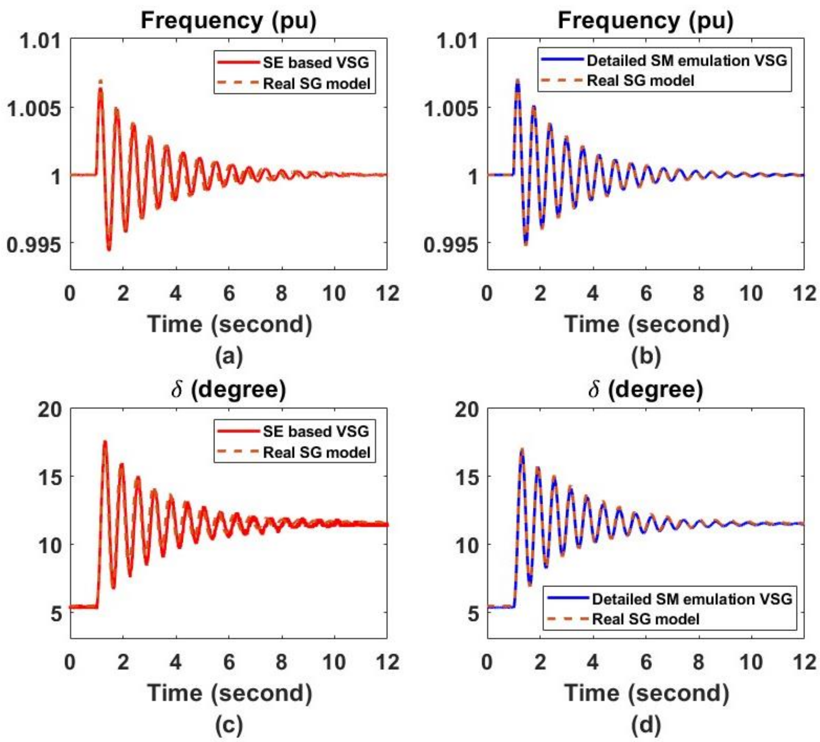

Figure 7-2 Frequency and Voltage Angle Waveforms with the Power Increase

From Figure 7-2 (a) and (b), the frequency in either option oscillates following the power order increase and recovers to its nominal value to keep synchronism with the grid. Both VSG schemes have essentially identical rates of change of frequency (RoCoF) when compared with the real SG. Therefore, the inertia support is similar. This is reasonable because the inertia constants used in all three cases: i) the real SG, ii) the SE-based VSG, and iii) the detailed SM emulation VSG are the same. Here, the dc side was idealized as a voltage source. The results may differ for the real system, where the remote converter may be connected to a weak ac system so that it has a limitation on the ability to transfer energy rapidly.

As expected, the detailed SM emulation VSG and a real SG show essentially identical results. As explained in Chapter 2, the SE-based VSG ignores the higher-order behaviour of a real SG. Therefore, it manifests a slightly different oscillation frequency and damping behaviour.

Similarly, in Figure 7-2 (c) and (d), with both VSG options, when the power increases, the voltage angle δ oscillates and settles at a larger value corresponding to the increased power level.

7.2.3 System Operation with A Three-phase To Ground Fault

A $150\,ms$ duration three-phase-to-ground fault is applied at the midpoint of the transmission line at $t = 1\,s$. The frequency waveforms and voltage angle δ for the two different VSGs are shown in Figure 7-3 (superimposed on the results from the real SG).

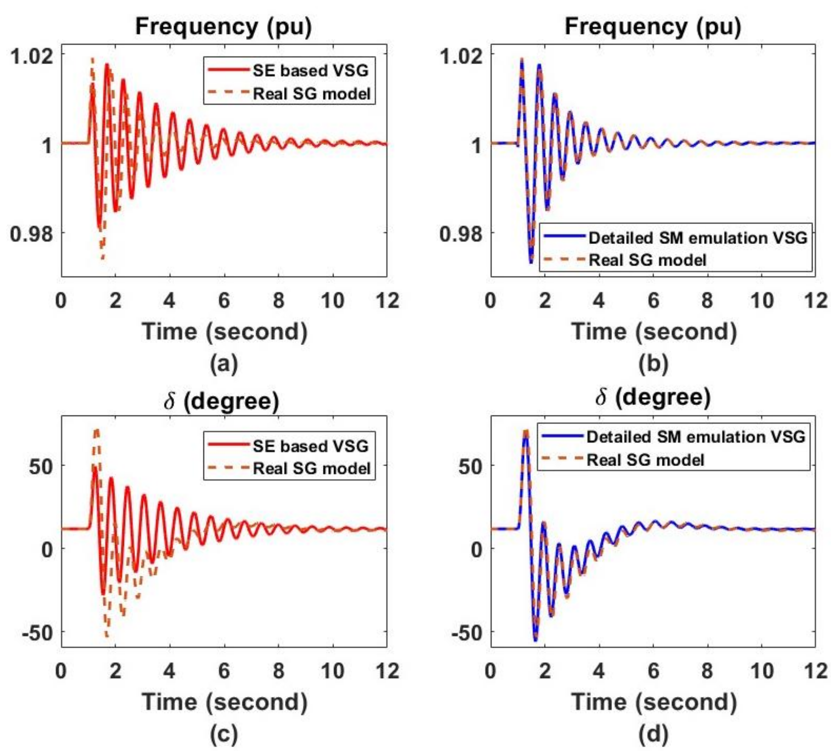

Figure 7-3 Frequency and Voltage Angle Waveforms with A Fault

From Figure 7-3, the frequency of both VSGs recovers to its nominal value after the fault is cleared, demonstrating that both VSG options have adequate fault ride-through capability. The angle δ also shows similar behaviour. Here there is no change in transmitted power on recovery and so δ returns to its pre-fault value when oscillations cease. The responses of the converter with detailed SM emulation VSG have a better fidelity with the real SG as compared to the SE-based VSG.

7.3 Over-current Protection

As discussed in Section 2.1 the direct control variable of SE-based VSG is the converter's terminal voltage. Therefore, there is no inherent over-current protection, the current can only be indirectly restricted via the terminal voltage.

The switchable current limiting control in Section 2.2 (Figure 2-6) is an effective method to prevent over-current damage during the fault. However, the shortage of this current limiting method is that this method relies on the sensitivity of the fault detection block. Also, since the PI controller is used in the current limiting block, the current may overshoot the reference transiently or have a slow response depending on the controller's gains. As shown in Figure 2-14 in Chapter 2, a short-time spike can be observed in the current magnitude at $0.5\ s$, which indicates that at the beginning of the fault, the current magnitude cannot be properly limited and is higher than the maximum limitation.

This disadvantage mentioned above can be avoided when a detailed SM emulation VSG is used. According to Chapter 5, the direct control variables of the detailed SM emulation VSG are the system currents. As a hysteresis type controller is used, which has negligible controller delay in achieving the ordered currents, the dynamic response is greatly simplified. Thus, over-current protection can be applied to the control easily by limiting the current orders as discussed in section 5.3.

7.4 Chapter Conclusion

In conclusion, the following facts can be deduced:

1) To accurately include mechanical damping effects, the SE-based approach should have two terms related to damping torque. The first term is to represent amortisseur winding effects, where damping is proportional to the difference between synchronous speed and actual speed, and the other term is only

proportional to windage damping. On the other hand, the detailed SM emulation VSG has damper windings included in the model, so the swing equation only includes the windage effects.

2) The simulation study shows that the dynamic response of the detailed SM emulation VSG (such as the rate of frequency change under various transients) is identical to that of a real SG. Nevertheless, the dynamic performance of the SE-based VSG is very similar to that of the real SG.
3) In the past decades, the conventional power system is dominated by the SGs, thus, in the legacy power network, all the system-level planning and control schemes have been developed based on the characteristics of SG. Because of the high similarity with SG, it is reasonable to treat the converter with detailed SM emulation VSG as an SG from the grid side. Besides, all the past experience about SG can still be applied to this VSG method without a large modification.
4) Limiting the current is straightforward in the detailed SM Emulation VSG. On the other hand, the current limiting feature in the SE-based VSG requires some additional tuning efforts.

8 Concluding Remarks and Future Work

8.1 Summary of the Thesis Research

The key contributions of this thesis research are summarized below:

1. This thesis proposes a new method of implementing a virtual synchronous generator (VSG) using an improved current source interface. To demonstrate advantages of the approach, a comparison with existing or recently emerging approaches such as Swing Equation (SE) based VSG is also developed. Therefore, the first part of the thesis focuses on the investigation of the SE-based VSG and its application.

- The SE-based VSG method is inspired by the mechanical equations of synchronous generators. The converter can mimic the behaviors of the SG model with this control; therefore, limited inertia and damping support can be provided to the system. Since the damper windings are all ignored in the SE-based VSG, their effect can be approximated by modifying the damping in the swing equation mechanical dynamics. Thus, the damping coefficient needs to be well-tuned.
- Since the control variables of SE-based VSG are voltage signals, it is difficult to have inherent current limits as are needed to prevent overcurrent damage to the VSG's semiconductor switches. A current limiting method referred to as 'switchable current limiting control' is applied to the SE-based VSG. This current limiting block highly relies on the effectiveness of the fault detection block and the converter also may face overshoot phenomenon due to the slow response of the PI controller used inside.

2. Application of the SE-based VSG: Demonstration of how SE-based VSGs are efficient in ensuring parallel operation of two VSC-HVdc links.

- For environmental considerations, the HVdc links are increasingly being recommended for providing power to offshore oil/gas drilling platforms instead of traditional gas generators on platforms. The VSG method is shown to be a suitable choice for this application since the load sharing can be done automatically without extra communication links.

- A slower secondary frequency regulation loop is needed in the SE-based VSG to eliminate the steady state error of ω when the converter is connected to the passive loads.
- The SE-based VSG is compared with the Master/Slave controller in different operation situations in the EMT simulation program, such as load balancing, start-up of offshore induction motors, transferring and tripping of loads in case of failure of one of the links, and fault recovery and ride-through.

3. A novel acceleration slope-based hysteresis current control designed for MMC is developed: In order to develop a current source interfaced VSG, one of the hurdles which needs to be overcome is to develop a method to control the MMC act as a current source with a very fast response.

The candidate considers this to be a major contribution of the thesis.

- In order to control the converter as a high-bandwidth and high-precision current source, a novel acceleration slope-based hysteresis current controller is developed. Unlike the well-known traditional hysteresis controller used with 2-level VSCs, this algorithm is designed for use with MMCs. It makes use of the multiple voltage steps available with the MMC and accelerates or decelerates the rate of change of current depending on whether it deviates significantly from the target current.
- The successful operation of the proposed hysteresis current controller is validated in offline testing using Electromagnetic Transients simulation (PSCAD/EMTDC program).
- An algorithm to compute the power loss is used for the acceleration slope-based hysteresis current controller. The dependence of the loss on the number of MMC levels is investigated. For comparison, the power loss analysis for a current source implemented on a 2-level VSC using the traditional hysteresis controller is also conducted.

- Results show that the MMC with the proposed current control method has significantly less power loss than a two-level VSC with the traditional hysteresis method.
- Additionally, as the number of submodules per arm is made larger, the power loss of the MMC decreases and eventually saturates. When the MMC has 10 or more levels, the power loss with the proposed method is essentially the same as that of an MMC controlled as a voltage source, which is the commonly used configuration for MMCs in HVdc transmission applications.

4. Application of the proposed acceleration slope-based hysteresis current controller: Demonstration of the active power filter.

- With the hysteresis current control method, the usage of the MMC can be extended into more application areas that need high-speed and accurate current control ability.
- One of the popular applications is the active power filter (APF), which identifies the undesirable components of the load current and injects a canceling component into the grid to offset these components.
- An MMC-based active power filter is investigated as an application example of the proposed hysteresis current controller. The EMT simulation is used to develop the concept and select feasible controller parameters, after which the controller is physically constructed and tested in a hardware-in-loop environment with the electrical network part implemented on a real-time simulator.
- Both the EMT simulation and HIL experiment prove that the MMC-based APF can indeed inject currents into the system to cancel the unbalanced and harmonics component of the system currents to improve the power quality.

5. Implementation of a VSG strategy using the proposed acceleration slope-based hysteresis current controller: Using the proposed hysteresis current controller, the VSC is interfaced as a rapidly controllable current source and faithfully operated as the VSG with the characteristic of a real SG (albeit with limited overcurrent capability as compared to the real SG). The approach also allows one to represent the VSG with the differential

equations of an actual SG with as much detail as desired, such as a number of d- and q-axis windings, etc.

- A detailed SM emulation VSG is constructed that has the same detailed structure as a real SG. All the windings of the SG are built inside this controller, the parameters selection can use the SG as a reference which has been well studied.
- The control variables of detailed SM emulation VSG are current signals; therefore, it is easy to have inherent restrictions to the current references. The current limiting blocks and virtual rotor speed reset mechanism are applied to the detailed SM emulation VSG. The current restriction could strictly limit the converter current under a pre-set value during the whole operation. Also, the inclusion of these extra controllers improves the fault ride-through capability of the VSG.

6. Comparison of VSGs with different number of damper windings using small signal analysis: Small signal analysis is used to investigate the performance of the SM emulation VSGs (current source interfaced VSGs) with different levels of detail in the SG's representation (e.g., different number of damper windings, etc.), as well as under different ac systems with varying SCR. The conclusions of the eigenvalues analysis are all validated by the EMT simulations.

- Small signal models are developed for the various current source interfaced VSG options. Stability information can then be garnered by computing the eigenvalues of the SS models.
- These analytical SS models are successfully validated using Electromagnetic Transients (EMT) simulations.
- Using the SS models, the root locus analysis shows that with or without the damper windings, the current source interfaced VSG remains stable not only in weak systems ($SCR < 2$) but also in ultra-stiff systems ($SCR > 30$), which was identified as a challenge for earlier voltage source interfaced VSG implementations.
- Also, eigenvalue analysis is conducted on current source interfaced VSGs to investigate the effect of inclusion/exclusion of the damper windings. Results

show that for a given ac system, the inclusion of d- and q-axis damper winding impedances in the VSG can marginally improve the transient performance.

7. Optimization of VSG parameters for superior damping performance: Since the VSG is not restricted to use realistic values for the machine parameters as in a real SG, the parameters could be optimized to obtain the largest damping ratio.

- A Genetic Algorithms (GA) optimization procedure is applied to optimize the parameters of the SM emulation VSG.
- Results show that the transient performance, e.g., the damping ratio can be improved significantly by a factor of 7 or more.

8. Comparison of the performance of SE-based VSG, the proposed novel SM emulation VSG with that of a real SG:

- The SE-based VSG and detailed SM emulation VSG are compared with respect to their impacts on damping, closeness to the operation of a real synchronous generator, and limiting of over-current.
- The simulation study shows that with suitable parameters, the dynamic responses of both VSG options are similar to that of the real SG.
- Limiting the current is straightforward in the SM emulation VSG, unlike in the case of the SE-based VSG which requires additional effort.
- Since the damper windings are not represented in the SE-base VSG, a damping term proportional to the slip frequency is added to the mechanical part to crudely represent the damping effects of the damping windings in a real SG. However, such an approach is not necessary for the SM emulation VSG, since all the damping windings are included in the model.

8.2 Publications Resulting from the Thesis

The following papers and patents are the results of the research in this thesis:

Conference Papers:

- ***C. Jiang***, *A. D. Sinkar, M. K. Das, A. M. Gole, and V. Pathirana, "***A comparative study of master-slave control and virtual synchronous machine control for parallel VSC-HVDC links feeding passive loads on offshore platforms***," 15th IET*

International Conference on AC and DC Power Transmission (ACDC 2019), Coventry, UK, 2019, pp. 1-6.

- *Jia Lu,* ***Chen Jiang****, Haoyan Xue, Akihiro Ametani and Aniruddha Gole, "****Study on Numerical Fourier/ Laplace Transformation and Inversion****," IEE Japan HV Conference, Tsushima-Island, Japan, 2020, pp. 1-6.*
- ***C. Jiang****, A. D. Sinkar and A. M. Gole, "****Comparative study of Swing Equation-based and full emulation-based Virtual Synchronous Generators****," 11th International Conference on Power Electronics, Machines, and Drives (PEMD 2022), 2022, pp. 578-582*

Journal Paper:

- ***C. Jiang****, A. M. Gole, and Y. Zhang "* ***Novel Hysteresis Current Control for Modular Multilevel Converters Using Acceleration Slope****," Under preparation for IEEE Transactions on Power Delivery.*
- ***Chen Jiang****, Ajinkya D. Sinkar, Aniruddha M. Gole, "****Small signal analysis of a grid-forming modular multilevel converter with a novel virtual synchronous generator control****", Electric Power Systems Research, Volume 223, 2023.*
- ***C. Jiang****, Jhair S. Acosta and Aniruddha M. Gole, "****Robust Parameter Optimization of a Novel Grid-Forming Modular Multilevel Converter Using Genetic Algorithm****", under preparation for The Power Systems Computation Conference 2024 (Electric Power Systems Research).*

Ongoing US Patent Application:

- ***C. Jiang****, A. M. Gole, "* ***Novel Hysteresis Current Control with a Modular Multilevel Converter Using an Acceleration Slope****," US Provisional Patent Application No. 63/502,189, May 2023.*

8.3 Future Work

There still exist several valuable topics for further research, which are shortly summarized in this section.

8.3.1 Adaptive Control Algorithm for SM Emulation VSG

Without the physical limitations, the parameters that are fixed for SG can now be manipulated in the VSG algorithm. Even some dynamic optimization algorithms can be embedded inside the VSG control model. The goal is to gain even better performance than SG.

For example, the varying inertia constant (H) can be added to the detailed SM emulation VSG control. The typical power-angle curve of synchronous generators is in Figure 8-1 [17].

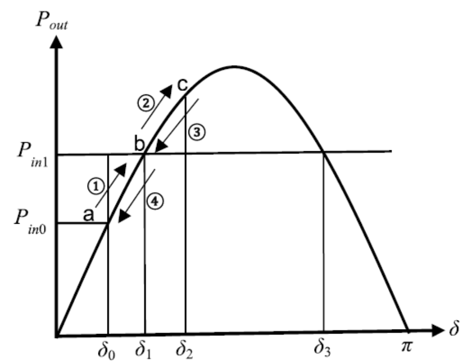

Figure 8-1 Power Angle Curve

The input power is changed from P_{in0} to P_{in1}. There are four segments ($a \rightarrow b, b \rightarrow c, c \rightarrow b, b \rightarrow a$) in Figure 8-1. During each segment, the sign of $\frac{d\omega}{dt}$ together with the sign of $\Delta\omega$ defines acceleration or deceleration. The inertia constant H can be changed according to these acceleration or deceleration processes. A large value of H can be used during acceleration phases to reduce the acceleration and a small value of H is chosen during deceleration phases to boost the deceleration.

8.3.2 Investigation of High Renewable Penetrated Network with Multiple VSGs and Other VSCs

It is proposed to investigate the behavior of SM emulation VSG in a system with a high penetration of inverter-based generation. The IEEE 21-bus system as shown in Figure 8-2 [77] could be used as a starting point for such a study.

From the figure, the distributed generations are connected to the utility source using an inverter interface. The proposed SM emulation VSG can be applied to these VSC inverters. Also, some other control strategies can be used. In this case, firstly, the advantages and disadvantages of the VSG can be investigated under this high-penetration of inverter-based generation. Then, the corporation ability of VSG and other control methods can be discussed.

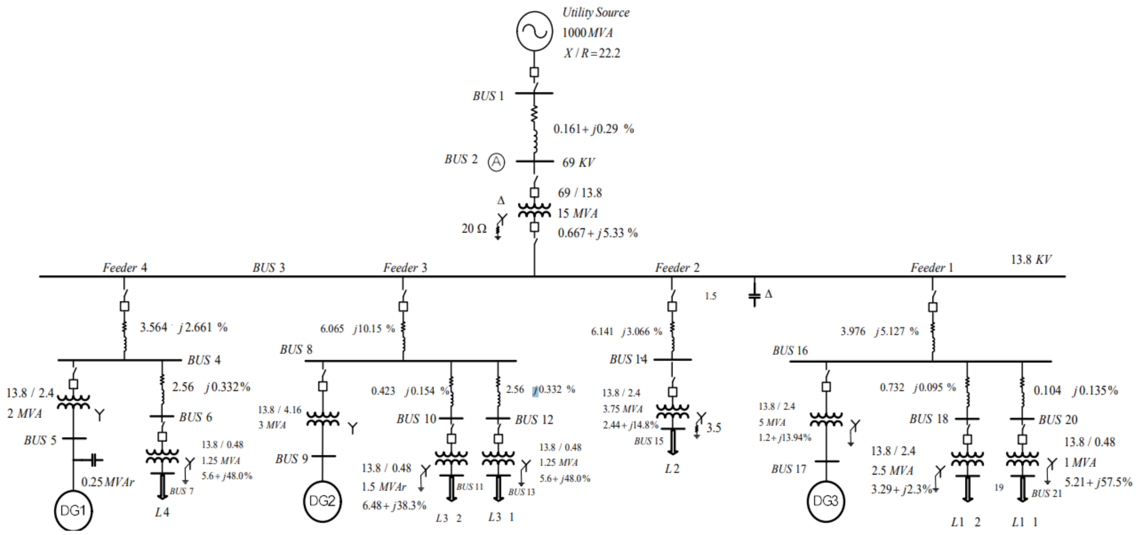

Figure 8-2 IEEE 21-bus System

Another interesting study is replacing the SG model with a distributed power to study the system stability of the pure inverter-based generation power system.

Appendix I

The small signal model of the '2.1' and '3.3' SM emulation VSG options (current source interfaced VSGs) are derived in this appendix. Similar to section 6.1.1.6, the accuracy of the SS models of these VSG options can also be validated (not shown).

A1.1 Small Signal Model of '2.1' SM Emulation VSG

The equations related to the $\Delta\psi_{1d}$, Δi_{1d}, $\Delta\psi_{1q}$, Δi_{1q}, $\Delta\psi_{2q}$ and Δi_{2q} are removed from the '3.2' VSG option. Therefore, the small signal equations of the '2.1' SM emulation VSG are from (A-1) to (A-8). Please remember that any variables with a superscript '0' means its steady-state value where the system is linearized. Also, V_l is equal to $\sqrt{(v_d^0)^2 + (v_q^0)^2}$, K_A' is equal to $K_A \cdot \frac{R_{fd}}{L_{md}}$ and δ is the angle between the d-axis and R-axis.

$$\frac{1}{\omega_n}\frac{d\Delta\psi_d}{dt} = -X_s\Delta i_q - E_B sin\delta^0\Delta\delta - R_a\Delta i_d - \omega^0\Delta\psi_q - \psi_q^0\Delta\omega \quad \text{(A-1)}$$

$$\frac{1}{\omega_n}\frac{d\Delta\psi_{fd}}{dt} = \Delta E_{fd} - R_{fd}\Delta i_{fd} \quad \text{(A-2)}$$

$$\frac{1}{\omega_n}\frac{d\Delta\psi_q}{dt} = X_s\Delta i_d - E_B cos\delta^0\Delta\delta - R_a\Delta i_q + \omega^0\Delta\psi_d + \psi_d^0\Delta\omega \quad \text{(A-3)}$$

$$\frac{d\Delta\omega}{dt} = \frac{\Delta P_{ref}}{2H} - \frac{D_w}{2H}\Delta\omega - \frac{i_q^0}{2H}\Delta\psi_d - \frac{\psi_d^0}{2H}\Delta i_q + \frac{i_d^0}{2H}\Delta\psi_q + \frac{\psi_q^0}{2H}\Delta i_d \quad \text{(A-4)}$$

$$\frac{1}{\omega_n}\frac{d\Delta\delta}{dt} = -\Delta\omega \quad \text{(A-5)}$$

$$\frac{d\Delta E_{fd}}{dt} = -\frac{1}{T_A}\Delta E_{fd} + \frac{K_A'}{T_A}\left(1 - \frac{T_C}{T_B}\right)\Delta X_{E1} + \frac{K_A' T_C}{T_A T_B}\Delta V_{ref} - \frac{K_A' T_C}{T_A T_B}\Delta X_{E2} \quad \text{(A-6)}$$

$$\frac{d\Delta X_{E1}}{dt} = \frac{1}{T_B}\Delta V_{ref} - \frac{1}{T_B}\Delta X_{E1} - \frac{1}{T_B}\Delta X_{E2} \quad \text{(A-7)}$$

$$\frac{d\Delta X_{E2}}{dt} = -\frac{1}{T_r}\Delta X_{E2} + \frac{v_d^0}{T_r V_l}(-X_s)\Delta i_q + \frac{v_d^0}{T_r V_l}(-E_B \sin\delta^0)\Delta\delta + \frac{v_q^0}{T_r V_l}X_s\Delta i_d +$$

$$\frac{v_q^0}{T_r V_l}(-E_B \cos\delta^0)\Delta\delta \quad \text{(A-8)}$$

The classical state variable form of this '2.1' VSG small signal model is in (A-9), which is the same as (6-50), and 'T' is the transpose of the matrix.

$$\frac{d\boldsymbol{\Delta x_{21}}}{dt} = \boldsymbol{A_{21}\Delta x_{21}} + \boldsymbol{B_{21}\Delta u} \tag{A-9}$$

Here,

$$\boldsymbol{A_{21}} = [\boldsymbol{M_{21}} + \boldsymbol{N_{21}}(\boldsymbol{L'_{21}})^{-\mathbf{1}}] \tag{A-10}$$

$$\boldsymbol{M_{21}} =$$

$$\begin{pmatrix} 0 & 0 & -\omega^0\omega_n & -\psi_q^0\omega_n & -E_B sin\delta^0\omega_n & 0 & 0 & 0 \\ 0 & 0 & 0 & 0 & 0 & \omega_n & 0 & 0 \\ \omega^0\omega_n & 0 & 0 & \psi_d^0\omega_n & -E_B cos\delta^0\omega_n & 0 & 0 & 0 \\ -\frac{i_q^0}{2H} & 0 & \frac{i_d^0}{2H} & -\frac{D_w}{2H} & 0 & 0 & 0 & 0 \\ 0 & 0 & 0 & -\omega_n & 0 & 0 & 0 & 0 \\ 0 & 0 & 0 & 0 & 0 & -\frac{1}{T_A} & \frac{K'_A}{T_A}(1-\frac{T_C}{T_B}) & -\frac{K'_A T_C}{T_A T_B} \\ 0 & 0 & 0 & 0 & 0 & 0 & -\frac{1}{T_B} & -\frac{1}{T_B} \\ 0 & 0 & 0 & 0 & \frac{-E_B v_d^0 sin\delta^0 - E_B v_q^0 cos\delta^0}{T_r V_l} & 0 & 0 & -\frac{1}{T_r} \end{pmatrix} \tag{A-11}$$

$$\boldsymbol{N_{21}} = \begin{pmatrix} -R_a\omega_n & 0 & -X_s\omega_n & 0 & 0 & 0 & 0 & 0 \\ 0 & -R_{fd}\omega_n & 0 & 0 & 0 & 0 & 0 & 0 \\ X_s\omega_n & 0 & -R_a\omega_n & 0 & 0 & 0 & 0 & 0 \\ \frac{\psi_q^0}{2H} & 0 & -\frac{\psi_d^0}{2H} & 0 & 0 & 0 & 0 & 0 \\ 0 & 0 & 0 & 0 & 0 & 0 & 0 & 0 \\ 0 & 0 & 0 & 0 & 0 & 0 & 0 & 0 \\ 0 & 0 & 0 & 0 & 0 & 0 & 0 & 0 \\ \frac{v_q^0}{T_r V_l}X_s & 0 & -\frac{v_d^0}{T_r V_l}X_s & 0 & 0 & 0 & 0 & 0 \end{pmatrix} \tag{A-12}$$

$$\boldsymbol{\Delta x_{21}} = \left(\Delta\psi_d \;\; \Delta\psi_{fd} \;\; \Delta\psi_q \;\; \Delta\omega \;\; \Delta\delta \;\; \Delta E_{fd} \;\; \Delta X_{E1} \;\; \Delta X_{E2}\right)^T \tag{A-13}$$

$$\boldsymbol{\Delta i_{21}} = \left(\Delta i_d \;\; \Delta i_{fd} \;\; \Delta i_q \;\; 0 \;\; 0 \;\; 0 \;\; 0 \;\; 0\right)^T \tag{A-14}$$

$$\boldsymbol{\Delta u} = (\Delta P_{ref} \quad \Delta V_{ref})^T \tag{A-15}$$

$$\boldsymbol{B_{32}} = \begin{pmatrix} 0 & 0 & 0 & \frac{1}{2H} & 0 & 0 & 0 & 0 \\ \\ 0 & 0 & 0 & 0 & 0 & \frac{K_A' T_C}{T_A T_B} & \frac{1}{T_B} & 0 \end{pmatrix}^T \tag{A-16}$$

Also, the entries '$\mathbf{0}$' in (A-17) are 5×5 zero matrices.

$$\boldsymbol{L_{21}} = \begin{pmatrix} L_a + L_{md} & L_{md} & 0 \\ L_{md} & L_{fd} + L_{kf} + L_{md} & 0 \\ 0 & 0 & L_a + L_{mq} \end{pmatrix} \tag{A-17}$$

$$\boldsymbol{L_{21}'} = \begin{pmatrix} \boldsymbol{L_{21}} & \mathbf{0} \\ \mathbf{0} & \mathbf{0} \end{pmatrix} \tag{A-18}$$

A1.2 Small Signal Model of '3.3' SM Emulation VSG

The equations related to the $\Delta\psi_{2q}$ and Δi_{2q} can be added to the '3.2' VSG model. Therefore, the small signal equations of the '3.3' SM emulation VSG are from (A-19) to (A-29). Please remember that any variable with a superscript '0' means its steady-state value where the system is linearized. Also, V_l is equal to $\sqrt{(v_d^0)^2 + (v_q^0)^2}$, K_A' is equal to $K_A \cdot \frac{R_{fd}}{L_{md}}$ and δ is the angle between the d-axis and R-axis.

$$\frac{1}{\omega_n}\frac{d\Delta\psi_d}{dt} = -X_s\Delta i_q - E_B sin\delta^0\Delta\delta - R_a\Delta i_d - \omega^0\Delta\psi_q - \psi_q^0\Delta\omega \tag{A-19}$$

$$\frac{1}{\omega_n}\frac{d\Delta\psi_{1d}}{dt} = -R_{1d}\Delta i_{1d} \tag{A-20}$$

$$\frac{1}{\omega_n}\frac{d\Delta\psi_{fd}}{dt} = \Delta E_{fd} - R_{fd}\Delta i_{fd} \tag{A-21}$$

$$\frac{1}{\omega_n}\frac{d\Delta\psi_q}{dt} = X_s\Delta i_d - E_B cos\delta^0\Delta\delta - R_a\Delta i_q + \omega^0\Delta\psi_d + \psi_d^0\Delta\omega \tag{A-22}$$

$$\frac{1}{\omega_n}\frac{d\Delta\psi_{1q}}{dt} = -R_{1q}\Delta i_{1q} \tag{A-23}$$

$$\frac{1}{\omega_n}\frac{d\Delta\psi_{2q}}{dt} = -R_{2q}\Delta i_{2q} \tag{A-24}$$

$$\frac{d\Delta\omega}{dt} = \frac{\Delta P_{ref}}{2H} - \frac{D_w}{2H}\Delta\omega - \frac{i_q^0}{2H}\Delta\psi_d - \frac{\psi_d^0}{2H}\Delta i_q + \frac{i_d^0}{2H}\Delta\psi_q + \frac{\psi_q^0}{2H}\Delta i_d \tag{A-25}$$

$$\frac{1}{\omega_n}\frac{d\Delta\delta}{dt} = -\Delta\omega \tag{A-26}$$

$$\frac{d\Delta E_{fd}}{dt} = -\frac{1}{T_A}\Delta E_{fd} + \frac{K_A'}{T_A}\left(1 - \frac{T_C}{T_B}\right)\Delta X_{E1} + \frac{K_A' T_C}{T_A T_B}\Delta V_{ref} - \frac{K_A' T_C}{T_A T_B}\Delta X_{E2} \tag{A-27}$$

$$\frac{d\Delta X_{E1}}{dt} = \frac{1}{T_B}\Delta V_{ref} - \frac{1}{T_B}\Delta X_{E1} - \frac{1}{T_B}\Delta X_{E2} \tag{A-28}$$

$$\frac{d\Delta X_{E2}}{dt} = -\frac{1}{T_r}\Delta X_{E2} + \frac{v_d^0}{T_r V_l}(-X_s)\Delta i_q + \frac{v_d^0}{T_r V_l}(-E_B \sin\delta^0)\Delta\delta + \frac{v_q^0}{T_r V_l}X_s \Delta i_d +$$

$$\frac{v_q^0}{T_r V_l}(-E_B \cos\delta^0)\Delta\delta \tag{A-29}$$

The classical state variable form of this ‘3.3’ VSG small signal model is in (A-30), which is the same as (6-51). ‘T’ is the transpose of the matrix.

$$\frac{d\boldsymbol{\Delta x_{33}}}{dt} = \boldsymbol{A_{33}\Delta x_{33}} + \boldsymbol{B_{33}\Delta u} \tag{A-30}$$

Here,

$$\boldsymbol{A_{33}} = [\boldsymbol{M_{33}} + \boldsymbol{N_{33}}(\boldsymbol{L'_{33}})^{-\boldsymbol{1}}] \tag{A-31}$$

$$\boldsymbol{\Delta x_{33}} = \left(\Delta\psi_d\ \ \Delta\psi_{1d}\ \ \Delta\psi_{fd}\ \ \Delta\psi_q\ \ \Delta\psi_{1q}\ \ \Delta\psi_{2q}\ \ \Delta\omega\ \ \Delta\delta\ \ \Delta E_{fd}\ \ \Delta X_{E1}\ \ \Delta X_{E2}\right)^T \tag{A-32}$$

$$\boldsymbol{M_{33}} =$$

$$\begin{pmatrix}
0 & 0 & 0 & -\omega^0\omega_n & 0 & 0 & -\psi_q^0\omega_n & -E_B sin\delta^0\omega_n & 0 & 0 & 0 \\
0 & 0 & 0 & 0 & 0 & 0 & 0 & 0 & 0 & 0 & 0 \\
0 & 0 & 0 & 0 & 0 & 0 & 0 & 0 & \omega_n & 0 & 0 \\
\omega^0\omega_n & 0 & 0 & 0 & 0 & 0 & \psi_d^0\omega_n & -E_B cos\delta^0\omega_n & 0 & 0 & 0 \\
0 & 0 & 0 & 0 & 0 & 0 & 0 & 0 & 0 & 0 & 0 \\
0 & 0 & 0 & 0 & 0 & 0 & 0 & 0 & 0 & 0 & 0 \\
-\frac{i_q^0}{2H} & 0 & 0 & \frac{i_d^0}{2H} & 0 & 0 & -\frac{D_w}{2H} & 0 & 0 & 0 & 0 \\
0 & 0 & 0 & 0 & 0 & 0 & -\omega_n & 0 & 0 & 0 & 0 \\
0 & 0 & 0 & 0 & 0 & 0 & 0 & 0 & -\frac{1}{T_A} & \frac{K_A'}{T_A}(1-\frac{T_C}{T_B}) & -\frac{K_A' T_C}{T_A T_B} \\
0 & 0 & 0 & 0 & 0 & 0 & 0 & 0 & 0 & -\frac{1}{T_B} & -\frac{1}{T_B} \\
0 & 0 & 0 & 0 & 0 & 0 & 0 & \frac{-E_B v_d^0 sin\delta^0 - E_B v_q^0 cos\delta^0}{T_r V_l} & 0 & 0 & -\frac{1}{T_r}
\end{pmatrix}$$

(A-33)

$$\boldsymbol{N_{33}} =$$

$$\begin{pmatrix} -R_a\omega_n & 0 & 0 & -X_s\omega_n & 0 & 0 & 0 & 0 & 0 & 0 & 0 \\ 0 & -R_{1d}\omega_n & 0 & 0 & 0 & 0 & 0 & 0 & 0 & 0 & 0 \\ 0 & 0 & -R_{fd}\omega_n & 0 & 0 & 0 & 0 & 0 & 0 & 0 & 0 \\ X_s\omega_n & 0 & 0 & -R_a\omega_n & 0 & 0 & 0 & 0 & 0 & 0 & 0 \\ 0 & 0 & 0 & 0 & -R_{1q}\omega_n & 0 & 0 & 0 & 0 & 0 & 0 \\ 0 & 0 & 0 & 0 & 0 & -R_{2q}\omega_n & 0 & 0 & 0 & 0 & 0 \\ \frac{\psi_q^0}{2H} & 0 & 0 & -\frac{\psi_d^0}{2H} & 0 & 0 & 0 & 0 & 0 & 0 & 0 \\ 0 & 0 & 0 & 0 & 0 & 0 & 0 & 0 & 0 & 0 & 0 \\ 0 & 0 & 0 & 0 & 0 & 0 & 0 & 0 & 0 & 0 & 0 \\ 0 & 0 & 0 & 0 & 0 & 0 & 0 & 0 & 0 & 0 & 0 \\ \frac{v_q^0}{T_r V_l}X_s & 0 & 0 & -\frac{v_d^0}{T_r V_l}X_s & 0 & 0 & 0 & 0 & 0 & 0 & 0 \end{pmatrix}$$

(A-34)

$$\boldsymbol{\Delta u} = (\Delta P_{ref} \quad \Delta V_{ref})^T \qquad \text{(A-35)}$$

$$\boldsymbol{\Delta i_{33}} = \left(\Delta i_d \;\; \Delta i_{1d} \;\; \Delta i_{fd} \;\; \Delta i_q \;\; \Delta i_{1q} \;\; \Delta i_{2q} \;\; 0 \;\; 0 \;\; 0 \;\; 0 \;\; 0\right)^T \qquad \text{(A-36)}$$

$$\boldsymbol{B_{33}} = \begin{pmatrix} 0 & 0 & 0 & 0 & 0 & 0 & \frac{1}{2H} & 0 & 0 & 0 & 0 \\ 0 & 0 & 0 & 0 & 0 & 0 & 0 & 0 & \frac{K_A' T_C}{T_A T_B} & \frac{1}{T_B} & 0 \end{pmatrix}^T$$

(A-37)

Also, the entries '$\mathbf{0}$' in (A-38) are 5×5 zero matrices.

$$\boldsymbol{L_{33}} = \begin{pmatrix} L_a + L_{md} & L_{md} & L_{md} & 0 & 0 & 0 \\ L_{md} & L_{1d} + L_{kf} + L_{md} & L_{kf} + L_{md} & 0 & 0 & 0 \\ L_{md} & L_{kf} + L_{md} & L_{fd} + L_{kf} + L_{md} & 0 & 0 & 0 \\ 0 & 0 & 0 & L_a + L_{mq} & L_{mq} & L_{mq} \\ 0 & 0 & 0 & L_{mq} & L_{1q} + L_{qq} + L_{mq} & L_{qq} + L_{mq} \\ 0 & 0 & 0 & L_{mq} & L_{qq} + L_{mq} & L_{2q} + L_{qq} + L_{mq} \end{pmatrix}$$

(A-38)

$$\boldsymbol{L'_{33}} = \begin{pmatrix} \boldsymbol{L_{33}} & \mathbf{0} \\ \mathbf{0} & \mathbf{0} \end{pmatrix} \qquad \text{(A-39)}$$

Appendix II

A2 Small Signal Model of Conventional VSG with Embedded Current Controller

The small signal (SS) equations of the conventional voltage source interfaced VSG with the embedded current controller are developed based on [28] and are listed below for readers' convenience.

The structures of this VSG are in Figure A-1, and the equivalent external system is shown in Figure A-2. The corresponding state variables are all shown in these figures. Further descriptions can be found in [28].

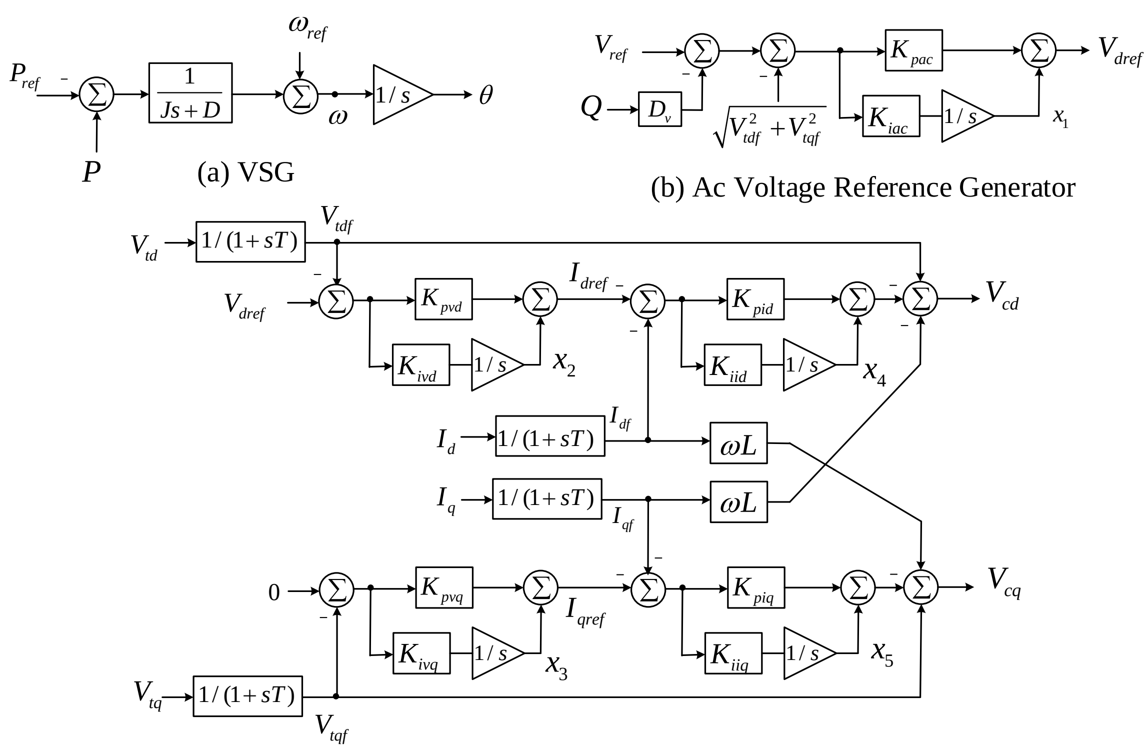

Figure A-1 Block Diagram of Control System. (a) VSG. (b) Ac Voltage Reference Generator. (c) Embedded Current Controller

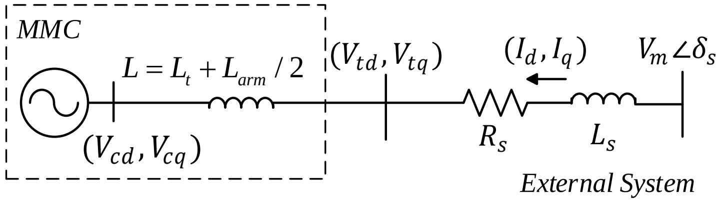

Figure A-2 Equivalent External System

Based on Figure A-1 and Figure A-2, the SS equations of the VSG with the embedded current controller are listed below. Note that ω_n is the nominal rotor speed, which is equal to 120π in the $60\,Hz$ system, and the superscript '0' denotes the steady-state value around which the equations are linearized.

$$T\frac{d\Delta V_{tdf}}{dt} = -\Delta V_{tdf} + \Delta V_{td} \tag{A-40}$$

$$T\frac{d\Delta V_{tqf}}{dt} = -\Delta V_{tqf} + \Delta V_{tq} \tag{A-41}$$

$$T\frac{d\Delta I_{df}}{dt} = -\Delta I_{df} + \Delta I_{d} \tag{A-42}$$

$$T\frac{d\Delta I_{qf}}{dt} = -\Delta I_{qf} + \Delta I_{q} \tag{A-43}$$

$$\frac{d\Delta x_1}{dt} = \Delta V_{ref} - \frac{V_{tdf}^0}{\left|V_{tf}^0\right|}\Delta V_{tdf} - \frac{V_{tqf}^0}{\left|V_{tf}^0\right|}\Delta V_{tqf} \tag{A-44}$$

$$\frac{d\Delta x_2}{dt} = \Delta V_{dref} - \Delta V_{tdf} \tag{A-45}$$

$$\frac{d\Delta x_3}{dt} = \Delta V_{tqf} \tag{A-46}$$

$$\frac{d\Delta x_4}{dt} = \Delta I_{dref} - \Delta I_{df} \tag{A-47}$$

$$\frac{d\Delta x_5}{dt} = \Delta I_{qref} - \Delta I_{qf} \tag{A-48}$$

$$J\frac{d\Delta\omega}{dt} = -D\Delta\omega + I_{df}^0\Delta V_{tdf} + V_{tdf}^0\Delta I_{df} + I_{qf}^0\Delta V_{tqf} + V_{tqf}^0\Delta I_{qf} - \Delta P_{ref} \tag{A-49}$$

$$\frac{d\Delta\theta}{dt} = \Delta\omega \tag{A-50}$$

$$\frac{L}{\omega_n}\frac{d\Delta I_d}{dt} = \Delta V_{td} - LI_q^0\Delta\omega - \omega^0 L\Delta I_q - \Delta V_{cd} \tag{A-51}$$

$$\frac{L}{\omega_n}\frac{d\Delta I_q}{dt} = \Delta V_{tq} + LI_d^0\Delta\omega + \omega^0 L\Delta I_d - \Delta V_{cq} \tag{A-52}$$

$$\frac{L_s}{\omega_n}\frac{d\Delta I_d}{dt} = \Delta V_{sd} - R_s\Delta I_d - L_sI_q^0\Delta\omega - \omega^0 L_s\Delta I_q - \Delta V_{td} \tag{A-53}$$

$$\frac{L_s}{\omega_n}\frac{d\Delta I_q}{dt} = \Delta V_{sq} - R_s\Delta I_q + L_sI_d^0\Delta\omega + \omega^0 L_s\Delta I_d - \Delta V_{tq} \tag{A-54}$$

$$0 = K_{iac}\Delta x_1 + K_{pac}\left(\Delta V_{ref} - \frac{V_{tdf}^0}{\left|V_{tf}^0\right|}\Delta V_{tdf} - \frac{V_{tqf}^0}{\left|V_{tf}^0\right|}\Delta V_{tqf}\right) - \Delta V_{dref} \tag{A-55}$$

$$0 = -K_{ivd}\Delta x_2 - K_{pvd}\left(\Delta V_{dref} - \Delta V_{tdf}\right) - \Delta I_{dref} \tag{A-56}$$

$$0 = -K_{ivq}\Delta x_3 + K_{pvq}\Delta V_{tqf} - \Delta I_{qref} \tag{A-57}$$

$$0 = \Delta V_{tdf} - LI_{qf}^0\Delta\omega - \omega^0 L\Delta I_{qf} - K_{iid}\Delta x_4 - K_{pid}\left(\Delta I_{dref} - \Delta I_{df}\right) - \Delta V_{cd} \tag{A-58}$$

$$0 = \Delta V_{tqf} + LI_{df}^0\Delta\omega + \omega^0 L\Delta I_{df} - K_{iiq}\Delta x_5 - K_{piq}\left(\Delta I_{qref} - \Delta I_{qf}\right) - \Delta V_{cq} \tag{A-59}$$

$$0 = V_m\sin(\delta^0 - \theta^0)\,\Delta\theta - \Delta V_{sd} \tag{A-60}$$

$$0 = V_m\cos(\delta^0 - \theta^0)\,\Delta\theta - \Delta V_{sq} \tag{A-61}$$

Then the Differential-Algebraic Equation (DAE) formulation of the above equations is given below,

$$\boldsymbol{E}\frac{d\boldsymbol{\Delta X}}{dt} = \boldsymbol{A\Delta X} + \boldsymbol{B\Delta u} \tag{A-62}$$

$$\boldsymbol{\Delta X} = \begin{matrix}[\Delta V_{tdf} \;\; \Delta V_{tqd} \;\; \Delta I_{df} \;\; \Delta I_{qf} \;\; \Delta x_1 \;\; \Delta x_2 \;\; \Delta x_3 \;\; \Delta x_4 \;\; \Delta x_5 \;\; \Delta\omega \;\; \Delta\theta \;\; \Delta I_d \;\; \Delta I_q \\ \Delta V_{td} \;\; \Delta V_{tq} \;\; \Delta V_{dref} \;\; \Delta I_{d_{ref}} \;\; \Delta I_{qref} \;\; \Delta V_{cd} \;\; \Delta V_{cq} \;\; \Delta V_{sd} \;\; \Delta V_{sq}]^T\end{matrix} \tag{A-63}$$

$$\boldsymbol{\Delta u} = \left[\Delta P_{ref} \quad \Delta V_{ref}\right]^T \tag{A-64}$$

Generally, $\boldsymbol{E}$ is singular and non-invertible because the (A-62) has algebraic variables. Therefore, the eigenvalues are calculated using matrix pencil $(\boldsymbol{A}, \boldsymbol{E})$. This will yield 13 finite eigenvalues which correspond to the modes of the linearized system and 9 infinite eigenvalues that comes with the network algebraic equations. These infinite eigenvalues do not impact the system dynamics; thus, they can be ignored. The remaining finite eigenvalues can be used for stability analysis.

References

[1] A. Yazdani and R. Iravani, *Voltage-sourced Converters in Power Systems: Modeling, Control, and Applications*. John Wiley & Sons, 2010.

[2] Chandorkar MC, Divan DM, Adapa R, "Control of parallel connected inverters in standalone AC supply systems". *IEEE. Trans Ind*, App 29(1):136–143, 1993.

[3] Soni N, Doolla S, Chandorkar MC, "Improvement of transient response in microgrids using virtual inertia". *IEEE Trans Power Deliv* 28(3):1830–1838, 2013.

[4] *VSC transmission*, CIGRE Working Group B4.37-269, Tech. Rep., 2005.

[5] E.W. Kimbark, *Direct Current Transmission, Vol. I.* New York: Wiley, 1971.

[6] J. Arrillaga, *High Voltage Direct Current Transmission, 2nd Edition*. London: The Institution of Electrical Engineers, 1998.

[7] C. Barker, *HVDC for beginners and beyond*, Alstom Grid, UK, 2002.

[8] Praça, A., Arakari, H., Alves, S.R., Eriksson, K., Graham, J., Biledt, G., Itaipu, "HVDC Transmission System - 10 years operational experience", *V SEPOPE*, Recife, May 1996.

[9] T. Smed and G. Andersson, 'Utilizing HVDC to damp power oscillations,' *IEEE Transactions on Power Delivery*, vol. 8, no. 2, pp. 620-627, April 1993.

[10] Sharifabadi, Kamran, et al. *Design, control, and application of modular multilevel converters for HVDC transmission systems*. John Wiley & Sons, 2016.

[11] N. Flourentzou, V. G. Agelidis, and G. D. Demetriades, "VSC-Based HVDC Power Transmission Systems: An Overview," *IEEE Transactions on Power Electronics*, vol. 24, no. 3, pp. 592-602, March 2009.

[12] A. Sinkar, A. Gole, V. Pathirana, and U. Gnanarathna, "Design Considerations for Parallel HVDC Links Feeding Offshore Platforms," in *Cigre Session*, August 2018, Paris, France.

[13] S. Debnath, J. Qin, B. Bahrani, M. Saeedifard and P. Barbosa, "Operation, Control, and Applications of the Modular Multilevel Converter: A Review," *IEEE Transactions on Power Electronics*, vol. 30, no. 1, pp. 37-53, Jan. 2015

[14] M. Glinka and R. Marquardt, "A new AC/AC multilevel converter family," *IEEE Transactions on Industrial Electronics*, vol. 52, no. 3, pp. 662-669, June 2005

[15] M. Hiller, D. Krug, R. Sommer, and S. Rohner, "A new highly modular medium voltage converter topology for industrial drive applications," in *13th European Conference on Power Electronics and Applications*, 2009, pp. 1-10.

[16] S. Debnath and M. Saeedifard, “A New Hybrid Modular Multilevel Converter for Grid Connection of Large Wind Turbines,” *IEEE Transactions on Sustainable Energy*, vol. 4, no. 4, pp. 1051-1064, Oct. 2013.

[17] P. Kundur, N. J. Balu, and M. G. Lauby, *Power System Stability and Control*, vol. 7. McGraw-hill New York, 1994.

[18] D. N. Zmood and D. G. Holmes, "Stationary frame current regulation of PWM inverters with zero steady-state error," *IEEE Transactions on Power Electronics*, vol. 18, no. 3, pp. 814-822, May 2003.

[19] R. Rosso, X. Wang, M. Liserre, X. Lu and S. Engelken, "Grid-Forming Converters: Control Approaches, Grid-Synchronization, and Future Trends—A Review," *IEEE Open Journal of Industry Applications*, vol. 2, pp. 93-109, 2021.

[20] Liu J, Miura Y, Ise T, “Comparison of dynamic characteristics between virtual synchronous generator and droop control in inverter-based distributed generators”. *IEEE Trans Power Electron* 31(5):3600–3611, 2016.

[21] Coelho EAA, Cortizo PC, Garcia P.F.D, “Small-signal stability for parallel-connected inverters in stand-alone AC supply systems”. *IEEE Trans Ind*, Appl 38(2):533–542, 2002.

[22] Q.-C. Zhong and G. Weiss, “Synchronverters: Inverters that mimic synchronous generators,” *IEEE Trans. Ind. Electron*, vol. 58, no. 4, pp. 1259–1267, Apr. 2011.

[23] C. Jiang, A. D. Sinkar, M. K. Das, A. M. Gole, and V. Pathirana, "A comparative study of master-slave control and virtual synchronous machine control for parallel VSC-HVDC links feeding passive loads on offshore platforms," in *15th IET International Conference on AC and DC Power Transmission (ACDC 2019)*, Coventry, UK, 2019, pp. 1-6.

[24] Dong, S., Chi, Y., Li, Y.: ‘Active voltage feedback control for hybrid multiterminal HVDC system adopting improved synchronverters’, *IEEE Trans. Power Deliv*., 2016, 31, (2), pp. 445–455.

[25] J. Roldán-Pérez, A. Rodríguez-Cabero and M. Prodanovic, "Design and Analysis of Virtual Synchronous Machines in Inductive and Resistive Weak Grids," *IEEE Transactions on Energy Conversion*, vol. 34, no. 4, pp. 1818-1828, Dec. 2019.

[26] Salvatore D’Arco, Jon Are Suul, Olav B. Fosso, “A Virtual Synchronous Machine implementation for distributed control of power converters in Smart Grids”, *Electric Power Systems Research*, Volume 122, 2015, Pages 180-197.

[27] P. Rodríguez, C. Citro, J. I. Candela, J. Rocabert and A. Luna, "Flexible Grid Connection and Islanding of SPC-Based PV Power Converters," *IEEE Transactions on Industry Applications*, vol. 54, no. 3, pp. 2690-2702, May-June 2018.

[28] A. F. Darbandi, A. Sinkar, and A. Gole, "Effect of Short-Circuit Ratio and Current Limiting on the Stability of a Virtual Synchronous Machine Type Gridforming Converter," in *17th International Conference on AC and DC Power Transmission (ACDC 2021)*, Glasgow, UK, 2021, pp. 182-187.

[29] T. Magg, M. Manchen, E. Krige, J. Wasborg and J. Sundin, "Connecting networks with VSC HVDC in Africa: Caprivi Link interconnector," IEEE Power and Energy Society Conference and Exposition in Africa: Intelligent Grid Integration of Renewable Energy Resources (PowerAfrica), Johannesburg, South Africa, 2012

[30] M. A. Torres L., L. A. C. Lopes, L. A. Moran T., and J. R. Espinoza C., "Self-tuning virtual synchronous machine: A control strategy for energy storage systems to support dynamic frequency control," *IEEE Trans. Energy Convers.*, vol. 29, no. 4, pp. 833–840, Dec. 2014.

[31] A. Lesnicar and R. Marquardt, "An innovative modular multilevel converter topology suitable for a wide power range," in *2003 IEEE Bologna Power Tech Conference Proceedings*, pp. 6 pp. Vol.3, 2003.

[32] Y. Wang, D. Sun, X. Wang and L. Zhang, "A Novel Low Voltage Ride Through Control Strategy Based on Virtual Synchronous Generator," in *2019 IEEE 28th International Symposium on Industrial Electronics (ISIE)*, Vancouver, BC, Canada, 2019, pp. 2105-2110.

[33] A. Gkountaras, S. Dieckerhoff, and T. Sezi, "Evaluation of current limiting methods for grid forming inverters in medium voltage microgrids," in *2015 IEEE Energy Conversion Congress and Exposition (ECCE)*, Montreal, QC, 2015, pp. 1223-1230.

[34] T. Chen, L. Chen, T. Zheng, X. Chen, and S. Mei, "General control strategy to limit peak currents of Virtual Synchronous Generator under voltage sags," in *2016 IEEE Power and Energy Society General Meeting (PESGM)*, Boston, MA, 2016, pp. 1-5.

[35] R. H. Lasseter, Z. Chen, and D. Pattabiraman, "Grid-Forming Inverters: A Critical Asset for the Power Grid," *IEEE Journal of Emerging and Selected Topics in Power Electronics*, vol. 8, no. 2, pp. 925-935, June 2020.

[36] M. Li, W. Huang, N. Tai, M. Yu, Y. Lu, and C. Ni, "Transient Behavior Analysis of VSG-IIDG During Disturbances Considering the Current Limit Unit," in *2019 IEEE Power & Energy Society General Meeting (PESGM)*, Atlanta, GA, USA, 2019, pp. 1-5.

[37] A. G. Paspatis and G. C. Konstantopoulos, "Current-limiting droop control with virtual inertia and self-synchronization properties," in *IECON 2017 - 43rd Annual Conference of the IEEE Industrial Electronics Society*, Beijing, 2017, pp. 196-201.

[38] M. R. Sreejith and M. C. Chandorkar, "Electrical source emulation using modular multilevel converter," in *2014 IEEE International Conference on Power Electronics, Drives and Energy Systems (PEDES*), Mumbai, 2014, pp. 1-6.

[39] L. Zhou et al., "Harmonic Current and Inrush Fault Current Coordinated Suppression Method for VSG under Non-ideal Grid Condition," *IEEE Transactions on Power Electronics*, vol. 36, no. 1, pp. 1030-1042, Jan. 2021.

[40] S. Dong, Y. Chi, and Y. Li, "Active Voltage Feedback Control for Hybrid Multiterminal HVDC System Adopting Improved Synchronverters," *IEEE Transactions on Power Delivery*, vol. 31, no. 2, pp. 445-455, April 2016.

[41] R. Chokhawala, "Powering platforms," *ABB Rev*., pp. 52–56, 2008.

[42] B. Westman, S. Gilje, and M. Hyttinen, "Valhall re-development project, power from shore," in *PCIC Europe 2010 Conference Record*, 2010, pp. 1–5.

[43] L. Stendius and P. Jones, "The challenges of offshore power system construction-bringing power successfully to Troll A, one of the worlds largest oil and gas platform," in *The 8th IEE International Conference on AC and DC Power Transmission*, London, UK, 2006, pp. 75-78.

[44] K. Sharifabadi, N. Krajisnik, R. Teixeira Pinto, S. Achenbach, and R. Rad, "Parallel operation of multivendor VSC-HVDC schemes feeding a large islanded offshore Oil and Gas grid," in *Cigre Session*, August 2018, Paris, France.

[45] A. Mohd, E. Ortjohann, D. Morton, and O. Omari, "Review of control techniques for inverters parallel operation," *Electr. Power Syst. Res.*, vol. 80, no. 12, pp. 1477–1487, 2010.

[46] Frede Blaabjerg, *Control of Power Electronic Converters and Systems*, Academic Press, 2018, vol. 7, pp. 371-380

[47] CIGRE WG B4.19, "Static synchronous compensator (STATCOM) for arc furnace and flicker compensation", in *CIGRE Technical Brochure 237*, September 2003

[48] *Power Electronics Handbook*, Fourth Edition, Butterworth-Heinemann, 2018

[49] A. D. Rajapakse, A. M. Gole, and P. L. Wilson, "Electromagnetic transients simulation models for accurate representation of switching losses and thermal performance in power electronic systems," *IEEE Transactions on Power Delivery*, vol. 20, no. 1, pp. 319-327, Jan. 2005.

[50] A. D. Rajapakse, A. M. Gole, and R. P. Jayasinghe, “An Improved Representation of FACTS Controller Semiconductor Losses in EMTP-Type Programs Using Accurate Loss-Power Injection Into Network Solution,” *IEEE Transactions on Power Delivery*, vol. 24, no. 1, pp. 381-389, Jan. 2009.

[51] M. P. Kazmierkowski and L. Malesani, “Current control techniques for three-phase voltage-source PWM converters: a survey,” *IEEE Transactions on Industrial Electronics*, vol. 45, no. 5, pp. 691-703, Oct. 1998.

[52] F. Martinez-Rodrigo, D. Ramirez, H. Mendonça, S. de Pablo, “MMC as nonlinear vector current source for grid connection of wave energy generation”, *International Journal of Electrical Power & Energy Systems*, Volume 113, 2019, Pages 686-698

[53] A. Shukla, A. Ghosh, and A. Joshi, “Hysteresis Modulation of Multilevel Inverters,” in *IEEE Transactions on Power Electronics*, vol. 26, no. 5, pp. 1396-1409, May. 2011

[54] L. Yunbo, X. Yonghai and X. Yunfei, "A MMC hysteresis current control method based on current slope," in the *IECON 2017-43rd Annual Conference of the IEEE Industrial Electronics Society*, Beijing, China, 2017, pp. 577-582

[55] M Guan, Z Xu, “Modeling and Control of Modular Multilevel Converter in HVDC Transmission,” *Automation of Electric Power System*, vol. 34, no. 19, pp. 64-68, Oct. 2010.

[56] Toshiba Silicon N-Channel IEGT, ST1500GXH24 Product Specification Sheet, March. 2003.

[57] P. Sanjeevikumar, C. Sharmeela, Jens Bo Holm-Nielsen, P. Sivaraman, *Power Quality in Modern Power Systems*, Academic Press, 2021.

[58] M. Peterson, B. N. Singh, and P. Rastgoufard, “Active and Passive Filtering for Harmonic Compensation,” in *40th Southeastern Symposium on System Theory (SSST)*, 2008, pp. 188-192.

[59] B. Singh, K. Al-Haddad and A. Chandra, “A review of active filters for power quality improvement,” *IEEE Transactions on Industrial Electronics*, vol. 46, no. 5, pp. 960-971, Oct. 1999.

[60] Hang Li, “Controller Implementation and Performance Evaluation of A High Power Three-phase Active Power Filter using Controller Hardware-in-the-loop Simulation,” M.S. thesis, Department of Electrical and Computer Engineering., University of Manitoba., Winnipeg, Manitoba, Canada, 2018.

[61] H. S. Stone, "R66-50 An Algorithm for the Machine Calculation of Complex Fourier Series," *IEEE Transactions on Electronic Computers*, vol. EC-15, no. 4, pp. 680-681, Aug. 1966

[62] *Real-Time Digital Simulator (RTDS) User's Manual Set*, RTDS Technologies, Winnipeg, MB, Canada, 2008.

[63] Sir Isaac Newton, *The Method of Fluxions and Infinite Series: With Its Application to the Geometry of Curve-lines*. Translated from the Author's Latin Original Not Yet Made Publick. To which is Subjoin'd, a Perpetual Comment Upon the Whole Work, By John Colson, Sir Isaac Newton. Henry Woodfall; and sold by John Nourse, 1736.

[64] Gole, Aniruddha M. "Exciter stresses in capacitively loaded synchronous generators", Ph.D. dissertation, Department of Electrical and Computer Engineering, University of Manitoba, Winnipeg, Canada, 1982.

[65] A. M. Gole, R. W. Menzies, H. M. Turanli and D. A. Woodford, "Improved Interfacing of Electrical Machine Models to Electromagnetic Transients Programs," *IEEE Transactions on Power Apparatus and Systems*, vol. PAS-103, no. 9, pp. 2446-2451, Sept. 1984

[66] Butcher, John C, *Numerical Methods for Ordinary Differential Equations*, New York: John Wiley & Sons, 2003.

[67] Atkinson, Kendall E., *An Introduction to Numerical Analysis* (2nd ed.), New York: John Wiley & Sons, 1989.

[68] *IEEE Recommended Practice for Excitation System Models for Power System Stability Studies*, IEEE Std 421.5-1992, vol., no., pp.1-56, 10 Aug. 1992

[69] Aleksey Suvorov, Alisher Askarov, Yuly Bay, Boris Maliuta, Andrey Achitaev, Konstantin Suslov, "Comparative small-signal stability analysis of voltage-controlled and enhanced current-controlled virtual synchronous generators under weak and stiff grid conditions", *International Journal of Electrical Power & Energy Systems*, Volume 147, 2023.

[70] Bonyadi MR, Michalewicz Z. "Particle Swarm Optimization for Single Objective Continuous Space Problems: A Review". *Evol Comput*. 2017 Spring;25(1):1-54.

[71] Acosta Sarmiento, Jhair Stivel. "Optimization of Overhead Transmission Lines With Multiple Circuits At Different Voltage Levels On the Same Tower." Ph.D. dissertation, Department of Electrical and Computing Engineering, University of Campinas, Brazil, 2021.

[72] Firas Gerges, Germain Zouein, and Danielle Azar. "Genetic Algorithms with Local Optima Handling to Solve Sudoku Puzzles". In *2018 International Conference on Computing and Artificial Intelligence (ICCAI 2018)*. Association for Computing Machinery, New York, NY, USA, 19–22.

[73] Lothar M. Schmitt, "Theory of Genetic Algorithms II: models for genetic operators over the string-tensor representation of populations and convergence to global optima for arbitrary

fitness function under scaling”, *Theoretical Computer Science*, Volume 310, Issues 1–3, 2004, Pages 181-231

[74] Jhair S. Acosta, Maria C. Tavares, Aniruddha M. Gole, “Optimizing multi-circuit transmission lines for single-phase auto-reclosing”, *Electric Power Systems Research*, Volume 197, 2021.

[75] A. M. Gole, S. Filizadeh and P. L. Wilson, "Inclusion of robustness into design using optimization-enabled transient simulation," *IEEE Transactions on Power Delivery*, vol. 20, no. 3, pp. 1991-1997, July 2005.

[76] C. Jiang, A. D. Sinkar and A. M. Gole, "Comparative study of Swing Equation-based and full emulation-based Virtual Synchronous Generators," in *11th International Conference on Power Electronics, Machines, and Drives (PEMD 2022)*, 2022, pp. 578-582.

[77] K. Hatipoglu, M. Olama, and Y. Xue, "Model-Free Dynamic Voltage Control of a Synchronous Generator-Based Microgrid," in *2020 IEEE Power & Energy Society Innovative Smart Grid Technologies Conference (ISGT)*, 2020, pp. 1-5

[78] Gao F, Iravani MRA, “Control strategy for a distributed generation unit in grid-connected and autonomous modes of operation”. *IEEE Trans Power Deliv* 23(2):850–859, 2008

[79] D’Arco S, Suul JA, “Equivalence of virtual synchronous machines and frequency-droops for converter-based microgrids”. *IEEE Trans Smart Grid* 5(1):394–395, 2014

[80] Pogaku N, Prodanovic´ M, Green TC, “Modeling, analysis and testing of autonomous operation of an inverter-based microgrid”. *IEEE Trans Power Electron* 22(2):613–625, 2007

[81] Guan M, Pan W, Zhang J, et al, “Synchronous generator emulation control strategy for voltage source converter (VSC) stations”. *IEEE Trans Power Syst* 30(6):3093–3101, 2015

[82] Beck HP, Hesse R, “Virtual synchronous machine”, in *Proceedings of the elect power quality and utilisation conference*, Barcelona, Spain, 10–13 October 2007.

[83] Driesen J, Visscher K, “Virtual synchronous generators”. In Proceedings of *the power and energy society general meeting*, Pittsburgh, USA, 20–24 July 2008

[84] Y. Chen, R. Hesse, D. Turschner, and H.-P. Beck, “Improving the grid power quality using virtual synchronous machines,” in *Conf. Power Eng. Energy. Elect. Drives*, 2011, pp. 1–6.

[85] M. P. N. Van Wesenbeeck, S. W. H. De Haan, P. Varela, and K. Visscher, “Grid tied converter with virtual kinetic storage,” in. *IEEE Powertech Conf.*, 2009, pp. 1–7.

[86] M. Torres and L. A. C. Lopes, “Virtual synchronous generator control in autonomous wind-diesel power systems,” in *Proc. IEEE Elect. Power Energy Conf.*, 2009, pp. 1–6.

[87] V. Karapanos, S. De Haan, and K. Zwetsloot, “Real time simulation of a power system with VSG hardware in the loop,” in *Proc. 37th Annu. Conf. IEEE Ind. Electron. Soc*., 2011, pp. 3748–3754.

[88] Y. Hirase, O. Noro, E. Yoshimura, H. Nakagawa, K. Sakimoto, and Y. Shindo, “Virtual synchronous generator control with double decoupled synchronous reference frame for single-phase inverter,” in *Proc. Int. Power Electron. Conf*., 2014, pp. 1552–1559.

[89] X.-Z. Yang, J.-H. Su, M. Ding, J.-W. Li, and D. Yan, “Control strategy for virtual synchronous generator in microgrid,” in Proc. *4th Int. Conf. Elect. Utility Dereg. Restruct. Power Technol*., 2011, pp. 1633–1637.

[90] Sakimoto K, Miura Y, Ise T, “Stabilization of a power system with a distributed generator by a virtual synchronous generator function”. In Proc *International conference on power electronics and ECCE*, Asia, Jeju, the Republic of Korea, 1–4 January 2011, 8 pp

[91] T. Shintai, Y. Miura, and T. Ise, “Reactive power control for load sharing with virtual synchronous generator control,” in Proc. *7th Int. Power Electron. Motion Control Conf*., 2012, pp. 846–853.

[92] T. Shintai, Y. Miura, and T. Ise, “Oscillation damping of a distributed generator using a virtual synchronous generator,” *IEEE Trans. Power Del*., vol. 29, no. 2, pp. 668–676, Apr. 2014.

[93] J. Alipoor, Y. Miura, and T. Ise, “Power system stabilization using virtual synchronous generator with alternating moment of inertia,” *IEEE J. Emerg. Sel. Topics Power Electron*., vol. 3, no. 2, pp. 451–458, Jun. 2015.

[94] S. Yazdani, M. Ferdowsi, M. Davari, and P. Shamsi, "Advanced Current-Limiting and Power-Sharing Control in a PV-Based Grid-Forming Inverter Under Unbalanced Grid Conditions," *IEEE Journal of Emerging and Selected Topics in Power Electronics*, vol. 8, no. 2, pp. 1084-1096, June 2020.

[95] K. Shi, W. Song, P. Xu, R. Liu, Z. Fang, and Y. Ji, "Low-Voltage Ride-Through Control Strategy for a Virtual Synchronous Generator Based on Smooth Switching," *IEEE Access*, vol. 6, pp. 2703-2711, 2018.

[96] A. D. Paquette and D. M. Divan, "Virtual Impedance Current Limiting for Inverters in Microgrids with Synchronous Generators," *IEEE Transactions on Industry Applications*, vol. 51, no. 2, pp. 1630-1638, March-April 2015.

[97] K. Sakimoto, Y. Miura and T. Ise, "Stabilization of a power system with a distributed generator by a Virtual Synchronous Generator function," in *8th International Conference on Power Electronics – ECCE,* Asia, Jeju, 2011, pp. 1498-1505

[98] J. Ruan, R. Cai, X. Huang, and H. Xie, "Comparison of Virtual and Conventional Synchronous Generators Based on a Modularized Analysis Tool," in *2018 China International Conference on Electricity Distribution (CICED)*, Tianjin, 2018, pp. 2242-2246

[99] Hartmann, B, Vokony, I, Táczi, I. "Effects of decreasing synchronous inertia on power system dynamics—Overview of recent experiences and marketisation of services." *Int Trans Electr Energ Syst*. 2019

[100] El Chehaly, Mohamed, "Power system stability analysis with a high penetration of distributed generation." M.S. thesis, Department of Electrical and Computer Engineering, McGill University, Montréal, Canada, 2010.

[101] T. Magg, M. Manchen, E. Krige, J. Wasborg, and J. Sundin, "Connecting networks with VSC HVDC in Africa: Caprivi Link interconnector," in *IEEE Power and Energy Society Conference and Exposition in Africa: Intelligent Grid Integration of Renewable Energy Resources (PowerAfrica)*, 2012, pp. 1-6

[102] T. Esram and P. L. Chapman, "Comparison of Photovoltaic Array Maximum Power Point Tracking Techniques," *IEEE Transactions on Energy Conversion*, vol. 22, no. 2, pp. 439-449, Jun

[103] J. H. Vivas, G. Bergna and M. Boyra, "Comparison of multilevel converter-based STATCOMs," in *14th European Conference on Power Electronics and Applications*, 2011, pp. 1-10